Strojniški vestnik

Journal of Mechanical Engineering

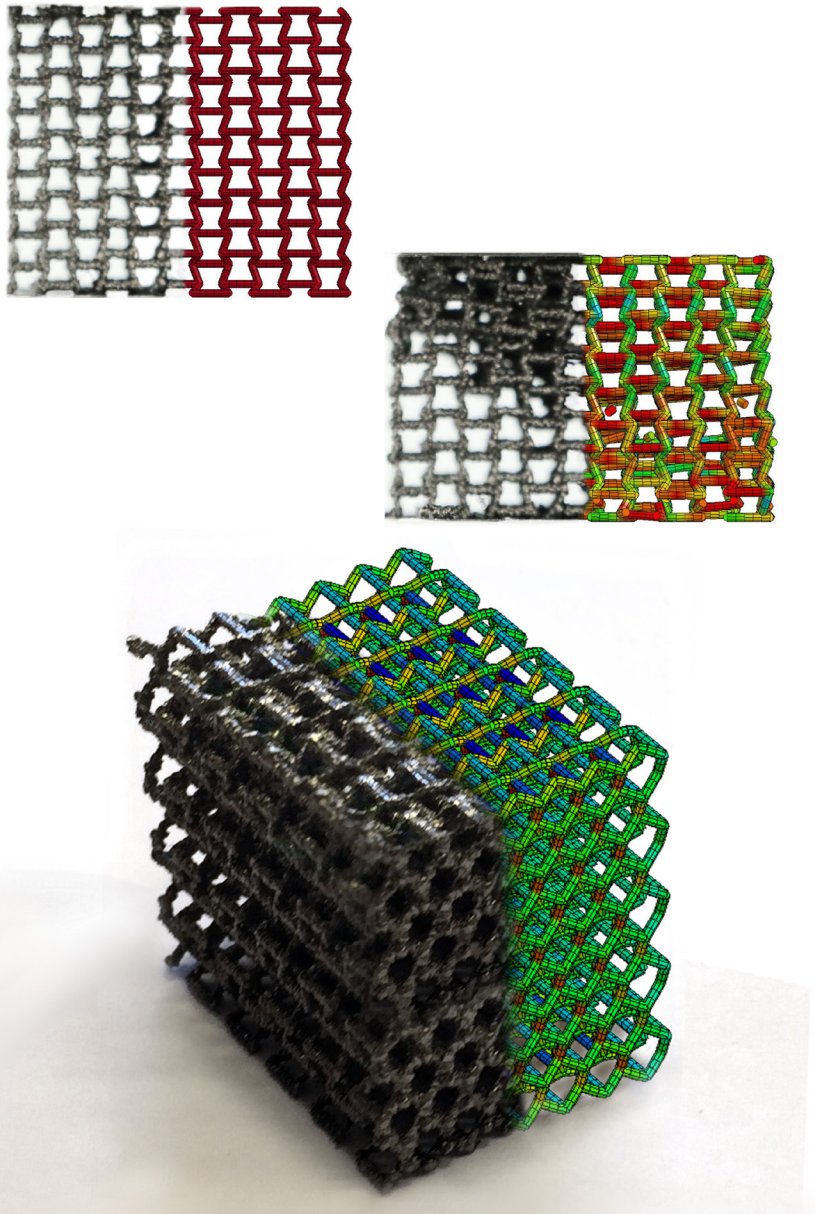

no. 9
year 2016
volume 62

Strojniški vestnik – Journal of Mechanical Engineering (SV-JME)

Aim and Scope
The international journal publishes original and (mini)review articles covering the concepts of materials science, mechanics, kinematics, thermodynamics, energy and environment, mechatronics and robotics, fluid mechanics, tribology, cybernetics, industrial engineering and structural analysis.
The journal follows new trends and progress proven practice in the mechanical engineering and also in the closely related sciences as are electrical, civil and process engineering, medicine, microbiology, ecology, agriculture, transport systems, aviation, and others, thus creating a unique forum for interdisciplinary or multidisciplinary dialogue.
The international conferences selected papers are welcome for publishing as a special issue of SV-JME with invited co-editor(s).

Editorial Office
University of Ljubljana, Faculty of Mechanical Engineering
SV-JME, Aškerčeva 6, SI-1000 Ljubljana, Slovenia
Phone: 386 (0)1 4771 137
Fax: 386 (0)1 2518 567
info@sv-jme.eu, http://www.sv-jme.eu

Print: Grafex, d.o.o., printed in 310 copies

Founders and Publishers
University of Ljubljana, Faculty of Mechanical Engineering, Slovenia
University of Maribor, Faculty of Mechanical Engineering, Slovenia
Association of Mechanical Engineers of Slovenia
Chamber of Commerce and Industry of Slovenia, Metal Processing Industry Association

Cover: The cover shows an auxetic cellular structure fabricated at the Institute of Materials Science and Technology (WTM), University of Erlangen-Nürnberg, Germany, and mechanically characterised at the University of Maribor. The bottom figure shows the geometry of undeformed auxetic cellular structure (fabricated sample and numerical model), while the top two figures illustrate the compressive behaviour at two different deformation levels determined both experimentally and computationally.

Image Courtesy: Nejc Novak, Laboratory for Advanced Computational Engineering and Experimenting, Faculty of Mechanical Engineering, University of Maribor, Slovenia

ISSN 0039-2480

General information
Strojniški vestnik – Journal of Mechanical Engineering is published in 11 issues per year (July and August is a double issue).

Institutional prices include print & online access: institutional subscription price and foreign subscription €100,00 (the price of a single issue is €10,00); general public subscription and student subscription €50,00 (the price of a single issue is €5,00). Prices are exclusive of tax. Delivery is included in the price. The recipient is responsible for paying any import duties or taxes. Legal title passes to the customer on dispatch by our distributor.

Single issues from current and recent volumes are available at the current single-issue price. To order the journal, please complete the form on our website. For submissions, subscriptions and all other information please visit: *http://en.sv-jme.eu/.*

You can advertise on the inner and outer side of the back cover of the journal. The authors of the published papers are invited to send photos or pictures with short explanation for cover content.

We would like to thank the reviewers who have taken part in the peer-review process.

The journal is subsidized by Slovenian Research Agency.

Strojniški vestnik - Journal of Mechanical Engineering is available on http://www.sv-jme.eu, where you access also to papers' supplements, such as simulations, etc.

Contents

Strojniški vestnik - Journal of Mechanical Engineering
volume 62, (2016), number 9
Ljubljana, September 2016
ISSN 0039-2480

Published monthly

Papers

Strojniški vestnik - Journal of Mechanical Engineering 62(2016)9, 485-493

DOI:10.5545/sv-jme.2016.3656 Review Scientific Paper
Received for review: 2016-04-11
Received revised form: 2016-05-30
Accepted for publication: 2016-06-01

Auxetic Cellular Materials - a Review

Nejc Novak* – Matej Vesenjak – Zoran Ren
University of Maribor, Faculty of Mechanical Engineering, Slovenia

Auxetic cellular materials are modern materials which have some unique and superior mechanical properties. As a consequence of the structural deformation of their internal cellular structure they exhibit a negative Poisson's ratio, i.e. they significantly increase in volume when stretched and vice versa. The effect of negative Poisson's ratio is useful in many applications to enhance certain physical properties such as the density, stiffness, fracture toughness, energy absorption and damping. These properties can be further tailored by using variable cell geometry and density distribution, which can be achieved with functionally graded porosity of auxetic materials. This review paper provides the state-of-the-art overview of the auxetic materials, their development, most common geometries, fabrication methods, mechanical properties, applications and further possibilities for their development.

Keywords: cellular materials, auxetic materials, negative Poisson's ratio, honeycombs, composites

Highlights

- *Development, geometries, fabrication methods of auxetic cellular materials are presented.*
- *Identification and comparison of mechanical properties of different types of auxetic materials.*
- *Applications of auxetic materials are introduced.*
- *Possibilities for further development of graded auxetic cellular materials are indicated.*

0 INTRODUCTION

Cellular materials have some advantageous mechanical and thermal properties in comparison to solid materials [1], for example: low density, high acoustic isolation and damping, better thermal management (for use in heat exchangers, flame arresters, heat shields), high energy absorption capabilities (for crash absorbers), durability at dynamic loadings and fatigue, filters etc. The production methods of cellular materials are described in [2] and [3]. Some cellular materials are being used in practical applications [4], but most of them were only investigated by experiments and simulations [5] to [8]. This is due to high production costs and a lack of mass production capabilities to control the shape, size and distribution of cellular pores during the production process which results in a certain scatter of mechanical properties. Novel uni-directional structures, such as lotus-type [7] and UniPore [8] materials, hollow sphere structures [9] and [10] and APM elements [11] to [13] were introduced recently, and comprehensively characterised. The new additive manufacturing technologies offer improvements in the production of cellular structures with constant or graded porosity.

The internal structure of cellular materials can also be designed so that its deformation results in a negative Poisson's ratio behaviour. Poisson's ratio (ν) is defined (in case of tension loading) as the ratio between the longitudinal expansion and the lateral contraction of material during the loading [14]. Materials that exhibit negative Poisson's ratio become wider when stretched and thinner when compressed (Fig. 1), and are also called the auxetic materials [15].

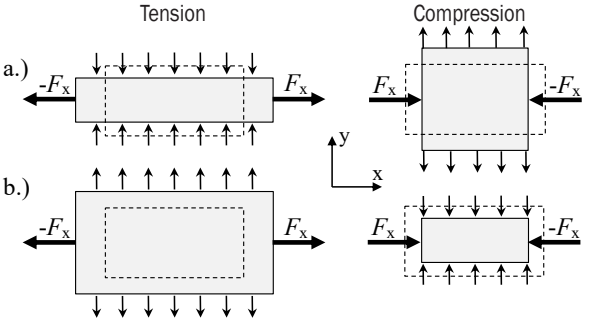

Fig. 1. *Non-auxetic a) and auxetic b) behaviour during tensile and compressive loading (dashed lines – undeformed geometry)*

This paper provides a short review of the development, geometries, manufacturing methods, mechanical properties and applications of cellular auxetic materials. Future prospects for further development and new applications of cellular auxetic materials are also discussed.

1 AUXETIC MATERIALS

The term "auxetic materials" was first introduced by Evans et al. in 1991 (from the Greek auxetos: that may be increased) [15]. The natural auxetic material can be found in α-cristobalite [16], biological tissues (skin)

*Corr. Author's Address: University of Maribor, Faculty of Mechanical Engineering, Smetanova 17, Maribor, Slovenia, nejc.novak5@um.si

[17] and pyrolytic graphite [18]. Man-made material structures with similar behaviour were first used in practical application as moderator core of a Magnox nuclear reactor [19], where auxetic behaviour occurs due to radial movement of the free-standing columns of graphite bricks via sliding of the loose keys. The structure was designed to withstand horizontal forces generated during earthquake, whilst also allowing free movement of the structure to accommodate thermal movements between the graphite core and steel supporting structures at the edges of the core. Development of this structure was conducted to solve a practical problem and auxetic behaviour was only a by-product of the design.

Systematic research of auxetic materials first started in 1985 with analysis of a 2D re-entrant auxetic structure by Almgren [20] based on analytical expressions presented a few years earlier for conventional honeycombs [21]. In 1987 first auxetic material was manufactured by Lakes and co-workers with transformation of conventional open cell foam [22]. Auxetic structures from polymers were also fabricated later [23] to [25]. Further progress was made by introducing composite structures that exhibit negative Poisson's ratio [26]. Next promising way to produce cheaper, more complex and larger auxetic structures is additive manufacturing.

It is not always necessary to have a porous microstructure (like in cellular materials) to induce the auxetic behaviour of the material structure [26]. The change in microstructure (molecular auxetic materials) or composite structures with rotating units can also exhibit the auxetic behaviour [27].

However, most of above mentioned auxetic structures are highly anisotropic and thus not well suited for the general structural applications in most cases. For this reason, a very exciting development of novel 3D cellular auxetic materials is being investigated at several research centres around the world and we can expect some promising auxetic materials to emerge soon.

Most of auxetic materials can be classified into three main groups: auxetic honeycombs, auxetic microporous polymers and auxetic composites. Auxetic materials which do not belong to any of these groups are also described in Section 1.4.

1.1 Auxetic Honeycombs

Conventional and auxetic honeycomb 2D structures are the most common types which have been investigated widely over past few decades. These 2D structures can be extended in the normal direction to get a 3D unidirectional auxetic structure.

1.1.1 Re-entrant Structures

Development of 2D re-entrant honeycombs (Fig. 2) started with analytical calculations of various deformation mechanisms caused by flexing the cell walls [20] or more realistic behaviour when honeycombs undergo flexure, stretching and hinging deflections when subjected to external loadings [28].

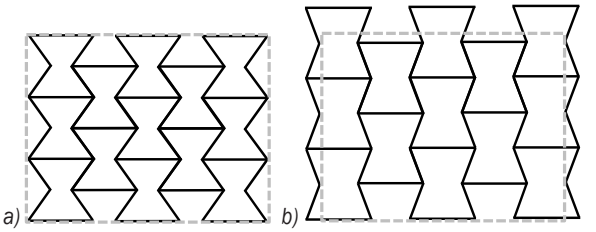

Fig. 2. *a) Undeformed and b) deformed re-entrant structure*

1.1.2 Rotating Units

Auxetic structures with rotating units were presented by Grima and Evans [27], where rigid rectangular and triangular cells are connected together at selected vertices by hinges (Fig. 3). These kinds of structures result in analytical value of minus one for the Poisson's ratio. The auxetic behaviour of the rotating units was analysed with analytical expressions for the rotating rectangles [29] and [30] and the triangles [27]. Semi-rigid rotating units were also developed [31]. Real structures with similar behaviour as the rotating units (square array with elliptical voids) were analysed with experimental testing and numerical simulations [32].

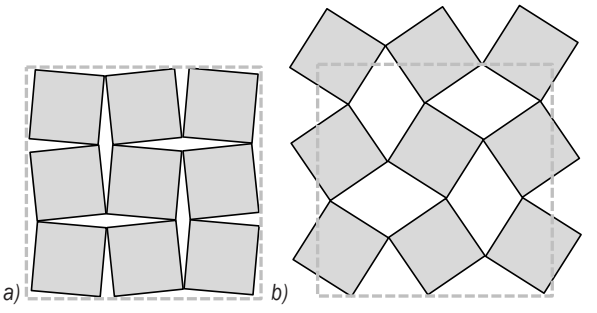

Fig. 3. *a) Undeformed and b) deformed rotating rectangles*

1.1.3 Missing Rib

Missing rib structure is derived from conventional honeycomb (intact) where cutting of some ribs (Fig.

4) leads to the auxetic behaviour [33]. Experimental testing of two different missing rib structures and two conventional structures was done by Gaspar et. al [34].

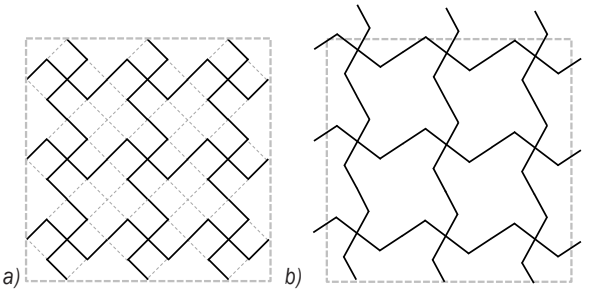

Fig. 4. *a) Undeformed and b) deformed missing rib structure (dashed lines-intact conventional structure)*

1.1.4 Chiral Structures

Chiral structures are formed by connecting straight ligaments (ribs) to central nodes which may be circles or other geometrical forms (Fig. 5). The auxetic effects are achieved through wrapping or unwrapping of the ligaments around the nodes in response to the applied force. Poisson's ratio of chiral structures is –1, based on theoretical and experimental investigation [35].

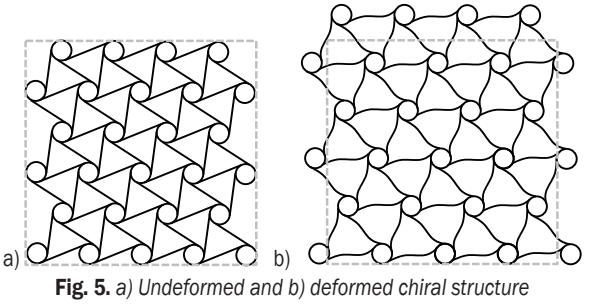

Fig. 5. *a) Undeformed and b) deformed chiral structure*

1.1.5 Other Honeycomb Geometries

Many other auxetic geometries were also developed in the past: antichiral structures with different strategies of connecting central nodes [36], star [37] and double arrowhead [38] structures, 2D planar structures using Kagome patterns [39] and [40]. Geometry of auxetic honeycombs was also developed with numerical analysis of eigenvalues and natural frequencies of different non-auxetic honeycombs [41].

1.2 Auxetic Microporous and Molecular Polymers

After successful production of auxetic material from conventional polymer foam [22] researchers were looking for procedure with which they can fabricate stiffer materials for wider engineering applications. Structure from expanded polytetrafluoroethylene (PTFE) was produced and evaluated by tensile testing methods [23] and [24]. Extremely low negative Poisson's ratio values up to minus 12 in one direction were achieved and explained by the anisotropic foam structure. A simple concept to explain the complex microstructure deformation behaviour found in auxetic PTFE is shown in Fig. 6, where hatched regions are nodules. Further experimental testing and deformation mechanism analysis was done by Alderson and Evans [42] and Alderson et al. [43].

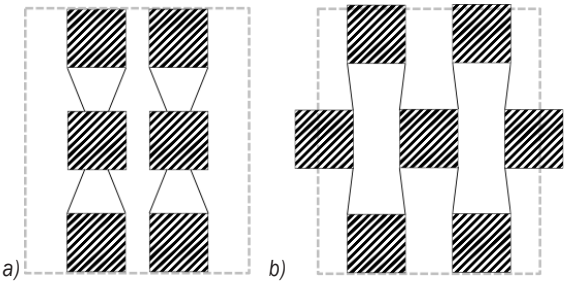

Fig. 6. *a) Undeformed and b) deformed nodule-fibril model network*

Similar microporous polymer microstructures can be produced using the ultra high molecular weight polyethylene (UHMWPE), with some distinct differences: nodules in UHMWPE are nearly spherical and the structure is more isotropic. These differences also influence the Poisson's ratio which for UHMWPE is no lower than minus 1.24 [25].

Researchers have also observed that the auxetic behavior of some of the polymer structures is not depend on the scale of the material [44], which is convenient for production of larger specimens and components.

Microporous auxetic polymers possess auxetic properties because their porous structures allows sufficient space for the nodules to spread apart. But this porosity leads to lower density and stiffness values resulting in their unsuitability in many structural applications.

One approach to overcome the problem with material porosity is to develop molecular auxetic material, where the molecular structure is tailored to exhibit negative Poisson's ratio [45] and [46]. Tailoring is done by inserting molecular elements which causes the auxetic behaviour in the molecular structure. However, many problems in synthesizing and testing these materials still need to be overcome [15]. In the future, when synthesizing methods improve and allow for the development of anisotropic molecular auxetic

materials, these kinds of materials could well turn out to be the best auxetic materials for use in structural applications.

1.3 Auxetic Composites

Composite materials are made of two or more different components with different material properties. Composite rod and hinge structures were first analytically investigated by Milton [26]. The model is shown in Fig. 7, where under infinitesimal deformations in the increase in the width AB causes an increase in the length CD. If a series of these models are stacked together vertically in a matrix, a composite laminate with negative Poisson's ratio is obtained.

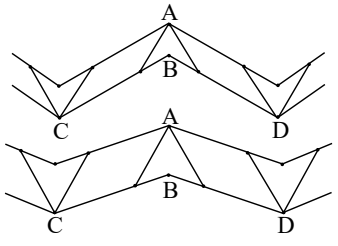

Fig. 7. *Rod and hinge model*

Auxetic composites can also be prepared by laminating unidirectional pre-preg tapes of epoxy resin reinforced with carbon fibers [47], or using fibre-reinforced Poly-Ether-Ether-Ketone (PEEK), which are then bonded together in the triangular auxetic core [48].

Composite sandwich panels which employ cellular auxetic material as a core can also be useful for applications in the aerospace industry [49].

1.4 Other Auxetic Geometries

Many other 2D auxetic geometries were developed and analysed in the past, but only a few 3D structures were investigated. Analytical formulas to calculate mechanical behaviour for 3D re-entrant structures were introduced by Choi and Lakes [50]. 3D structures of the rotating units [51] and nodule-fibril model [52] were also developed. Introduction of additive manufacturing techniques enables different and new 3D auxetic structures to be fabricated [53] and [54]. Interlocking hexagon models [55] are low porosity structures, which also exhibit auxetic behaviour. Auxetic yarns can find useful applications in composites and textiles [56].

2 FABRICATION

Structural auxetic materials can be made from a variety of metals or polymers using different manufacturing procedures. First manufactured auxetic material was re-entrant structure produced by Lakes in 1987 from conventional polymer foam [22]. This procedure is based on triaxial compression and heat treatment of the polymer foam, and was further developed for producing bigger specimens [57]. Similar procedures using solvent instead of heat treatment were also developed [58] with the added advantage that the auxetic foams can be transformed back to the conventional form.

Fabrication of the UHMWPE microporous polymers is done in the following steps: powder compaction, sintering and extrusion. The process is similar in case of the PTFE microporous polymers where the sintered part is rapidly stretched in the axial direction instead of being extruded [25].

Two different molecular design approaches are used to produce organic (molecular) auxetic materials: liquid crystal polymers (LCP) [30], [31] and [59], and three-dimensional tessellated polymer networks [15].

Large auxetic re-entrant honeycomb specimens can be produced with Kevlar fabric and epoxy using the Kirigami manufacturing process [60].

Additive manufacturing technologies offer new manufacturing procedure to make large parts and structures with complex geometries from various metals and plastics [53] and [61], which can be optimised using modern computational tools [41] and [62].

3 MECHANICAL PROPERTIES

The effect of Poisson's ratio on mechanical behaviour of an isotropic material can be derived from Eq. (1), with the Young's modulus assumed to be constant [63]:

$$G = K\frac{3(1-2\nu)}{2(1+\nu)}, \tag{1}$$

where G is the shear modulus (material response to shear stress), K is bulk modulus (material response to volumetric stress) and ν is Poisson's ratio.

From Eq. (1) it can be seen that materials with a Poisson's ratio approaching 0.5 (i.e. rubber) readily undergo shear deflections but resist volumetric deformations. When Poisson's ratio approaches the negative limit of −1 for isotropic materials, the shear modulus approaches infinite value and the material

preserves the shape during loading – material is strong in shear but easy to deform. At this point it must be pointed out that these relationships are valid only for isotropic materials, since in the case of anisotropic materials the bounds on Poisson's ratio are larger, theoretically $-\infty < \nu < \infty$ [63].

During elastic deformations auxetic materials do not preserve the volume: in the case of tensile deformations the volume of the material increases and vice-versa. This applies to the deformation behaviour before the material reaches yield stress and thereafter the material preserves the volume reached at yield, since the Poisson's ratio does not affect the deformation behaviour during material yielding.

Auxetic materials with Poisson's ratio near minus 1 resist indentation better than conventional materials, because the indentation resistance is inversely proportional to $(1-\nu^2)$. Enhanced indentation resistance has been proven through investigation of polymeric [64], metallic [65] foams and microporous polymers [66]. In case of impact, non-auxetic materials "flow" away from the impact area, while they "flow" towards the impact zone in case of auxetic materials. This makes the auxetic materials more dense at the impact zone and therefore more resistant to indentation [67].

The characterisation of the mechanical behaviour different auxetic structures has so far been carried out mainly using analytical methods and compressive or tensile testing to determine Poisson's ratio, Young's modulus and energy absorption capabilities [68]. Three-point bending tests were also performed on different structures manufactured by the rapid prototyping [69], electron beam melting (EBM) [70] and Directionally Reinforced Integrated Single-yarn (DIRIS) concept [48]. Dynamic tests of auxetic materials were performed using indentation of the cylinder and ball [64], and, ballistic tests [71].

Experimentally determined values of Poisson's ratio and Young's modulus for different auxetic materials are shown in Table 1. The listed values are the maximum values measured in specimens with different porosities and at different strains [23] and [53].

From Table 1 it can be seen that almost all of the experimentally determined values for the Poisson's ratios in different materials and structures lie in the range from minus 0.6 to minus 1.2. In only a few cases are values smaller than minus 1.2, because of material anisotropy. Values of the Young's modulus are given in lesser number of sources than Poisson's ratio, but it can be seen that structures produced with electron beam melting (EBM) methods from Ti6Al4V alloy are very stiff in comparison with any other material, but they are also very brittle because of the production method [75].

Table 1. *Mechanical properties of different auxetic materials*

Material		Poisson's ratio [-]	Young's modulus [MPa]
Transform. conventional open-cell foam	[22]	–0.7	0.072
	[50]	–0.8	-
	[57]	–0.82	-
Re-entrant copper foam	[72] and [73]	–0.39	30
Re-entrant silicon rubber foam	[73]	–0.25	26
PTFE	[23]	–12	0.15
UHMWPE	[25]	–1.24	-
6-chiral	[35]	~–1	-
	[36]	–0.81	19.46
Anti 4-chiral	[36]	–0.98	3.11
		–0.26	7.08
Anti 4-chiral	[69]	–1.831	5.374
Missing rib	[33] and [34]	–0.6	-
Polypropylene film	[74]	–1.12	340
Structures produced with EBM	[53]	–0.4	~8000
	[75]	–1,899	5085.3
3D printed re-entrant lattice	[54]	–1.18	-
Square array with voids	[32]	–0.73	-
Hierarchical honeycomb	[76]	–0.5	-
Rotating squares film	[77]	–0.963	-

4 APPLICATIONS

The auxetic materials have improved the shear performance (increased shear modulus) [78], damping, sound [79] (also with control of bands [80]) and energy absorption [64] and [71] of structural components, which makes them particularly useful for many special applications.

They are being increasingly used in body and vehicle armour applications in sandwich plates for ballistic protection in combination with other materials [81] and [82] fiber composites for greater pull-out resistance (applied tension pull-out force causes increase of cross section area), increased sensitivity piezoelectric composites, new kinds of fasteners, which transversally contract when pushed into a socket (compression load) and expand when attempted to be removed (tension load) [72], flexible pads to reduce impact forces upon small (elbow) and large objects (leg, human torso) [63] which can also be used for sports applications [83], more comfortable textiles with reduced clothing pressure, medical devices (especially bandages) and fashion

applications [84] and [85], promising and interesting medical application of auxetic materials such as in stents [77]. Very interesting applications in automotive and aerospace engineering are also in double curved sandwich structures, where the advantage of some auxetic material plates to deform in a convex shape (synclastic curvature) is exploited [22] and [86]. Also the out-of-plane strength and stiffness of the auxetic core materials are maximized, since the ribs are always aligned normal to the curved surface [49]. Another interesting application in aerospace engineering shows morphing wings using auxetic structures [87].

There are some examples where auxetic materials are used for thermal protection in aerospace applications (pyrolytic graphite) and vanes for aircraft turbine engines (large single crystals of Ni3Al) [88].

5 CONCLUSIONS

The paper gives an overview of fabrication, characterisation, properties and current applications of existing auxetic cellular materials with monotonous internal cellular structure. The response of auxetic materials to dynamic impact loading conditions at different strain rates is not yet sufficiently characterised and needs to be further investigated.

New advanced additive manufacturing techniques provide means to fabricate the next generation of auxetic materials with functionally graded porosity, which can be adapted to the requirements of a particular engineering application by computational simulations and optimization techniques. Such specifically designed internal cellular structure of auxetic materials provides the best desired mechanical response to particular loading conditions. This response can for example result in constant deceleration of impacting projectile or constant reaction force on structures, which is very useful for different applications in defence engineering and crashworthiness.

The auxetic cellular materials and structures show huge potential to become important light-weight structural materials of the future with further development of additive manufacturing technologies or with introduction of some new, more cost effective manufacturing techniques.

6 ACKNOWLEDGEMENTS

The paper was produced within the framework of research programme P2-063 entitled "Design of Porous Structures", which is financed by the Slovenian Research Agency "ARRS".

7 REFERENCES

[1] Gibson, L.J., Ashby, M.F. (1997). Cellular Solids: Structure and Properties. Cambridge University Press, Cambridge, DOI:10.1017/CBO9781139878326.

[2] Ashby, M.F., Evans, A., Fleck, N., Gibson, L.J., Hutchinson, J.W., Wadley, H.N. (2000). *Metal Foams: A Design Guide*. Elsevier Science, Burlington.

[3] Banhart, J. (2001). Manufacture, characterisation and application of cellular metals and metal foams. *Progress in Materials Science*, vol. 46, no. 6, p. 559-632, DOI:10.1016/S0079-6425(00)00002-5.

[4] Schwartz, D.S., Shih, D.S., Evans, A.G., Wadley, H.N.G. (1998). Porous and cellular materials for structural applications. *Materials Research Society Symposium Proceedings*, vol. 521.

[5] Duarte, I., Vesenjak, M., Krstulović-Opara, L., Ren, Z. (2015). Static and dynamic axial crush performance of in-situ foam-filled tubes. *Composite Structures*, vol. 124, p. 128-39, DOI:10.1016/j.compstruct.2015.01.014.

[6] Tanaka, S., Hokamoto, K., Irie, S., Okano, T., Ren, Z., Vesenjak, M., Itoh, S. (2011). High-velocity impact experiment of aluminum foam sample using powder gun. *Measurement*, vol. 44, no. 10, p. 2185-2189, DOI:10.1016/j.measurement.2011.07.018.

[7] Vesenjak, M., Kovačič, A., Tane, M., Borovinšek, M., Nakajima, H., Ren, Z. (2012). Compressive properties of lotus-type porous iron. *Computational Materials Science*, vol. 65, p. 37-43, DOI:10.1016/j.commatsci.2012.07.004.

[8] Vesenjak, M., Hokamoto, K., Matsumoto, S., Marumo, Y., Ren, Z. (2016). Uni-directional porous metal fabricated by rolling of copper sheet and explosive compaction. *Materials Letters*, vol. 170, p. 39-43, DOI:10.1016/j.matlet.2016.01.143.

[9] Sanders, W.S., Gibson, L.J. (2003). Mechanics of BCC and FCC hollow-sphere foams. *Materials Science and Engineering: A*, vol. 352, no. 1-2, p. 150-161, DOI:10.1016/S0921-5093(02)00890-0.

[10] Vesenjak, M., Fiedler, T., Ren, Z., Öchsner, A. (2009). Dynamic behaviour of metallic hollow sphere structures. Öechsner, A., Augustin, C. (eds.). *Multifunctional Metallic Hollow Sphere Structures*, p. 137-158, Springer-Verlag, Berlin, Heidelberg, DOI:10.1007/978-3-642-00491-9_8.

[11] Stöbener, K., Baumeister, J., Rausch, G., Rausch, M. (2005). Forming metal foams by simpler methods for cheaper solutions. *Metal Powder Report*, vol. 60, no. 1, p. 12-14, 16, DOI:10.1016/S0026-0657(05)00316-4.

[12] Vesenjak, M., Gačnik, F., Krstulović-Opara, L., Ren, Z. (2011). Behavior of composite advanced pore morphology foam. *Journal of Composite Materials*, vol. 45, no. 26, p. 2823-2831, DOI:10.1177/0021998311410489.

[13] Sulong, M.A., Vesenjak, M., Belova, I.V., Murch, G.E., Fiedler, T. (2014). Compressive properties of advanced pore morphology (APM) foam elements. *Materials Science and Engineering: A*, vol. 607, p. 498-504, DOI:10.1016/j.msea.2014.04.037.

[14] Fung, Y.C. (1965). *Foundations of Solid Mechanics*. Prentice-Hall, Englewood Cliffs.

[15] Evans, K.E., Nkansah, M.A., Hutchinson, I.J., Rogers, S.C. (1991). Molecular Network Design. *Nature*, vol. 353, p. 124, DOI:10.1038/353124a0.

[16] Yeganeh-Haeri, A., Weidner, D.J., Parise, J.B. (1992). Elasticity of a-cristobalite: A silicon dioxide with a negative Poisson's ratio. *Science*, vol. 257, no. 5070 p. 650-652, **DOI:10.1126/science.257.5070.650**.

[17] Lees, C., Vincent, J.F., Hillerton, J.E. (1991). Poisson's ratio in skin. *Bio-Medical Materials and Engineering*, vol. 1, no. 1, p. 19-23, **DOI:10.3233/BME-1991-1104**.

[18] Voigt, W. (1928). *Lehrbuch der Kristallphysik (mit Ausschluss der Kristalloptik)*. B.G. Teubner, Leipzig, Berlin.

[19] Muto, K., Bailey, R.W., Mitchell, K.J. (1963). Special requirements for the design of nuclear power stations to withstand earthquakes. *Proceedings of the Institution of Mechanical Engineers*, vol. 177, no, 1, p. 155-203, **DOI:10.1243/PIME_PROC_1963_177_018_02**.

[20] Almgren, R.F. (1985). An isotropic three-dimensional structure with Poisson's ratio=–1. Journal of Elasticity, vol. 15, no. 4, p. 427-430, **DOI:10.1007/BF00042531**.

[21] Gibson, L.J., Ashby, M.F., Schajer, G.S., Robertson, C.I. (1982). The mechanics of two-dimensional cellular material. *Proceedings of the Royal Society A*, no. 382, p. 25-45, **DOI:10.1098/rspa.1982.0087**.

[22] Lakes, R. (1987). Foam Structures with a Negative Poisson's Ratio. *Science*, vol. 235, no. 4792, p. 1038-1040, **DOI:10.1126/science.235.4792.1038**.

[23] Caddock, B.D., Evans, K.E. (1989). Microporous materials with negative Poisson's ratios. I. Microstructure and mechanical properties. *Journal of Physics D: Applied Physics*, vol. 22, no. 12, p. 1877-1882, **DOI:10.1088/0022-3727/22/12/012**.

[24] Evans, K.E., Caddock, B.D. (1989). Microporous materials with negative Poisson's ratios. II. Mechanisms and interpretation. *Journal of Physics D. Applied Physics*, vol. 22, p. 1883-1887, **DOI:10.1088/0022-3727/22/12/013**.

[25] Alderson, K.L., Evans, K.E. (1992). The fabrication of microporous polyethylene having a negative Poisson's ratio. *Polymer*, vol. 33, no. 20, p. 4435-8, **DOI:10.1016/0032-3861(92)90294-7**.

[26] Milton, G.W. (1992). Composite materials with poisson's ratios close to –1. *Journal of the Mechanics and Physics of Solids*, vol. 40, no. 5, p. 1105-1137, **DOI:10.1016/0022-5096(92)90063-8**.

[27] Grima, J.N., Evans, K.E. (2000). Auxetic behavior from rotating squares. *Journal of Materials Science Letters*, vol. 19, no. 17, p. 1563-1565, **DOI:10.1023/A:1006781224002**.

[28] Masters, I.G., Evans, K.E. (1996). Models for the elastic deformation of honeycombs. *Composite Structures*, vol. 35, no. 4, p. 403-422, **DOI:10.1016/S0263-8223(96)00054-2**.

[29] Grima, J.N., Alderson, A., Evans, K.E. (2004). Negative Poisson'S ratios from rotating rectangles. *Computational Methods in Science and Technology*, vol. 10, no. 2, p. 137-145, **DOI:10.12921/cmst.2004.10.02.137-145**.

[30] Grima, J.N., Alderson, A., Evans, K.E. (2005). Auxetic behaviour from rotating rigid units. *Physica Status Solidi (B)*, vol. 242, no. 3, p. 561-575, **DOI:10.1002/pssb.200460376**.

[31] Grima, J.N., Zammit, V., Gatt, R., Alderson, A., Evans, K.E. (2007). Auxetic behaviour from rotating semi-rigid units. *Physica Status Solidi (B)*, vol. 244, no. 3, p. 866-882, **DOI:10.1002/pssb.200572706**.

[32] Taylor, M., Francesconi, L., Gerendás, M., Shanian, A., Carson, C., Bertoldi, K. (2013). Low porosity metallic periodic structures with negative Poisson's ratio. *Advanced Materials*, vol. 26, no. 15, p. 2365-2370, **DOI:10.1002/adma.201304464**.

[33] Smith, C.W., Grima, J.N., Evans, K.E. (2000). A novel mechanism for generating auxetic behaviour in reticulated foams: missing rib foam model. *Acta Materialia*, vol. 48, no. 17, p. 4349-4356, **DOI:10.1016/S1359-6454(00)00269-X**.

[34] Gaspar, N., Ren, X.J., Smith, C.W., Grima, J.N., Evans, K.E. (2005). Novel honeycombs with auxetic behaviour. *Acta Materialia*, vol. 53, no. 8, p. 2439-2445, **DOI:10.1016/j.actamat.2005.02.006**.

[35] Prall, D., Lakes, R.S. (1997). Properties of a chiral honeycomb with a poisson's ratio of –1. *International Journal of Mechanical Sciences*, vol. 39, no. 3, p. 305-314, **DOI:10.1016/S0020-7403(96)00025-2**.

[36] Alderson, A., Alderson, K.L., Attard, D., Evans, K.E., Gatt, R., Grima, J.N., Miller, W., Ravirala, N., Smith, C.W., Zied, K. (2010). Elastic constants of 3-, 4- and 6-connected chiral and anti-chiral honeycombs subject to uniaxial in-plane loading. *Composites Science and Technology*, vol. 70, no. 7, p. 1042-1048, **DOI:10.1016/j.compscitech.2009.07.009**.

[37] Theocaris, P.S., Stavroulakis, G.E., Panagiotopoulos, P.D. (1997). Negative Poisson's ratios in composites with star-shaped inclusions: a numerical homogenization approach. *Archive of Applied Mechanics*, vol. 67, no. 4, p. 274-286, **DOI:10.1007/s004190050117**.

[38] Larsen, U.D., Sigmund, O., Bouwstra, S. (1997). Design and fabrication of compliant micromechanisms and structures with negative Poisson's ratio. *Journal of Microelectromechanical Systems*, vol. 6, no. 2, p. 99-106, **DOI:10.1109/84.585787**.

[39] Shan, S., Kang, S.H., Zhao, Z., Fang, L., Bertoldi, K. (2015). Design of planar isotropic negative Poisson's ratio structures. *Extreme Mechanics Letters*, vol. 4, p. 96-102, **DOI:10.1016/j.eml.2015.05.002**.

[40] Cho, Y., Shin, J.-H., Costa, A., Kim, T.A., Kunin, V., Li, J., Lee, S.Y., Yang, S., Han, H.N., Choi, I.-S., Srolovitz, D.J. (2014). Engineering the shape and structure of materials by fractal cut. *Proceedings of the National Academy of Sciences of the United States of America*, vol. 111, no. 49, p. 17390-17395, **DOI:10.1073/pnas.1417276111**.

[41] Körner, C., Liebold-Ribeiro, Y. (2015). A systematic approach to identify cellular auxetic materials. *Smart Materials and Structures*, vol. 24, no. 2, p. 025013, **DOI:10.1088/0964-1726/24/2/025013**.

[42] Alderson, A., Evans, K.E. (1995). Microstructural modelling of auxetic microporous polymers. *Journal of Materials Science*, vol. 30, no. 13, p. 3319-3332, **DOI:10.1007/BF00349875**.

[43] Alderson, A., Evans, K.E. (1997). Modelling concurrent deformation mechanisms in auxetic microporous polymers. *Journal of Materials Science*, vol. 32, no. 11, p. 2797-2809, **DOI:10.1023/A:1018660130501**.

[44] Grima, J.N., Williams, J.J., Evans, K.E. (2005). Networked calix[4]arene polymers with unusual mechanical properties. *Chemical Communications*, vol. 1, p. 4065-4067, **DOI:10.1039/b505839b**.

[45] He, C., Liu, P., Griffin, A.C. (1998). Toward Negative Poisson Ratio Polymers through Molecular Design. *Macromolecules*, vol. 31, no. 9, p. 3145-3147, **DOI:10.1021/ma970787m**.

[46] Yao, Y.T., Uzun, M., Patel, I. (2011). Workings of auxetic nano-materials. *Journal of Achievements in Materials and Manufacturing Engineering*, vol. 49, no. 2, p. 585-593.

[47] Clarke, J.F., Duckett, R.A., Hine, P.J., Hutchinson, I.J., Ward, I.M. (1994). Negative Poisson's ratios in angle-ply laminates: theory and experiment. *Composites*, vol. 25, no. 9, p. 863-868, **DOI:10.1016/0010-4361(94)90027-2**.

[48] Michelis, P., Spitas, V. (2010). Numerical and experimental analysis of a triangular auxetic core made of CFR-PEEK using the Directionally Reinforced Integrated Single-yarn (DIRIS) architecture. *Composites Science and Technology*, vol. 70, no. 7, p. 1064-1071, **DOI:10.1016/j.compscitech.2010.01.013**.

[49] Alderson, A., Alderson, K.L. (2007). Auxetic materials. *Proceedings of the Institution of Mechanical Engineers, Part G: Journal of Aerospace Engineering*, vol. 221, no. 4, p. 565-575, **DOI: 10.1243/09544100JAERO185**.

[50] Choi, J.B., Lakes, R.S. (1995). Nonlinear analysis of the Poisson's Ratio in negative Poisson's Ratio foams. *Journal of Composite Materials*, vol. 29, no. 1, p. 113-128, **DOI:10.1177/002199839502900106**.

[51] Alderson, A., Evans, K.E. (2001). Rotation and dilation deformation mechanisms for auxetic behaviour in the α-cristobalite tetrahedral framework structure. *Physics and Chemistry of Minerals*, vol. 28, no. 10, p. 711-718, **DOI:10.1007/s002690100209**.

[52] Gaspar, N., Smith, C.W., Alderson, A., Grima, J.N., Evans, K.E. (2011). A generalised three-dimensional tethered-nodule model for auxetic materials. *Journal of Materials Science*, vol. 46, no. 2, p. 372-384, **DOI:10.1007/s10853-010-4846-0**.

[53] Schwerdtfeger, J., Heinl, P., Singer, R.F., Körner, C. (2010). Auxetic cellular structures through selective electron beam melting. *Physica Status Solidi (B)*, vol. 247, no. 2, p. 269-272, **DOI:10.1002/pssb.200945513**.

[54] Critchley, R., Corni, I., Wharton, J.A., Walsh, F.C., Wood, R.J.K., Stokes, K.R. (2013). The preparation of auxetic foams by three-dimensional printing and their characteristics. *Advanced Engineering Materials*, vol. 15, no. 10, p. 980-985, **DOI:10.1002/adem.201300030**.

[55] Ravirala, N., Alderson, A., Alderson, K.L. (2007). Interlocking hexagons model for auxetic behaviour. *Journal of Materials Science*, vol. 42, no. 17, p. 7433-7445, **DOI:10.1007/s10853-007-1583-0**.

[56] Sloan, M.R., Wright, J.R., Evans, K.E. (2011). The helical auxetic yarn - A novel structure for composites and textiles; geometry, manufacture and mechanical properties. *Mechanics of Materials*, vol. 43, no. 9, p. 476-486, **DOI:10.1016/j.mechmat.2011.05.003**.

[57] Chan, N., Evans, K.E. (1997). Fabrication methods for auxetic foams. *Journal of Materials Science*, vol. 32, no. 22, p. 5945-5953, **DOI:10.1023/A:1018606926094**.

[58] Grima, J.N., Attard, D., Gatt, R., Cassar, R.N. (2009). A novel process for the manufacture of auxetic foams and for their re-conversion to conventional form. *Advanced Engineering Materials*, vol. 11, no. 7, p. 533-535, **DOI:10.1002/adem.200800388**.

[59] He, C., Liu, P., McMullan, P.J., Griffin, A.C. (2005). Toward molecular auxetics: Main chain liquid crystalline polymers consisting of laterally attached para-quaterphenyls. *Physica Status Solidi (B)*, vol. 242, no. 3, p. 576-584, **DOI:10.1002/pssb.200460393**.

[60] Hou, Y., Neville, R., Scarpa, F., Remillat, C., Gu, B., Ruzzene, M. (2014). Graded conventional-auxetic Kirigami sandwich structures: Flatwise compression and edgewise loading. *Composites Part B: Engineering*, vol. 59, p. 33-42, **DOI:10.1016/j.compositesb.2013.10.084**.

[61] Heinl, P., Körner, C., Singer, R.F. (2008). Selective electron beam melting of cellular titanium: Mechanical properties. *Advanced Engineering Materials*, vol. 10, no. 9, p. 882-888, **DOI:10.1002/adem.200800137**.

[62] Wang, F., Sigmund, O., Jensen, J.S. (2014). Design of materials with prescribed nonlinear properties. *Journal of the Mechanics and Physics of Solids*, vol. 69, p. 156-174, **DOI:10.1016/j.jmps.2014.05.003**.

[63] Lakes, R. (1993). Advances in negative Poisson's ratio materials. *Advanced Materials*, vol. 5, no. 4, p. 293-296, **DOI:10.1002/adma.19930050416**.

[64] Chan, N., Evans, K.E. (1998). Indentation resilience of conventional and auxetic foams. *Journal of Cellular Plastics*, vol. 34, no. 3, p. 231-260, **DOI:10.1177/0021955X9803400304**.

[65] Lakes, R.S., Elms, K. (1993). Indentability of conventional and negative Poisson's ratio foams. *Journal of Composite Materials*, vol. 27, no. 12, p. 1193-1202, **DOI:10.1177/002199839302701203**.

[66] Alderson, K.L., Fitzgerald, A., Evans, K.E. (2000). The strain dependent indentation resilience of auxetic microporous polyethylene. *Journal of Materials Science*, vol. 35, no. 16, p. 4039-4047, **DOI:10.1023/A:1004830103411**.

[67] Alderson, A. (1999). A triumph of lateral thought. *Chemistry and Industry*, vol. 10, p. 384-391.

[68] Scarpa, F., Pastorino, P., Garelli, A., Patsias, S., Ruzzene, M. (2005). Auxetic compliant flexible PU foams: static and dynamic properties. *Physica Status Solidi (B)*, vol. 242, no. 3, p. 681-694, **DOI:10.1002/pssb.200460386**.

[69] Chen, Y.J., Scarpa, F., Liu, Y.J., Leng, J.S. (2013). Elasticity of anti-tetrachiral anisotropic lattices. *International Journal of Solids and Structures*, vol. 50, no. 6, p. 996-1004, **DOI:10.1016/j.ijsolstr.2012.12.004**.

[70] Horn, T.J., Harrysson, O.L.A., Marcellin-Little, D.J., West, H.A., Lascelles, B.D.X., Aman, R. (2014). Flexural properties of Ti6Al4V rhombic dodecahedron open cellular structures fabricated with electron beam melting. *Additive Manufacturing*, vol. 1-4, p. 2-11, **DOI:10.1016/j.addma.2014.05.001**.

[71] Yang, S., Qi, C., Wang, D., Gao, R., Hu, H., Shu, J. (2013). A comparative study of ballistic resistance of sandwich panels with aluminum foam and auxetic honeycomb cores. *Advances in Mechanical Engineering*, vol. 5, p. 589216, **DOI:10.1155/2013/589216**.

[72] Choi, J.B., Lakes, R.S. (1991). Design of a fastener based on negative Poisson's ratio foam. *Cellular Polymers*, vol. 10, p. 205-212.

[73] Friis, E.A., Lakes, R.S., Park, J.B. (1988). Negative Poisson's ratio polymeric and metallic foams. *Journal of Materials*

Science, vol. 23, no. 12, p. 4406-4414, **DOI:10.1007/BF00551939**.

[74] Ravirala, N., Alderson, A., Alderson, K.L., Davies, P.J. (2005). Auxetic polypropylene films. *Polymer Engineering & Science*, vol. 45, no. 4, p. 517-528, **DOI:10.1002/pen.20307**.

[75] Yang, L., Harrysson, O., West, H., Cormier, D. (2012). Compressive properties of Ti–6Al–4V auxetic mesh structures made by electron beam melting. *Acta Materialia*, vol. 60, no. 8, p. 3370-3379, **DOI:10.1016/j.actamat.2012.03.015**.

[76] Mousanezhad, D., Babaee, S., Ebrahimi, H., Ghosh, R., Hamouda, A.S., Bertoldi, K., Vaziri, A. (2015). Hierarchical honeycomb auxetic metamaterials. *Scientific Reports*, vol. 5, p. 18306, **DOI:10.1038/srep18306**.

[77] Ali, M.N., Busfield, J.J.C., Rehman, I.U. (2014). Auxetic oesophageal stents: structure and mechanical properties. *Journal of Materials Science: Materials in Medicine*, vol. 25, no. 2, p. 527-553, **DOI:10.1007/s10856-013-5067-2**.

[78] Yang, W., Li, Z.M., Shi, W., Xie, B.H., Yang, M.B. (2004). On auxetic materials. *Journal of Materials Science*, vol. 39, no. 10, p. 3269-3279, **DOI:10.1023/B:JMSC.0000026928.93231.e0**.

[79] Scarpa, F., Ciffo, L.G., Yates, J.R. (2004). Dynamic properties of high structural integrity auxetic open cell foam. *Smart Materials and Structures*, vol. 13, no. 1, p. 49-56, **DOI:10.1088/0964-1726/13/1/006**.

[80] Krödel, S., Delpero, T., Bergamini, A., Ermanni, P., Kochmann, D.M. (2014). 3D auxetic microlattices with independently controllable acoustic band gaps and quasi-static elastic moduli. *Advanced Engineering Materials*, vol. 16, no. 4, p. 357-363, **DOI:10.1002/adem.201300264**.

[81] Imbalzano, G., Tran, P., Ngo, T.D., Lee, P.V.S. (2015). A Numerical Study of Auxetic Composite Panels under Blast Loadings. *Composite Structures*, vol. 135, p. 339-352, **DOI:10.1016/j.compstruct.2015.09.038**.

[82] Imbalzano, G., Tran, P., Ngo, T.D., Lee, P. V. (in press). Three-dimensional modelling of auxetic sandwich panels for localised impact resistance. *Journal of Sandwich Structures and Materials*, **DOI:10.1177/1099636215618539**.

[83] Sanami, M., Ravirala, N., Alderson, K., Alderson, A. (2014). Auxetic materials for sports applications. *Procedia Engineering*, vol. 72, p. 453-458, **DOI:10.1016/j.proeng.2014.06.079**.

[84] Wright, J.R., Burns, M.K., James, E., Sloan, M.R., Evans, K.E. (2012). On the design and characterisation of low-stiffness auxetic yarns and fabrics. *Textile Research Journal*, vol. 82, no. 7, p. 645-654, **DOI:10.1177/0040517512436824**.

[85] Rant, D., Rijavec, T., Pavko Čuden, A. (2013). Auxetic textiles. *Acta Chimica Slovenica*, vol. 60, no. 4, p. 715-723.

[86] Evans, K.E. (1991). The design of doubly curved sandwich panels with honeycomb cores. *Composite Structures*, vol. 17, no. 2, p. 95-111, **DOI:10.1016/0263-8223(91)90064-6**.

[87] Airoldi, A., Crespi, M., Quaranti, G., Sala, G. (2012). Design of a morphing airfoil with composite chiral structure. *Journal of Aircraft*, vol. 49, no. 4, p. 1008-1019, **DOI:10.2514/1.C031486**.

[88] Evans, K.E., Alderson, A. (2000). Auxetic materials: Functional materials and structures from lateral thinking! *Advanced Materials*, vol. 12, no. 9, p. 617-628, **DOI:10.1002/(SICI)1521-4095(200005)12:9<617::AID-ADMA617>3.0.CO;2-3**.

Strojniški vestnik - Journal of Mechanical Engineering 62(2016)9, 494-502
DOI:10.5545/sv-jme.2015.3016
Original Scientific Paper
Received for review: 2015-09-13
Received revised form: 2016-04-08
Accepted for publication: 2016-05-09

The Bond Graph Method for Analysis of the Micro-Motion Characteristics of a Micro Gripper

Chao Lin[1,*] – Yi-hang Ren[1] – Jiu-xiang Ji[1] – Li-zhong Cai[1] – Ji-ming Shao[2]
[1]Chongqing University, The State Key Laboratory of Mechanical Transmission, China
[2]Shanghai Key Laboratory of Spacecraft Mechanism, China

A full-flexure micro gripper with three-stage amplification has been designed. The pseudo-rigid-body (PRB) model of a bridge-type amplification mechanism (BTAM) and micro gripper are established; the input/output stiffness of the BTAM are deduced on the use of the compliant mechanism, Castigliano's theorem and the PRB method. The characteristic equations and state-space equations of the micro gripper are derived on the basis of bond graph theory. The displacement simulation curve and flexible hinge angular simulation curve of the micro gripper are acquired through Matlab R2013b programming. Ansys13.0 finite element simulation software is utilized for simulation analysis of the micro gripper micro-motion. The micro gripper is 3D printed using laser rapid prototyping technology, and a test bench has been set up. The experimental value, finite element analysis value, and Matlab simulation value are comparatively analysed, and the change rules are essentially the same. As a result, the validity of the bond graph model of the micro gripper is verified, and providing a new effective method for the flexible mechanism analysis.

Keywords: micro gripper, pseudo-rigid-body (PRB), flexure hinge, bond graph, Matlab R2013b, 3D print

Highlights

- *A full-flexure micro gripper with three-stage amplification has been designed.*
- *The bond graph model of the micro gripper has been set up, the characteristic equations and state equations of the micro gripper are derived.*

0 INTRODUCTION

In recent years, with the rapid development of science and technology, micro/nanotechnology has been becoming a key direction in research around the world. The demand for micro-motion devices has increased in many industrial applications, particularly in the fields of manipulating biological cells, microsurgical operation and assembling micro-machines. With the operation objects trending towards miniaturization, developing flexible, high precision and easily control microrobots are becoming an urgent requirement, and micro-manipulating robots combined with micro-positioning technology and robot technology are receiving increased attention **[1]** and **[2]**. According to the driving principle, micro grippers can be roughly divided into five categories: electrothermal actuators **[3]**, electrostatic actuators **[4]**, piezoelectric actuators (PZTs) **[5]**, shape memory alloy (SMA) actuators **[6]**, and electromagnetic actuators **[7]**. PZTs are widely used because they have many advantages such as stable output displacement, great output force, high resolution, high response speed and are easy to control **[8]** and **[9]**. Nah and Zhong **[9]** designed a monolithic compliant-flexure-based micro gripper, of which the displacement amplification and maximum stroke are 3.0 μm and 170 μm, respectively. Zubir et al. **[10]** developed a compliant-based micro gripper for high precision manipulation; a high displacement amplification and a maximum stroke of 100 μm can be achieved. Ramadan et al. **[11]** proposed a chopstick-like two-fingered micromanipulator based on a hybrid mechanism for cell manipulation. Xiao et al. **[12]** presented a micro gripper which has absolutely parallel movement of the gripping arms; the displacement amplification ratio is about 10, μm, and the micro gripper arm maximum stroke is 300 μm. Yu et al. **[13]** studied a piezoelectric-based micro gripper of which the displacement amplification of one side can be 10.6, and the maximum output displacement is 261 μm. Furthermore, other micro grippers have been designed, such as a thin-walled copper tube by Li et al. **[14]**, a compliant piezoelectric actuator based micro gripper by Jain et al. **[15]**, a single active finger ionic polymer metal composite (IPMC) micro gripper by Ford et al. **[16]**, a rotary micro gripper with locking function by Hao et al. **[17]**, a piezoelectric actuator for micro gripper by Jain et al. **[18]**, and a piezoelectric-actuated micro gripper with a three-stage flexure-based amplification by Wang et. al **[19]**.

The transmission of flexible micro gripper motion depends on the deformation of the material, so the kinematic modelling accuracy is difficult to guarantee. Furthermore, it is difficult to obtain the specific state change of a single internal component of the micro gripper. The bond graph is put forward by Paynter, describing the transmission, storage, conversion and consumption of power **[20]**. The nonlinearity of

*Corr. Author's Address: State Key Laboratory of Mechanical Transmission, Chongqing University, Chongqing, China, linchao@cqu.edu.cn

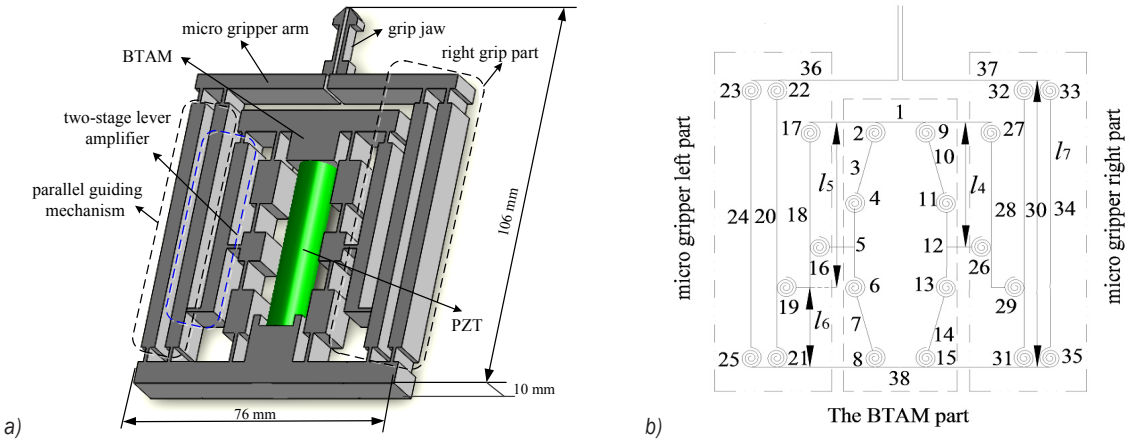

Fig. 1. *Schematic diagram of micro gripper; a) geometrical model, and b) PRB model*

systems can be intuitively considered in the bond graph method, and state variables in the model are all physical variables; thus, the state changes of the system can be further described. Moreover, the superiority of consistency between the bond graph and systematic state equations is significant. The corresponding mathematical model can be acquired by the bond graph of the system [21]. At present, bond graph modelling has been applied in the analysis of the Stewart platform mechanism [22]; however, the use of bond graph theory to analyse the flexible mechanism remains to be further developed.

Given the advantages of the bond graph in complex system physical model analysis, the bond graph model of the micro gripper is built after the analysis of working principles of the flexible micro gripper, stiffness of the bridge type amplification mechanism (BTAM) and parallel-guiding mechanism (PGM). The characteristic equations and state-space equations are derived. Finally, the output displacement simulation curve and flexible hinge angular displacement simulation curve of the micro gripper are obtained by using Matlab simulation and analysis.

1 STRUCTURE DESIGN AND WORKING PRINCIPLE ANALYSIS OF THE MICRO GRIPPER

According to the basic theory of compliant mechanism and mechanical principles, a micro gripper mechanism with large output displacement is designed (as shown in Fig. 1). The dimension is 106 mm × 76 mm × 10 mm. The micro gripper is driven by PZTs; the input displacement provided by PZTs is amplified by BTAM, and further enlarged by a two-stage flexible lever. As a result, the micro gripper arm has a large stroke. Meanwhile, the parallel-guiding mechanism ensures gripper arm maintains parallel movement and makes the grip jaw clip object more stably and firmly.

2 STATICS ANALYSIS OF THE MICRO GRIPPER

2.1 Input Stiffness of the Micro Gripper

According to the PRB method, a BTAM can be divided into 16 components, and each component is connected by a flexure hinge without clearance. The flexure hinge is equivalent to torsional spring, and the rest of the components are equivalent to a rigid rod. A quarter of the BTAM is taken for analysis because it is entirely symmetrical in structure. The PRB model and force analysis of BTAM are shown in Fig. 2.

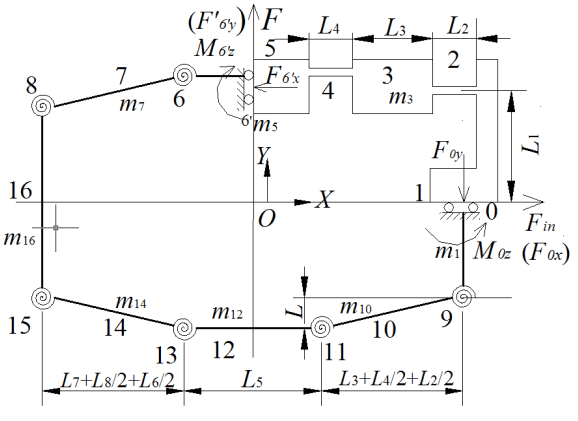

Fig. 2. *Graph of PRB model and 1/4 model force analysis of BTAM*

Using Castigliano's theorem, input stiffness and output stiffness of BTAM were deduced by Lobontiu. The derivation process of input stiffness is the same as

in reference [23], in this paper, however, in order to simplify the calculation, the shear force of flexure hinge is ignored. The output stiffness can be obtained in the same way while assuming the force $F_{6'y}^{'}$ is applied to point 6′ when solving output stiffness. Flexible hinges 2 and 4 have the same dimension; hence, the compliance along the x-axis and around the z-axis of flexible hinge 2 are equal to that of flexible hinge 2 correspondingly. That is, $C_{x\text{-}F}^{2}=C_{x\text{-}F}^{4}$, $C_{\theta\text{-}M}^{2}=C_{\theta\text{-}M}^{4}$.

Based on the analysis and theoretical derivation, the input stiffness and output stiffness of BTAM can be expressed by:

$$\begin{cases} k_{in}=\dfrac{F_{0x}}{u_{0x}}=\dfrac{2}{4C_{x\text{-}F}^{2}+L^{2}C_{\theta\text{-}M}^{2}} \\ k_{out}=\dfrac{F_{6'y}^{'}}{u_{6'y}}=\dfrac{2}{\left(L_3+L_4\right)^{2}C_{\theta-M}^{2}} \end{cases}, \tag{1}$$

where $C_{\theta\text{-}M}^{2}=12L_2/(Ebt^3)$, $C_{x\text{-}F}^{2}=L_2/(Etb)$, t, L, and L_2 to L_5 are structural parameters of BTAM as shown in Fig. 2, b is thickness of BTAM.

According to the movement of the micro gripper, when the micro gripper is driven by PZTs, not only the BTAM produces elongation deformation, flexible hinge 16, 19, 26 and 29 also achieve bending deformation in the driving force direction. As a consequence, the input stiffness of the micro gripper includes the input stiffness of BTAM and the bending stiffness of flexure hinge, as,

$$K_{in}=k_{in}+\sum\frac{1}{C_{y-F}^{m}}, \tag{2}$$

where m = 16, 19, 26, 29, and $1/C_{y-F}^{m}$ is bending stiffness of flexure hinge m when it is under the force $F_{6'y}$ which is parallel to the cross section, and $1/C_{y-F}^{m}=Ebt^3/\left(6l^2\right)$, l is the length of flexure hinge.

3 THE BOND GRAPH MODEL OF MICRO GRIPPER

The energy conversion and transmission of interactional components are the basic foundations to set up the system bond graph in the engineering system. In the bond graph theory, the system with the co-existence of different forms of energy can be processed in a unified way; any system can be summarized into four state variables: flow variables $f(t)$, effort variables $e(t)$, generalized momentum $p(t)$, and generalized displacement $q(t)$.

Based on the theory and method of the bond graph, combined with the characteristics of the micro gripper driver and motion transmission, firstly the bond graph models, respectively, of BTAM, leverage, and PGM are set up; then the bond graph model of each part to set up the bond graph model of the microclamp is assembled. In the process of setting up the bond graph model of PGM, the rotary angles of the flexible hinges of PGM are assumed to be the same. For BTAM, it works as one end fixed while the other stretches, but in the bond graph model, both ends are assumed to stretch.

According to the transmission characteristics of the system and the causal relationships among different parts, considering generalized displacement $q(t)$ of capacitive component and generalized momentum $p(t)$ of inertial component as the state variables, $e(t)$ and $f(t)$ as the effort and flow of each bond., numbering each key from 1 to 82, the bond graph model of the micro gripper was established. The model is displayed in Fig. 4.

In Fig. 4, '0' connection and '1' connection stand for serial and parallel energy connections; the arrows indicate energy flow directions of the system. I, C and R represent the inertial component, capacitive component, and resistive component, respectively. Transformer (TF) helps to convert one type of motion to another. *Se* is driving force, K_{in} is input stiffness of the micro gripper, k_i, M_i, J_i and u_i represent stiffness, mass, the moment of inertia and damping coefficient, and the subscript label is the series number of parts in Fig. 1b. $k'=k_m=1/C_{\theta\text{-}M}^{2}$ $(m=2,4,6,8,9,11,13,15)$ is bending stiffness of flexure hinge of BTAM, $k''=k_n=1/C_{\theta\text{-}M}^{16}$ $(n=16,17,19,21,22,23,25,26,27,29,31,32,33,35)$ is bending stiffness of flexure hinge of PGM. $J'=J_j$ $(j=3,7,10,14)$ is the moment of inertia of the rigid rod of BTAM, $J''=J_k$ $(k=18,20)$ is moment of inertia of the rigid rod of lever, $J'''=J_p$ $(p=24,28,30,34)$ is the moment of inertia of the rigid rod of PGM. By mechanics of materials, $J=ml^2/12$.

4 THE ESTABLISHMENT OF THE STATE-SPACE EQUATIONS

The motion state of the system can be described by a set of state variables. State-space equations are the time-varying physical quantities of the system's internal state. As seen in Fig. 4, there are 30 energy-storage components in the system, including 16 capacitive components and 14 inertial components. In these components, I_{63} and I_{82} have differential causality, and the rest have integral causality. The BTAM has equivalent damping in the direction of a driving force, as do both the left and right parts of micro gripper; as a consequence, the system also has resistive components. From Fig. 4, characteristic equations can be obtained as follows.

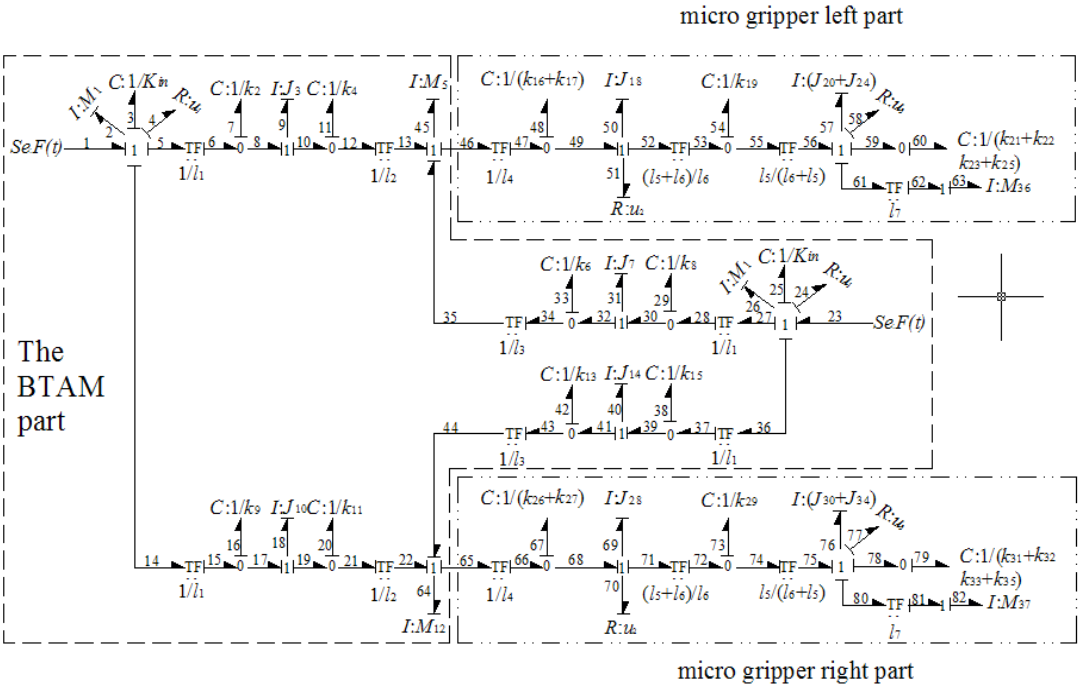

Fig. 3. *The bond graph model of micro gripper*

The characteristic equations of the resistive component are:

$$\begin{cases} e_4=f_4R_4, & e_{58}=f_{58}R_{58} \\ e_{24}=f_{24}R_{24}, & e_{70}=f_{70}R_{70} \\ e_{51}=f_{51}R_{51}, & e_{77}=f_{77}R_{77} \end{cases}. \tag{3}$$

The characteristic equations of the energy-storage components with integral causality are:

$$\begin{cases} f_2=\dfrac{1}{I_2}p_2 & \cdots & e_{60}=\dfrac{1}{C_{60}}q_{60} \\ e_3=\dfrac{1}{C_3}q_3 & \cdots & f_{64}=\dfrac{1}{I_{64}}p_{64} \\ \vdots & & \vdots \\ e_{16}=\dfrac{1}{C_{16}}q_{16} & \cdots & f_{76}=\dfrac{1}{I_{76}}p_{76} \\ f_{18}=\dfrac{1}{I_{18}}p_{18} & \cdots & e_{79}=\dfrac{1}{C_{79}}q_{79} \end{cases}. \tag{4}$$

The characteristic equations of the energy-storage components with differential causality are:

$$\begin{cases} e_{63}=I_{63}f_{63} \\ e_{82}=I_{82}f_{82} \end{cases}. \tag{5}$$

Assuming the system state variable is $\boldsymbol{X}=(p_2 \quad q_3 \quad q_7 \quad \cdots \quad q_{70} \quad p_{73} \quad q_{75})^T_{1\times 28}$, the subscript label of each state variable is the series number of bonds in Fig. 4. the state-space equations of a micro gripper can be deduced based on characteristic equations and characters of TF, connection '0' and '1'. Since 28 state variables exist in Eq. (4), the state-space equations correspondingly contain 28 differential equations. The state-space equations can be derived as:

$$\begin{cases} \dot{p}_2=se-e_3-e_4-e_5-e_{14}= \\ \quad =se-\dfrac{1}{C_3}q_3-R_4\dfrac{1}{I_2}p_2-\dfrac{1}{l_1C_7}q_7-\dfrac{1}{l_1C_{16}}q_{16} \\ \dot{q}_3=f_2=\dfrac{1}{I_2}p_2 \\ \dot{q}_7=f_6-f_8=\dfrac{1}{l_1I_2}p_2-\dfrac{1}{I_9}p_9 \\ \quad \vdots \\ \dot{q}_{73}=f_{72}-f_{74}=\dfrac{l_5+l_6}{l_6}\dfrac{1}{I_{69}}p_{69}-\dfrac{l_5+l_6}{l_5}\dfrac{1}{I_{76}}p_{76} \\ \dot{p}_{76}=\dfrac{I_{76}}{I_{76}+l_7^2I_{82}}(e_{75}-e_{77}-e_{78})= \\ \quad =\dfrac{I_{73}}{I_{73}+l_7^2I_{78}}(\dfrac{l_5+l_6}{l_5}\dfrac{1}{C_{73}}q_{73}-R_{77}\dfrac{1}{I_{76}}p_{76}-\dfrac{1}{C_{79}}q_{79}) \\ \dot{q}_{79}=f_{78}=f_{76}=\dfrac{1}{I_{76}}p_{76} \end{cases}. \tag{6}$$

In Eq. (3), the subscript labels of I, C and R are a series number of bonds, and $l_1=L$, $l_2=l_3=L_3+L_4/2+$ $+L_2/2$, l_5 and l_6 are structural parameters of lever-PGM, M is the quality of the translational components, and $M=m_1+m_{18}+m_{28}$, the subscript label is the series number of parts in Fig. 1b. μ is equivalent damping of BATM, μ_1 is equivalent damping of lever- PGM mechanism.

5 PROCESSING, SIMULATION, AND EXPERIMENT

5.1 Processing of the Micro Gripper

Laser rapid prototyping technology an additive manufacturing processing method; also known as "3D printing, it is a new manufacturing technology that integrates CAD, CNC, laser technology, automatic control technology, new materials and other advanced technologies. It has become widely used in machinery manufacturing, aerospace, medical and other fields. Because of the simple structure of the micro gripper, the 3D printing process of the micro gripper is more convenient. The micro gripper is processed through the EOS M280 laser molten sintering moulding machine, and separated from the base plate by using Wire EDM; the machining process is shown in Fig. 5. TC4 titanium alloy is chosen as the material of the micro gripper because of its good comprehensive properties, good plasticity and durability, and high-temperature deformation performance.

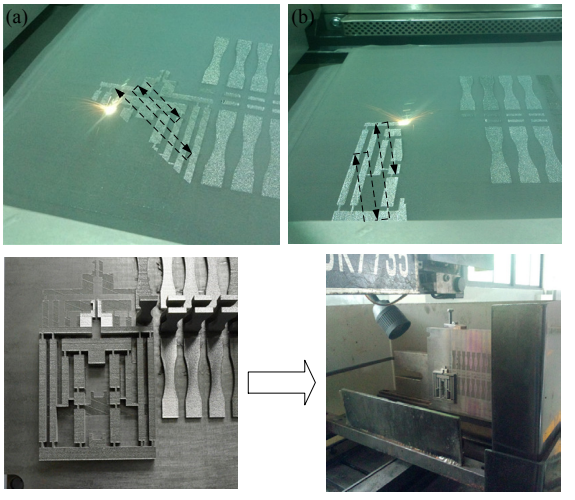

Fig. 4. *Processing of the micro gripper; a) 3D printing of the micro gripper and b) wire EDM processing*

5.2 The Finite Element Simulation and Solution of State Equations

The micro gripper is simulated and analysed with Ansys 13.0; the bottom is selected as fixed support, the mesh plots and working simulation diagram are shown in Fig. 5.

A variable order Adams PECE algorithm is a commonly used method for solving ordinary differential equations. It has the advantages of high precision, simple procedure, and stable calculation

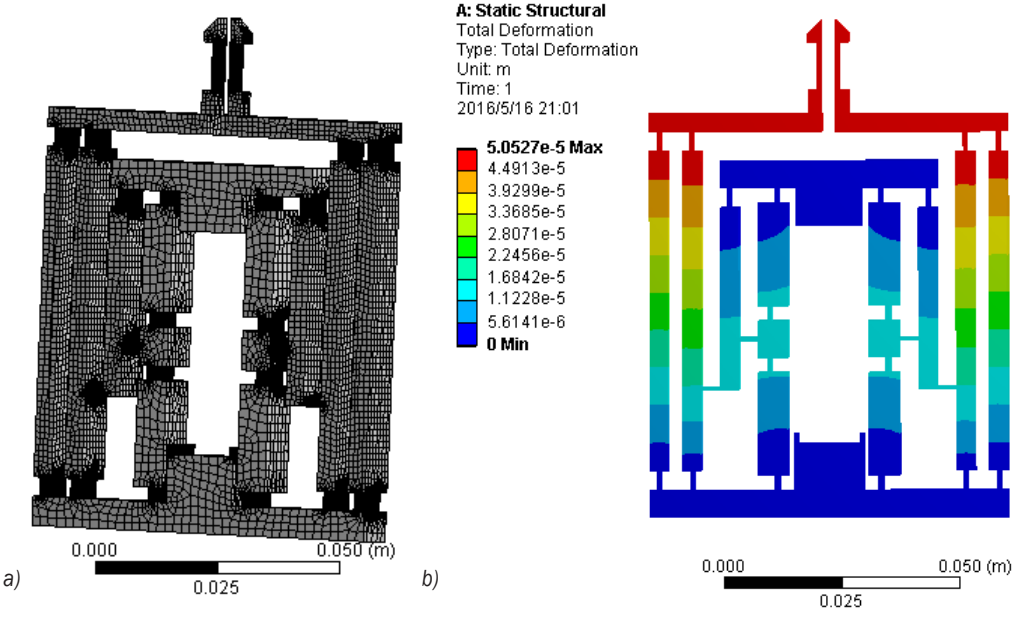

Fig. 5. *The finite element simulation diagram of micro gripper; a) mesh plots, and b) motion simulation diagram*

Table 2. *Key parameters of the micro gripper*

L [mm]	L_1 [mm]	L_2 [mm]	L_3 [mm]	L_4 [mm]	L_5 [mm]	t [mm]	b [mm]	l_4 [mm]	l_5 [mm]
1.5	11	3	22	3	4	1	10	30	40.4

l_6 [mm]	l_7 [mm]	K_{in} [N/mm]	k' [(N·mm)/rad]	k'' [N·mm)/rad]	J' [kg·mm^2]	J'' [kg·mm^2]	J''' [kg·mm^2]
19.6	72	88168	57680	21836	0.573	1.632	9.072

Table 3. *Relations output displacement and driving force of PZT of micro gripper*

ΔL_1 [μm]	1	2	3	4	5	6	7	8	9
F_{eff} [N]	49.6	99.2	148.8	198.3	247.9	297.5	347.1	396.7	446.3
ΔL_1 [μm]	10	11	12	13	14	15	16	17	18
F_{eff} [N]	495.9	545.5	595	644.6	694.2	743.9	793.5	843.1	892.7

process; its step size is easy to adjust. In comparison with the Runge-Kutta method, the variable order Adams PECE algorithm is a better method to perform the simulation analysis of the micro gripper, of which the range of allowable error is comparatively strict. Differential Eq. (15) is solved with the aid of the Matlab mathematical tool box in this paper. Because in the state equation represented by Eq. (6), the values of the inertial element, capacitive element, and resistive components are related to micro gripper parameters, the parameters of the micro gripper will be introduced before solving the state equation. The material of the micro gripper is TC4, the basic parameters of which are shown in Table 1. The key parameters of the micro gripper are shown in Table 2.

Table 1. *Relevant parameter of material*

E (elasticity modulus) [GPa]	μ (Poisson's ratio)	ρ (density) [kg/cm^3]	σ_s (yield strength) [MPa]
206	0.28	7850	1176

The PZT used here is 40VS15, which is made in China; its biggest driving force is 900 N, the maximum displacement is 36 μm, the closed-loop resolution is 1.2 nm, and stiffness is 15 N/μm. According to the stiffness characteristics of PZT, the relations between output force and output displacement of PZT under variable external loads can be obtained, shown in Table 3.

ΔL_1 is the output displacement of the PZT under variable load; F_{eff} is the output force of the PZT after overcoming the external loads.

The simulation curves of displacement of component 1 and angle displacement of flexible plate spring 21 within the scope of the biggest driving force are firstly obtained, the displacement simulation curves of component 1 are shown in Fig. 6.

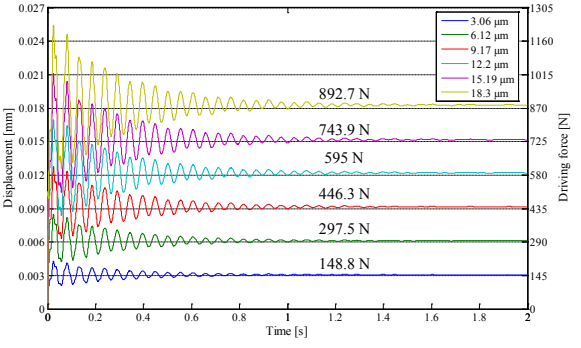

Fig. 6. *Displacement simulation curves of component 1*

The displacement simulation curves of component 1 under the force of 892.7 N, 743.9 N, 595 N, 446.3 N, 297.5 N and 148.8 N are shown in Fig. 6, and the final simulation displacement values are 18.3 μm, 15.15 μm, 12.2 μm, 9.15 μm, 6.11 μm and 3.06 μm. Consequently, the fast response is crucial in microstructure **[24]** and **[25]**. It takes about 1.2 s for a steady response of component 1.

In the same way, the angle displacement simulation curves of flexible plate spring 21 under the same input force can be obtained. Taking input force 148.8 N and 892.7 N as examples, the results are shown in Fig. 7.

The final angular simulation displacement values under 148.8 N and 892.7 N are 2.994×10^{-4} rad, and 1.786×10^{-3} rad according to Fig. 7, The response time of the angular displacement of flexible plate spring 21 is about 3 s. The length of the rod in parallel guides mechanism is 72 mm, so the displacements of the gripping jaw can be approximately calculated to 21.53

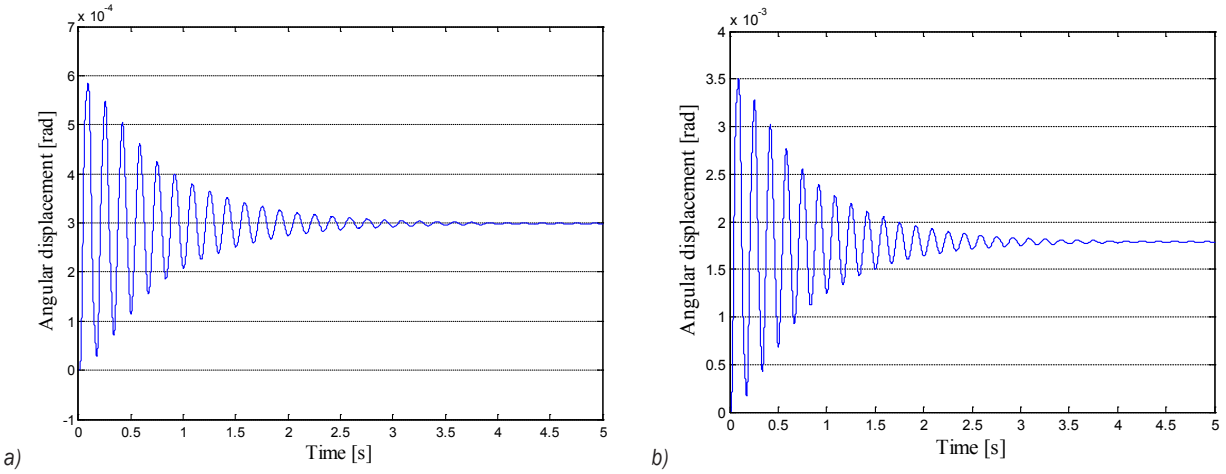

a) b)

Fig. 7. *Angular displacement simulation curves of flexible plate spring; under a) 148.8 N, and b) 892.7 N*

μm and 128.81 μm. The angular displacement of the flexible spring plate 21 under input force ranges from 49.6 N to 829.7 N can be calculated with Simulink, and the output displacement of the micro gripper can be obtained.

5.3 Experiments

In order to verify the validity of the established bond graph model of the micro gripper, the displacement of the gripper arm (component 36) under different driving forces F needs to be tested and measured within a reasonable range. The experiment principle diagram is shown in Fig. 8.

The displacement measurement test bench of the micro gripper can be set up according to Fig. 8; it is shown in Fig. 9.

During the experiment, the PZT is driven by the PZT controller and the output displacement is 1 to 18 μm, the displacement of gripper arm can be measured by the capacitance displacement sensor.

The finite element values, bond graph theoretic values and experimental values are compared; the results are obtained as shown in Fig. 10.

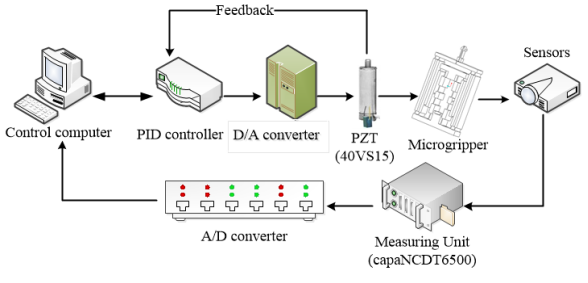

Fig. 8. *Experiment principle diagram*

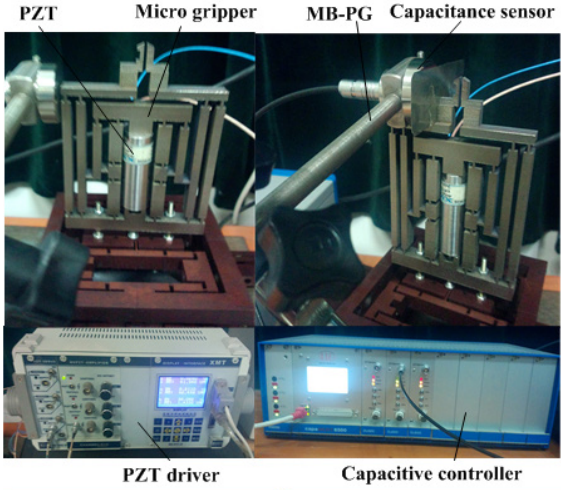

Fig. 9. *Test of micro gripper*

When the input displacement is over 13 μm, the increment of output displacement is decreasing along with the increasing of input displacement. When the input displacement is over 16 μm, the PZT is overloaded, the input displacement cannot be increased, so the finite element values, bond graph theoretic values and experimental values of gripper arm output displacement under input displacement of 1 μm to 16 μm are shown in Fig. 10a, and the maximums are 134.77 μm, 112.6 μm, and 91.52 μm, respectively.

Because of the high accuracy, the finite element simulation result is usually considered as the basis of the product performance analysis. The errors between the finite element values and the other two values are shown in Fig. 10b. It can be learned that the error between bond graph theoretic values and

finite element values is –(14.01 % to 16.42 %), the error between experimental values and finite element values is –(21.26 % to 32.09 %), where "–" means the bond graph theoretic values and experimental values are below the finite element values.

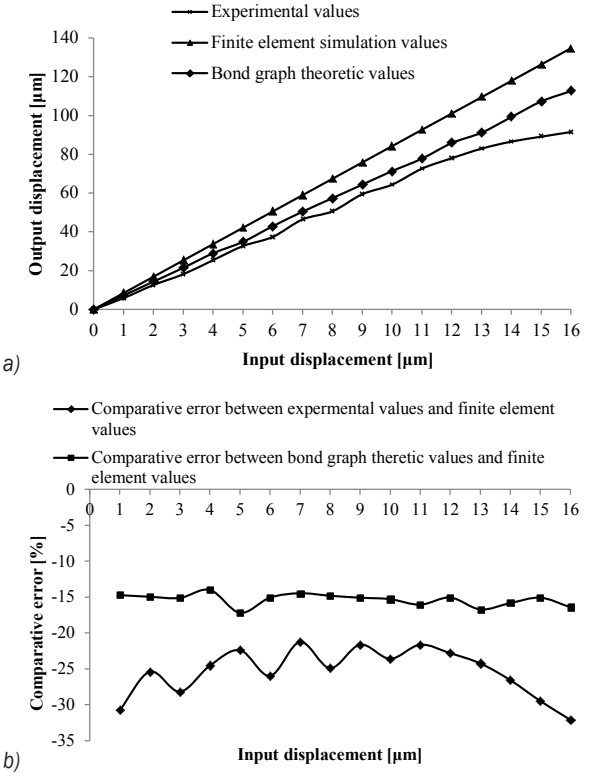

Fig. 10. *Output results of micro gripper; a) output displacement, and b) comparative error*

Table 4 can be obtained according to the analysis above.

Table 4. *Analysis result of micro gripper*

Micro gripper	Bond graph	Finite element	Experiment
One-way magnification	7.2	8.25	5.8
Max displacement [μm]	112.6	134.7	91.5
Average error [%]	–13.5	0	–23.4

The experimental values are smaller than the finite element values, and the increase becomes slow when input displacement is 13 μm, which is different from the theoretical values 18 μm, that is because the material characteristics have been changed largely by the high-temperature energy of the laser during the procedure of micro gripper. Without heat treatment, the stiffness of micro gripper is influenced by internal stress. The bond graph theoretical values and experimental values are all smaller than the finite element values, and the experimental values are closer to the bond graph theoretical values, so the correctness of the bond graph model of micro gripper and the feasibility of using the band graph method to analyse the fully flexured micro gripper are verified.

6 CONCLUSIONS

(1) A three stage amplifying micro gripper has been designed, of which a PRB model has also been set up. The micro gripper is processed based on laser rapid prototyping technology, the stiffness of BATM has been analysed, and the input stiffness of the micro gripper has been derived.

(2) The bond graph model of the micro gripper has been set up, the characteristic equations and state equations of the micro gripper are derived. The input/output displacement simulation curves of the micro gripper and angular displacement simulation curves of the flexible hinge are obtained via Matlab simulation, according to the state equations.

(3) The FEA for the micro gripper is conducted, and the experiments to verify it have been done. Matlab simulation values, FEA values, and experimental values are compared, the Matlab simulation values and FEA values are essentially the same. The error between Matlab simulation values and FEA values is small, which verifies the correctness and feasibility of the established bond graph model of the micro gripper; therefore, the bond graph method provides a new method of analysing the state changes of a fully flexible mechanism and its individual internal components.

In order to make the micro gripper more practical, there still are some tasks for future study:

(1) The research of clamping force and the relevant text need to be done;

(2) The bond graph method used in this paper still need further study for other compliant mechanisms.

7 ACKNOWLEDGEMENTS

This work is supported by the National Natural Science Foundation of China (51275537), the Independent Research Fund of State Key Laboratory of Mechanical Transmission (NO. SKLMT-ZZKT-2012 MS 05), the Open Foundation of Shang Hai Key Laboratory of Spacecraft Mechanism (SM2014D201).

8 REFERENCES

[1] Russell, R.A. (1993). Development of a robotic manipulator for micro-assembly operations. *Proceedings of the IEEE/RSJ International Conference on Intelligent Robots and Systems*, Yokohama, vol. 1, p. 471-474, **DOI:10.1109/IROS.1993.583143**.

[2] Codourey, A., Rodriguez, M., Pappas, I. (1997). A task-oriented teleoperation system for assembly in the microworld. *Proceedings of the 8th International Conference on Advanced Robotics*, Monterey, p. 235-240, **DOI:10.1109/icar.1997.620188**.

[3] Chan, H.Y., Li, W.J. (2003). A thermally actuated polymer micro robotic gripper for manipulation of biological cells. *Proceedings of the IEEE International Conference on Robotics and Automation*, vol. 1, p. 288-293, **DOI:10.1109/ROBOT.2003.1241610**.

[4] Beyeler, F., Bell, D.J., Nelson, B.J., Sun, Y., Neild, A., Oberti, S., Dual, J. (2006). Design of a micro-gripper and an ultrasonic manipulator for handling micron sized objects. *International Conference on Intelligent Robots and Systems*, p. 772-777, **DOI:10.1109/IROS.2006.282628**.

[5] Zubir, M.N.M., Shirinzadeh, B. (2009). Development of a high precision flexure-based micro gripper. *Precision Engineering*, vol. 33, no. 4, p. 362-370, **DOI:10.1016/j.precisioneng.2008.10.003**.

[6] Kyung, J.H., Ko, B.G., Ha, Y.H., Chung, G.J. (2008). Design of a micro gripper for micromanipulation of microcomponents using SMA wires and flexible hinges. *Sensors and Actuators A: Physical*, vol. 141, no. 1, p. 144-150, **DOI:10.1016/j.sna.2007.07.013**.

[7] Ren, H., Gerhard, E. (1997). Design and fabrication of a current-pulse-excited bistable magnetic microactuator. *Sensors and Actuators A: Physical*, vol. 58, no. 3, p. 259-264, **DOI:10.1016/S0924-4247(97)01395-2**.

[8] Watson, B., Friend, J., Yeo, L. (2009). Piezoelectric ultrasonic micro/milli-scale actuators. *Sensors and Actuators A: Physical*, vol. 152, no. 2, p. 219-233, **DOI:10.1016/j.sna.2009.04.001**.

[9] Nah, S.K., Zhong, Z.W. (2007). A micro gripper using piezoelectric actuation for micro-object manipulation. *Sensors and Actuators A: Physical*, vol. 133, no. 1, p. 218-224, **DOI:10.1016/j.sna.2006.03.014**.

[10] Zubir, M.N.M., Shirinzadeh, B., Tian, Y. (2009). Development of a novel flexure-based micro gripper for high precision micro-object manipulation. *Sensors and Actuators A: Physical*, vol. 150, no. 2, p. 257-266, **DOI:10.1016/j.sna.2009.01.016**.

[11] Ramadan, A.A., Takubo, T., Mae, Y., Oohara, K., Arai, T. (2009). Developmental process of a chopstick-like hybrid-structure two-fingered micromanipulator hand for 3-d manipulation of microscopic objects. *IEEE Transactions on Industrial Electronics*, vol. 56, no. 4, p. 1121-1134, **DOI:10.1109/TIE.2008.2008753**.

[12] Xiao, S.L., Li, Y.M., Zhao, X.H. (2011). Design and analysis of a novel micro-gripper with completely parallel movement of gripping arms. *6th IEEE Conference on Industrial Electronics and Applications*, p. 2127-2132, **DOI:10.1109/ICIEA.2011.5975943**.

[13] Yu, B.Q., Lei, Z., Weng, H.S. (2011). Optimal design of micro flexible gripper. *International Conference on Electric Information and Control Engineering*, p. 5154-5157, **DOI:10.1109/ICEICE.2011.5776813**.

[14] Li, Y., Huang, J., Huang, G., Wang, W., Chen, J., Zeng, Z. (2014). Comparison of radial forging between the two-and three-split dies of a thin-walled copper tube during tube sinking. *Materials & Design*, vol. 56, p. 822-832, **DOI:10.1016/j.matdes.2013.11.079**.

[15] Jain, R.K., Majumder, S., Ghosh, B., Saha, S. (2015). Design and manufacturing of mobile micro manipulation system with a compliant piezoelectric actuator based micro gripper. *Journal of Manufacturing Systems*, vol. 35, p. 76-91, **DOI:10.1016/j.jmsy.2014.12.001**.

[16] Ford, S., Macias, G., Lumia, R. (2015) Single active finger IPMC micro gripper. *Smart Materials and Structures*, vol. 24, no. 2, **DOI:10.1088/0964-1726/24/2/025015**.

[17] Hao, Y., Yuan, W., Zhang, H., Kang, H., Chang, H. (2016). A rotary micro gripper with locking function via a ratchet mechanism. *Journal of Micromechanics and Microengineering*, vol. 26, no. 1, **DOI:10.1088/0960-1317/26/1/015008**.

[18] Jain, R.K., Majumder, S., Ghosh, B. (2015). Design and analysis of piezoelectric actuator for micro gripper. *International Journal of Mechanics and Materials in Design*, vol. 11, no. 3, p. 253-276, **DOI:10.1007/s10999-014-9264-z**.

[19] Wang, F., Liang, C., Tian, Y., Zhao, X. (2015). Design of a piezoelectric-actuated micro gripper with a three-stage flexure-based amplification. *IEEE/ASME Transactions on Mechatronics*, vol. 20, no. 5, p. 2205-2213, **DOI:10.1109/TMECH.2014.2368789**.

[20] Paynter, H. (1992). An epistemic prehistory of Bond Graphs. in Breedveld, P.C., G. Dauphin-Tanguy, G. (eds.). *Bond Graphs for Engineers*. Elsevier, Amsterdam, p. 3-17.

[21] Gawthrop, P.J., Bevan, G.P. (2007). Bond-graph modeling. *IEEE Control Systems*, vol. 27, no. 2, p. 22-45, **DOI:10.1109/MCS.2007.338279**.

[22] Yildiz, I., Omurlu, V.E. (2011). Reduced order dynamics and stability of a parallel manipulator through bond-graph technique. *XXIII International Symposium on Information, Communication and Automation Technologies*, **DOI:10.1109/ICAT.2011.6102084**.

[23] Lobontiu, N., Garcia, E. (2003). Analytical model of displacement amplification and stiffness optimization for a class of flexure-based compliant mechanisms. *Computers & Structures*, vol. 81, no. 32, p. 2797-2809, **DOI:10.1016/j.compstruc.2003.07.003**.

[24] Kivi, A.R., Azizi, S. (2015). On the dynamics of a micro-gripper subjected to electrostatic and piezoelectric excitations. *International Journal of Non-Linear Mechanics*, vol. 77, p. 183-192, **DOI:10.1016/j.ijnonlinmec.2015.07.012**.

[25] Alogla, A.F., Amalou, F., Balmer, C., Scanlan, P., Shu, W., Reuben, R.L. (2015). Micro-tweezers: Design, fabrication, simulation and testing of a pneumatically actuated micro-gripper for micromanipulation and microtactile sensing. *Sensors and Actuators A: Physical*, vol. 236, p. 394-404, **DOI:10.1016/j.sna.2015.06.032**.

Strojniški vestnik - Journal of Mechanical Engineering 62(2016)9, 503-510

DOI:10.5545/sv-jme.2016.3459 Original Scientific Paper
Received for review: 2016-01-28
Received revised form: 2016-03-23
Accepted for publication: 2016-04-25

Optimization of the Brake Factor for an S-Cam Foundation Brake using RSM

Irfan Sayim – Dan Zhang
University of Ontario, Institute of Technology, Department of Automotive, Mechanical and Manufacturing, Canada

The brake factor (BF) scales the vehicle's braking force; therefore, the vehicle brake performance variation due to the foundation brake can be attributed to the BF variation. In this work, the BF reduction is considered in the design stage of an S-Cam foundation brake within dimensional properties in order to have stable, predictable and improved vehicle brake performance. First, brake lining wear types were defined and then actuation cam-roller position effects were formulated. Dimensional parameters were varied within certain design-possible ranges to quantify BF variation theoretically. The response surface method (RSM) was used to identify the BF-reduced combination of dimensions within theoretical results. In the meantime, a new testing procedure was introduced and then a new testbed was designed and built to validate relative improvement of BF experimentally without thermal effects on friction. It was investigated that a substantial improvement (22.93 %) on BF could be obtained if appropriate dimensions were selected in the design stage.
Keywords: brake factor, lining wear, S-Cam foundation brake, response surface method

Highlights
- *Brake factor (BF) optimization was carried out to improve the brake performance.*
- *A cost–effective testbed was built to measure BF in a temperature-free manner.*
- *Cam-roller position effects and lining wear types were formulated in detail.*
- *Response surface method (RSM) was used in the resizing process of dimensional design quantities.*

0 INTRODUCTION

The brake system is usually considered to be a safety part of the vehicle system and plays important operational roles. Therefore, many countries have recently introduced regulations and operational requirements for brake systems **[1]** and **[2]**. Regulations define a controllable, stable, predictable, and repeatable brake system performance for every road, load, weather condition, or partial failure. All these expectations can be met if the brake performance remains stable during its operation.

The components of a brake subsystem, such as valves and actuators, are well-controlled, and they do not significantly contribute to the variations in performance. They mostly respond to driver inputs as prescribed in their specifications-outputs. However, the performance variation of foundation brake generally depends on previously unpredictable physical conditions, such as load, road, and weather conditions. In a brake system, these conditions can arise as heat and wet affect the entire brake system through variations in friction. Electronic subsystems may partially reduce such performance variations of brakes by preventing wheel locks or accommodating vertical load related force distribution by controlling line air pressure. However, such systems do not guarantee a fully stable brake operation. Therefore, in this study, the performance variation issue for foundation brake is examined with regard to variation in the brake factor (BF).

The overall brake performance due to drum type foundation brake can be attributed to two criteria: 1) dimensional design parameters of foundation brake, and 2) friction between drum and lining **[3]**. The relation between both factors is formulized as brake factor (BF) **[4]**. Addressing issues related to BF variation is critical for quantifying performance variation in the overall vehicle brake system. Therefore, the foundation brake performance must be ensured before overall brake system performance is addressed **[5]** to **[7]**.

In general, there are two types of air-actuated foundation brakes; disc and drum. For disc type, the BF exhibits a linear relation with friction coefficient however for drum type the BF generally grows exponentially **[4]**. Since disc BF does not involve any dimensional parameters, it will not be considered in analysis here.

In past decade, a tendency showed that the drum type foundation brakes were replaced by disc brakes however, recently, a skeptical approach exists for there has been increased scepticism towards using disc brakes in the heavy commercial vehicle market. Drum type brakes (S-cam, Wedge, etc.) are still greatly preferred by truck, bus, and axle manufacturers **[8]**. A common belief among vehicle makers is that the S-Cam type foundation brake has great potential if its

*Corr. Author's Address: University of Ontario Institute of Technology, Department of Automotive, Mechanical and Manufacturing Engineering, L1H 7K4 Oshawa, ON, Canada, irfan.sayim@uoit.ca

performance is improved as a result of its reduced BF. Lessons learned from the experience that brake caused vehicle pull and vibration can also be attributed to high BF variation that usually occurs in drum-type foundation brakes [9]. In contrast, such problems are relatively small for disk type foundation brakes as a result of their low BF. In this context, the main competitor for disc brakes among drum types is the S-Cam brake in terms of BF quantity. Therefore, improving S-Cam foundation brakes, with comparable improved performance to disc brakes, may become an advantage for extensively using it on the market in the future.

In this study, the BF was optimized in the design level for an S-Cam foundation brake with the best combination of dimensional parameters. The response surface method (RSM) was used to identify the best selection option of dimensions within given ranges. Afterward, two samples were tested to validate the relative improvement. One sample was tested with nominal dimensions as assembled on the vehicles on the market. Another new sample was built based on the modified dimensions after RSM analysis. In the meantime, a new testbed was built to perform experimental measurements of BF without any thermal effects on friction. Whether a substantial reduction on BF could be obtained if appropriate dimensions were selected in the design stage was investigated.

1 S-CAM FOUNDATION BRAKE

An S-Cam foundation brake consists of a leading and a trailing shoe (Fig. 1). Both shoes are pivoted to on a foundation that is fixed on the vehicle's axle. Shoes rotate around their pivots at one end while they are mechanically actuated by an S-profiled cam, called S-Cam, at another end. The rotation of S-Cam for actuation is executed by a slack adjuster that is pushed by an air actuator from its tip.

Compressed air in the brake chamber generates a mechanical force that is transmitted to the brake shoes through the shoe roller and the S-Cam. The travel of the roller increases due to the wear of the brake linings and also due to the heat-related expansion of the brake drum as a consequence of braking operation [11] and [12]. Automatic slack adjusters, usually clearance-sensing, are used to compensate for this increase in roller travel because the force output from the brake chamber to the brake shoes decreases rapidly when the chamber stroke exceeds a certain limit. The mechanical subsystem of the schematic S-Cam air foundation brake system is illustrated in Fig 1. Depending on the rotation direction of the drum and shoes, the left side (C_L) is a leading (i.e. drum and shoe rotate at same direction) and the right side (C_T) is a trailing shoe (i.e. drum and shoe rotate at opposite direction) in Fig 1.

2 THE BRAKE FACTOR

The BF can be expressed as the ratio of drum-lining friction drag force and the shoe actuation force:

$$C^* = \frac{\sum F_{drum\_drag}}{\sum F_{shoe\_actuation}}, \quad (1)$$

where, $\sum F_{drum\_drag}$ is the summation of drum drag force and $\sum F_{shoe_actuation}$is the summation of total shoe actuation force. In order to compute the total BF (Eq. (1)), first, each shoe's BF can be computed separately as follows [10].

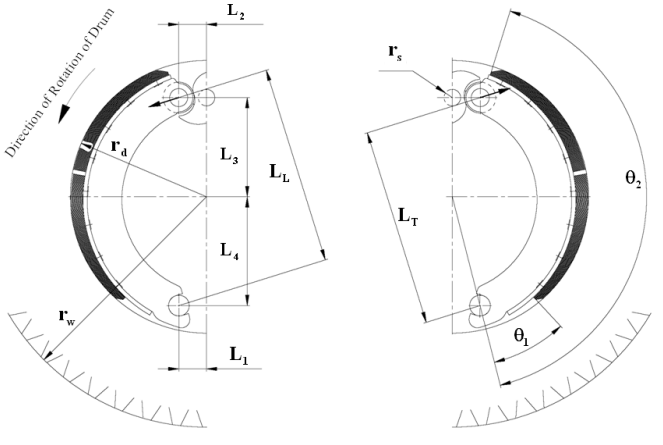

Fig. 1. *S-Cam foundation brake (from [10])*

$$C_L = \frac{4\mu L_L\left(\cos\theta_1 - \cos\theta_2\right)}{\left(-a\sin 2\theta_2 + 2a\theta_2 + a\sin 2\theta_2 - 2a\theta_1 + 4\mu r_d\cos 2\theta_2 - \mu a\cos 2\theta_2 - 4\mu r_d\cos 2\theta_1 + \mu a\cos 2\theta_1\right)}, \quad (2)$$

$$C_T = \frac{4\mu L_T\left(\cos\theta_2 - \cos\theta_1\right)}{\left(a\sin 2\theta_2 - 2a\theta_2 - a\sin 2\theta_1 + 2a\theta_1 - 4\mu r_d\cos 2\theta_2 - \mu a\cos 2\theta_2 - 4\mu r_d\cos 2\theta_1 + \mu a\cos 2\theta_1\right)}. \quad (3)$$

Here $a = \left(L_1^2 + L_4^2\right)^{1/2}$ and μ is the friction coefficient. L_L and L_T are the brake shoe's actuation lever arm lengths for leading and trailing shoes respectively and they can be calculated as:

$$\begin{bmatrix} L_L \\ L_T \end{bmatrix} = \begin{bmatrix} \cos\varphi & -\sin\varphi \\ \sin\varphi & \cos\varphi \end{bmatrix}\begin{bmatrix} L_2 + L_3 \\ L_1 \end{bmatrix} + \begin{bmatrix} r_s \\ r_s \end{bmatrix}, \quad (4)$$

where, $\varphi = \arcsin\left(b_1/L_4\right) + \arcsin\left(r_s/b_2\right)$. In this equation, $b_1 = R - \left(R^2 - (L_4 - L_i)^2\right)^{1/2}$ and $b_2 = \left(b_1^2 + L_4^2\right)^{1/2}$ with $R = \left(\left(L_i + L_1\right)^2 + \left(L_2 + L_3\right)^2\right)^{1/2}$. r_s is the S-Cam evolving (i.e. S-Cam base) radius. In analysis, L_2 is varied between L_i (i.e. before lining wear - full lining thickness) and L_f (i.e. after lining wear - lowest lining thickness) depending the rotation position of cam ($L_i \leq L_2 \leq L_f$). Sub-index L and T represent leading and trailing shoes respectively. Each shoe's BF versus friction coefficient is plotted in Fig. 2.

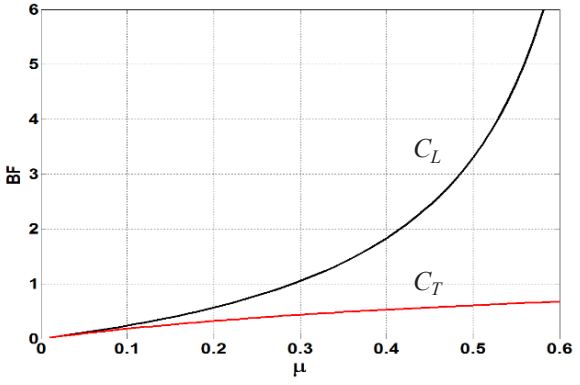

Fig. 2. *BF for leading and trailing shoes*

3 TYPES OF LINING WEAR

In calculation of BF, the nominal values data in Table 1 were used [10]. Fig. 2 shows that the BF grows exponentially for the leading shoe (C_L) as the friction coefficient increases. This occurrence is called "self-energized", and it can only be seen in type foundation brakes [13]. Brake lining wear can be categorized into two types, as follows:

Type A: Linear wear (LW): in this case, the leading and trailing shoes have no floating mechanism of actuation (i.e. actuation load transfer is prevented between both shoes). This case implies an unequal shoes actuation force or an equal lining wear. S-Cam foundation brake is a typical example.

Type B: Differential wear (DW): In this case, leading and trailing shoes have a floating mechanism of actuation (i.e. actuation load transfer is permitted between both shoes). This case implies an equal actuation force or an unequal lining wear. A simplex wedge foundation brake is a typical example. Conditions for shoe actuation force, contact pressure between drum and shoes, and resulting brake torque are summarized [10] in Table 2.

Table 1. *Nominal values (from [10])*

Variable	Quantity
L_1	40 mm
$L_i \leq L_2 \leq L_f$	$40.3 \leq L_2 \leq 72$ mm
L_3	143.15 mm
L_4	157 mm
r_s	12 mm
r_d	196.85 mm (ϕ 393.7 mm)
θ_1	28°
θ_2	145°

Table 2. *Conditions for lining wear types (from [10])*

Type	Drum/ Lining Pressure	Torque	Shoes Actuating Force	Total BF
A	$P_L = P_T$	$T_L = T_T$	$F_L < F_T$	$C^*_{LW} = 2\dfrac{(C_L C_T)}{(C_L + C_T)}$
B	$P_L < P_T$	$T_L < T_T$	$F_L = F_T$	$C^*_{DW} = C_L + C_T$

In Fig. 3, contact pressure profiles between drum and lining material are shown schematically for LW torque generated via lining and drum friction forces, F_L and F_T represent actuation forces applied to the shoes roller tips and DW. In Fig 3a, load transfer is permitted between the shoes, and equilibrium condition occurs through balanced contact pressure [10]. In Fig. 3b, load transfer is prevented via the aid of the S-Cam shaft and bushing. In this case, the pressure accumulates at trailing shoe, and the force

balance occurs through wear on the lining between two shoes [10].

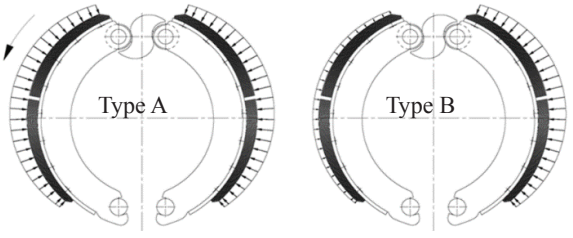

Fig. 3. *Lining-drum contact pressure profiles (from [10])*

Equilibrium Condition. In S-Cam foundation brakes, a mechanically rotating cam actuates both shoes simultaneously. The function of the S-Cam is not only actuating shoes but also preventing actuation load transfer between leading and trailing shoes during brake application. The advantage of the preventing of load transfer between shoes is (occurring in equilibrium through self-balanced lining wear condition (LW)) to have a low BF and an equally lasting lining life (Fig 4, BF for even wear rate). In reality, however, the BF can exceed uneven wear rate due to heat related shoes-drum expansions or deformations (Fig 4, BF for uneven wear rate).

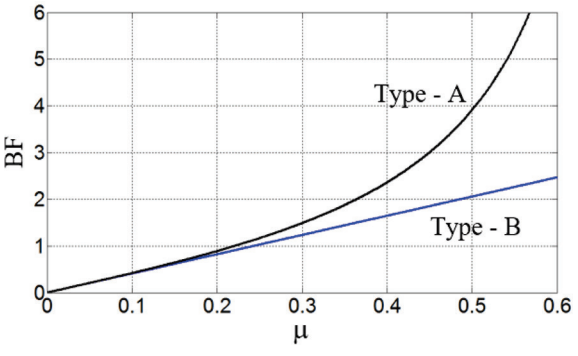

Fig. 4. *Total BF for type A and type B*

4 BRAKE PERFORMANCE VARIATION

The foundation brake performance variation is quantified due to: 1) shoe dimensions, and 2) actuated cam-roller position. The shoes' dimensions are generally specified in the initial stage of design. In contrast, the roller position (L_2) is a quantity that changes during brake application. It depends on the clearance between lining and drum that could be changed due to wear- or heat-related expansions. Therefore, these two sources of variation were computed theoretically within design-potential dimensional ranges (Table 3) to investigate their potential impacts on the complete brake system design. In the analysis, Type A and B were evaluated separately and shown in Figs. 5 and 6, respectively. In the computation, each variable was assumed to be usable within the predefined design-potential dimensional range and varied in Eqs. (2) and (3) for a fixed value of friction. All calculations were repeated for each evenly spaced discrete value of the friction coefficient (i.e. increments of 0.05 in friction coefficient). This approach was used to quantify the total impact of variables on the BF model in terms of maximum "increase" or "decrease". Therefore, the results were sorted between maximum and minimum bounds and then plotted in Figs. 5. and 6. Continuous curves represent the bounds of maximum increase and decrease. Vertical data points represent total BF variation due to incremented values of all six parameters within given ranges. The direction of variation for each parameter was also ranked as either "increase" or "decrease" and summarized in Table 4.

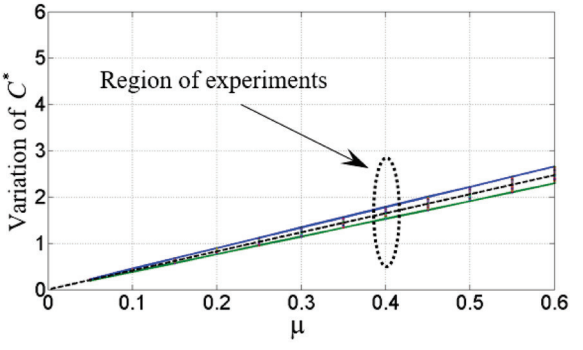

Fig 5. *BF Variation for type A*

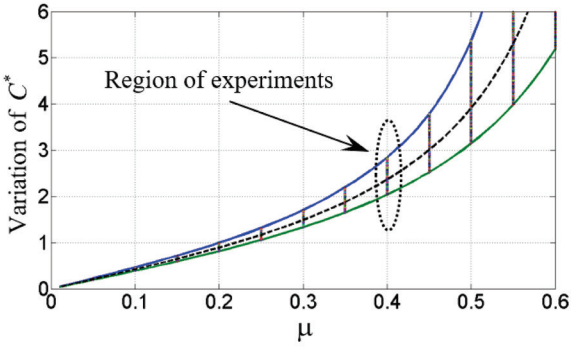

Fig 6. *BF Variation for type B*

Designing a foundation brake with improper dimensions may produce unexpected high BF that may cause a high variation in brake force when friction changes slightly. The changes in friction are unforeseeable; however, proper dimensions can be

well evaluated in the design stage of the foundation brake. In this work, the aim was set to lower the BF as much as possible within specified design-potential dimensional ranges during the design process. Therefore, the cam-roller position and shoe dimensions were carefully selected in the analysis to theoretically compute the potential of reduction on the BF. For example, in Fig. 6, a total variation of 31.92 % was observed relative to nominal value (dashed line) of BF at a friction of μ=0.4. The 19.73 % of this variation was above the nominal value; therefore, it was treated as irrelevant to analysis because the target was set to obtain a lower BF. A value of 12.19 % was below the nominal value which indicated the availability of improvement on BF. That is our primary focus of intention. Similarly, in Fig 5, a total variation of 15.37 % was observed at the friction of μ=0.4. The 8.08 % of total variation was above and 7.29 % was below the nominal.

5 THE RSM FOR THE BF MINIMIZATION

The RSM is a practical way to investigate relations between changes on the input variables and responses on the output variables in complex data systems. A wide variety of RSM engineering applications can be found in literature [14] to [16] such as aerospace, tribology, manufacturing, etc. In this analysis, the RSM is performed to minimize BF by using the values in Table 3 and at the friction coefficient of μ=0.4. Full quadratic surface fit is applied in the RSM analysis. In Fig. 7, nominal values (Table 1) were set as targeted in RMS analysis.

In Fig. 8, the RSM is run for minimizing BF with the best option of dimensional input variables. The type of lining wear (LW and DW) was not known precisely; therefore, RSM analysis was performed on both cases simultaneously in order to the obtain changes of same variables to the response of both

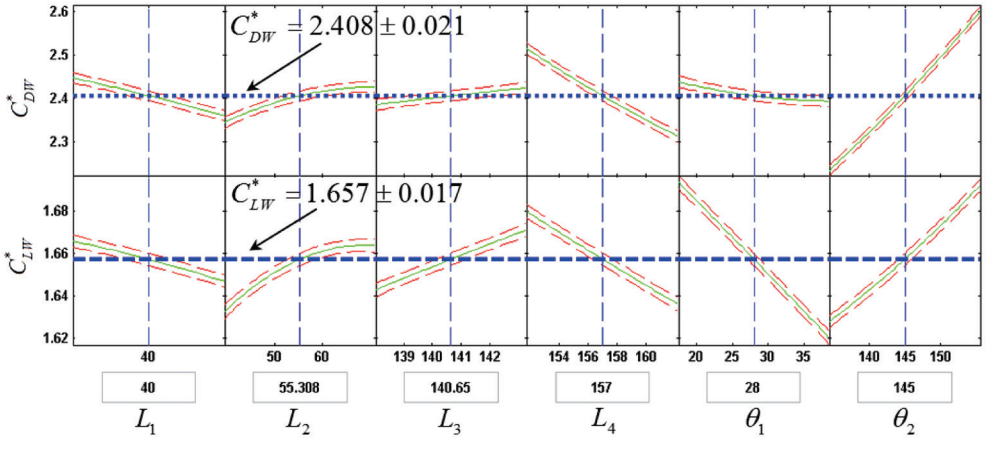

Fig. 7. *RSM results based nominal target value*

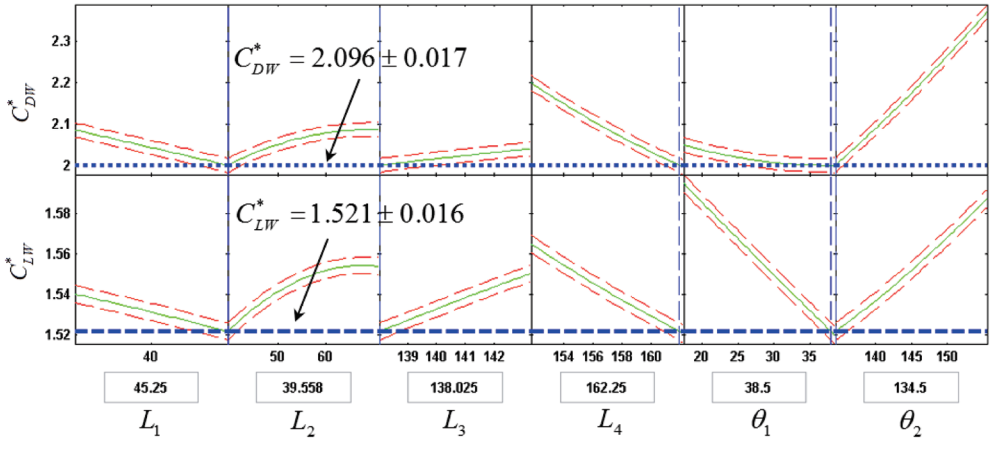

Fig. 8. *RSM results based nominal minimized target value*

Table 3. *Data values used in RSM*

	Design variables						Response variables	
Index	L_1 (35≈45) [mm]	L_2 (40.308≈70.308) [mm]	L_3 (138.15≈ 43.15) [mm]	L_4 (152≈162) [mm]	θ_1 (18≈38) [degree]	θ_2 (135≈155) [degree]	C^*_{LW}	C^*_{DW}
1	35	40.308	138.15	152	18	135	1.6563	2.3286
2	35	40.308	138.15	154	18	135	1.6472	2.2909
3	35	40.308	138.15	156	18	135	1.6383	2.2551
⋮	⋮	⋮	⋮	⋮	⋮	⋮	⋮	⋮
11662	45	70.308		158	38	155	1.6646	2.5679
11663	45	70.308	143.15	160	38	155	1.6565	2.5259
11664	45	70.308	143.15	162	38	155	1.6485	2.4860

output variables. Both RSM runs perfectly fit to the target (green solid lines) with a tolerance of ±0.06 (red dashed lines). Results of RSM, Figs 7. and 8, are summarized in Table 6 for easy interpretation. The effects of parameters were converted to percentage change and then their ranks are numbered from one to six, as shown in Table 4.

The most responsive variables (θ_2, L_4, and θ_1) are shown in shaded cells in Table 4. A new test sample of S-Cam foundation brake was built based on a modification of these three variables after RSM analysis ($\theta_1 = 38.5$, $L_4 = 162$ and $\theta_2 = 135$). For testing purposes, a new brake testbed was designed and then built to measure BF in a practical, effective and inexpensive way, as shown in Fig. 9. Most importantly, this testbed was also capable of measuring BF without thermal effects on friction (i.e. constant temperature or constant friction coefficient). With the modified test sample, one with nominal dimensions was also selected for testing to experimentally validate relative reduction on BF.

Table 4. *Effects of design parameters on BF*

	L_1	L_2	L_3	L_4	θ_1	θ_2
C^*_{LW}	↓	↑	↑	↓	↓	↑
% change	1.7221	1.7260	0.8989	4.2874	0.9992	7.7086
Rank	4	3	6	2	5	1
C^*_{DW}	↓	↑	↑	↓	↓	↑
% change	0.5622	0.9914	0.8885	1.3540	2.2661	1.9888
Rank	6	4	5	3	1	2

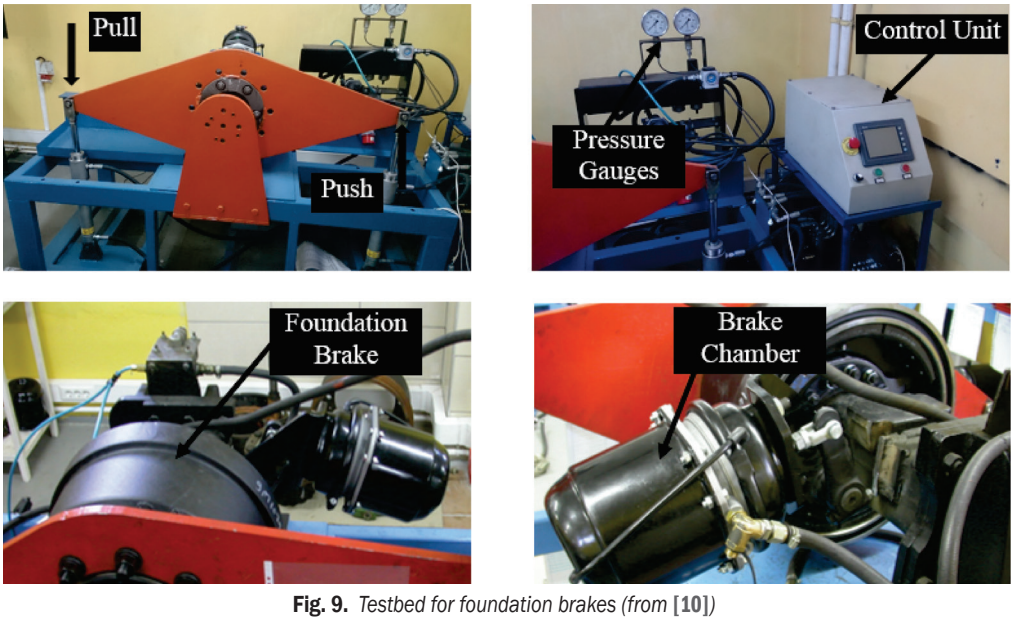

Fig. 9. *Testbed for foundation brakes (from [10])*

6 EXPERIMENTAL VALIDATION

6.1 Testbed

In the testbed, a Type-30 brake cylinder actuates both shoes. Cylinder input air pressure is controlled with a very precise pressure control and a check valve. In the meantime, the drum is forced to rotate via two hydraulic cylinders with an attached rotation flange, as shown in Fig. 9 [10]. These cylinders are also controlled by a very precise hydraulic pressure control valve. All three cylinders are plugged into a single control unit. The control unit performs the following jobs. First, it applies force to the shoe's roller through S-Cam actuation and holds the pressure of brake chamber in the stable state. This action puts the foundation and drum together in the brake state. Then, the control unit applies hydraulic pressure to the cylinders gradually to force the drum to rotate from a very low to high pressure by very small increments until the drum starts to rotate against the braked state. Sensors were installed to capture the rotation of the drum. Upon any detected small rotation in a short time (i.e. 3 mm to 5 mm relative displacement of the drum to the lining in the direction tangential to the drum's outer diameter), the sensor signals the control unit for recording all the pressures from all actuations including brake chamber and drum rotation cylinders. This pressure is an average value of measurements made by the control unit in very last short period and just before the rotation is captured. Finally, the measured force of rotation is assumed to be friction force generated by the foundation brake. The S-cam actuation force is calculated by considering the mechanical advantages (i.e. brake cylinder membrane surface, slack adjuster angles to pushrod). The ratio of these two forces is taken as BF as described in Eq. (1).

6.2 Experimental Work

Experiments were carried out by testing two samples in the testbed under the same conditions such as identical lining material (manufacturer-defined friction coefficient is $\mu = 0.4 \pm 0.02$), and same line air pressure (8.1 bar). First, the S-Cam foundation brake sample was tested with nominal design values, as given in Table 1, about fifty experimental runs.

A mean value of BF of $\bar{C}^* = 3.467$ with a standard deviation of 0.1118 were recorded. Second, a modified sample was tested over approximately fifty additional experimental runs. A mean value of BF of $\bar{C}^* = 2.672$ with a standard deviation of 0.1418 were recorded. The average of these two tests indicated that a relatively significant improvement of 22.93 % (or 0.795 of decrease on BF) on BF was obtained. Therefore, it can be concluded that highly consistent theoretical (19.48 %) and experimental (22.93 %) results were obtained in this paper analysis and also verified experimentally.

7 CONCLUSIONS

Performance improvement of an S-Cam foundation brake has been carried out with respect to its dimensional design criteria. First, a detailed precise BF formulation is derived including cam-roller position effects. Second, the BF variation is quantified theoretically by varying all six variables within certain design-possible ranges. Then, the contribution of each parameter to BF is quantified and ranked via the use of RSM. Finally, the experimental validation was performed. In this regard, a new testbed designed to measure BF effectively without any thermal effects on friction. Based on the modification of the most responsive elements, a new foundation brake test sample was built. This sample was tested and its results were compared with the nominal sample. A significant improvement (reduction of 22.93 %) on BF was obtained. With this result, we conclude that an improved S-Cam foundation brake has been designed, tested, and validated with comparable performance to disc foundation brake.

8 ACKNOWLEDGEMENTS

The author gratefully acknowledges Huseyin Cekmer, Hasan Cekmer, Murat Mater, Sabri Akin, and Ali Soylu from Tafsan Fren A.S. (formerly Istanbul Fren San ve Tic A.S.) for supporting this research. However, the views expressed in this paper belong to the authors alone and do not necessarily represent the position of any other organization or person.

9 NOMENCLATURES

C^* Brake Factor for foundation (Both shoes) [-]
$\bar{C}^*$ Mean value of measured brake factor for foundation [-]
C^*_{LW} Brake Factor for linear wear (Type A) [-]
C^*_{DW} Brake Factor for differential wear (Type B) [-]
μ Friction coefficient for lining and drum couple [-]
C_L Brake factor for leading shoe [-]
C_T Brake factor for trailing shoe [-]
F_T Force applied on the trailing shoe roller tip through S-Cam [N]

F_L Force applied on the leading shoe roller tip through S-Cam [N]
T_T Torque developed about drum axis due to friction drag force (trailing shoe) [Nm]
T_L Torque developed about drum axis due to friction drag force (leading shoe) [Nm]
P_T Pressure between lining and drum (trailing shoe) [N/m2]
P_L Pressure between lining and drum (leading shoe) [N/m2]
r_d Radius of drum [mm]
r_s Effective radius of S-Cam [mm]
r_w Effective radius of wheel [mm]
L_1 Half-length between two shoes pivots [mm]
L_2 Length 2 [mm]
L_3 Length 3 [mm]
L_4 Length 4 [mm]
L_i Initial distance between S-cam and roller centre –Full lining thickness [mm]
L_f Final distance between S-cam and roller centre – Lowest lining thickness [mm]
θ_1 Angle from reference line to tip of lining [rad]
θ_2 Angle from reference line to end of lining [rad]

10 REFERENCES

[1] United Nations (2014). E/ECE/324 and E/ECE/TRANS/505, Uniform Provisions Concerning the Approval of Vehicles of Categories M, N and O With Regard to Braking, from: *https://www.unece.org/fileadmin/DAM/trans/main/wp29/wp29regs/updates/R013r8e.pdf*, accessed on 2016-01-20.

[2] US Department of Transportation (2009). National Highway Traffic Safety Administration, 49 CRF Part 571 – RIN 2127-AK62, Federal Motor Vehicle Safety Standards; Air Brake Systems, *from: http://www.regulations.gov/#!documentDetail;D=NHTSA-2009-0175-0006*, accessed on 2016-01-20.

[3] Mac Adam, C., Gillespie, T.D. (1998). Determining the Mechanical Sensitivities of an S-cam Brake, University of Michigan, Highway Safety Research Institute, Report Number: UMTRI-98-55, from *http://deepblue.lib.umich.edu/handle/2027.42/1265*, accessed on 2016-01-20.

[4] Limpert, R. (2011). Brakes: Design and Safety, SAE International, Warrendale, **DOI:10.4271/R-398**.

[5] Winkler, C.B. (1976). Predicting the Braking Performance of Trucks and Tractor-Trailers, University of Michigan, Highway Safety Research Institute, Report Number: UM-HSRI-76-26-2, from: *http://deepblue.lib.umich.edu/handle/2027.42/738*, accessed on 2016-01-20.

[6] Gillespie, T.D., Fancher, P.S., Johnson, L.K. (1978). An Empirical Model for the Prediction of the Torque Output of Commercial Vehicle Air Brakes, University of Michigan, Highway Safety Research Institute, Report Number: UM-HSRI-8-53, from: *http://deepblue.lib.umich.edu/handle/2027.42/594*, accessed on 2016-01-20.

[7] Day, A.J., Kim, S.Y. (1996). Noise and vibration analysis of an S-cam drum brake. *Proceedings of the Institution of Mechanical Engineers, Part D: Journal of Automobile Engineering*, vol. 210, p. 35-43, **DOI:10.1243/PIME_PROC_1996_210_242_02**.

[8] Krishnan, G. (2015). *Future of Drum Brakes*. EuroBrake 2015, Dresden.

[9] Bombek, G., Pevecm M., Vranesevic, D. (2013). Research into the possible causes of squealing brake-drums. *Journal of Vibration and Control*, vol. 20, no. 9, p. 1271-1278, **DOI:10.1177/1077546312468924**.

[10] Sayim, I. and Zhang, D. (2016). Experimental quantification of brake factor for S-Cam type foundation brake. *Measurement*, vol. 87, p. 117-125, **DOI:10.1016/j.measurement.2016.02.067**.

[11] Sonawane, D.B., Narayan, K., Ra,o V.S., Subramanian, S.C. (2011). Model-based analysis of the mechanical subsystem of an air brake system. *International Journal of Automotive Technology*, vol. 12, no. 5, p. 697-704, **DOI:10.1007/s12239-011-0081-1**.

[12] Subramanian, S.C., Darbha, S., Rajagopal, K.R., (2004). Modeling the pneumatic subsystem of an S-cam air brake system. Journal of Dynamic Systems. *Measurement*, and Control, vol. 126, no. 1, p. 36-46, **DOI:10.1115/1.1666893**.

[13] Budynas, R.G., Nisbett, J.K. (2011). *Shigley's Mechanical Engineering Design*. McGraw-Hill Book Company Inc., New York.

[14] Thakre, A.A. (2015). Prediction of erosion of polyetherimide and its composites using response surface methodology. *Journal of Tribology*, vol. 137, no. 1, art. no. 011603, **DOI:10.1115/1.4028267**.

[15] Selçuk, B. (2014). Feasibility of utilizing response surface methodology for predicting wear of steels. *Proceedings of the Institution of Mechanical Engineers, Part J: Journal of Engineering Tribology*, vol. 225, no. 5, p. 277-287, **DOI:10.1177/1350650111401534**.

[16] Alaeddini, A., Yang, K., Murat, A. (2013), ASRSM: A sequential experimental design for response surface optimization. *Quality Reliability Engineering International*, vol. 29, no. 2, p. 241-358, p. 241-258, **DOI:10.1002/qre.1306**.

Strojniški vestnik - Journal of Mechanical Engineering 62(2016)9, 511-520

DOI:10.5545/sv-jme.2016.3188 Original Scientific Paper
Received for review: 2015-11-11
Received revised form: 2016-03-30
Accepted for publication: 2016-05-16

Slip Flow of Nanofluids between Parallel Plates Heated with a Constant Heat Flux

Ayşegül Öztürk - Kamil Kahveci*
Trakya University, Turkey

This study investigates the steady fully developed laminar flow and heat transfer of nanofluids between parallel plates heated with a constant heat flux. The governing equations were solved analytically under the boundary conditions of slip velocity and temperature jump. Water was taken as the base fluid and Cu, CuO and Al_2O_3 as the nanoparticles. The results were obtained for the slip factor in the range of 0 to 0.04, for the Brinkman number in the range of –0.1 to 0.1, for three different values of the ratio of the liquid layering thickness to the particle radius (0.1, 0.2, and 0.4) and for the solid volume fraction ranging from 0 % to 8 %. The results show that the nanoparticle presence in the base fluid has a significant effect on both the velocity field and heat-transfer characteristics. The average Nusselt number increases considerably with the increase of the nanoparticle solid volume fraction. The average Nusselt number takes much higher values for high values of the ratio of the liquid layering thickness to the nanoparticle radius. The average heat transfer rate of nanofluids between parallel plates ranges from the highest to the lowest when Cu, Al_2O_3, and CuO are used as nanoparticles, respectively.

Keywords: slip flow, nanofluid, parallel plate, slip factor, Nusselt number

Highlights

- *The nanoparticle usage has a considerable effect on both the velocity field and heat transfer characteristics.*
- *Velocity takes lower values with the increase of the nanoparticle solid volume fraction.*
- *The average Nusselt number increases considerably with the increase of the nanoparticle volume fraction and ratio of the liquid layering thickness to the nanoparticle radius.*
- *The average Nusselt number from the highest to the lowest is for the nanofluids of Cu, Al_2O_3, and CuO nanoparticles.*
- *The average heat transfer rate shows a decrease with the increase of the Brinkman number.*
- *The average heat transfer rate gets higher values for the positive values of the Brinkman number and lower values for the high negative values of the Brinkman number as the slip factor increases.*

0 INTRODUCTION

Flow and heat transfer in microchannels have attracted the interest of many researchers due to several application areas such as the electronic industry, microfabrication technology, and biomedical engineering. In particular, one of the main issues of the electronic industry nowadays is the transfer of heat generated in state-of-the-art chips at a rate as high as possible [1]. Since traditional air cooling systems cannot meet the demand for an efficient cooling, novel methods are being developed and analysed [1]. Cooling of electronic equipment with liquid flow in microchannels is an effective method of heat removal, which has the advantage of high heat capacity and conductivity of the liquids and the large surface area to volume ratio of the microchannels [2] and [3].

Fluid flow and heat transfer in microscale show differences from macroscale as the surface effects become more important at micro-scale flow. The major difference between macro- and micro-scale flows is slip velocity and temperature jump on the walls. For gas micro-scale flows, flow regimes can be slip ($0.001 < Kn < 0.1$), transient ($0.1 < Kn < 10$) and free molecular flow ($Kn > 10$). In contrast, for liquid micro-scale flows, the slip flow regime is primarily observed [4]. Liquid slip flow occurs when there is little interaction between the liquid and the solid surface, which occurs when liquids are non-wetting or when air (partly) covers the channel walls [5]. Both experimental and theoretical studies on liquid slip flow are available in the literature. Lichter et al. [6] studied the mechanisms for the liquid slip along the solid surfaces and observed that slip occurs by two different mechanisms: localized defect propagation and a concurrent slip of large domains. Their results also show that well-defined transitions between these mechanisms occur. Martini et al. [7] studied the molecular mechanisms of liquid slip. Their results indicate that global slip causes an increase in the number of slipping atoms, leading to an increase in the slip length. The slip length approaches a constant value when forcing has significantly large values. Guan et al. [8] performed an experimental and theoretical analysis of the slip flow in super-hydrophobic microtubes. Their results indicate that the decrease in the slip length and slip velocity with an increase in the pressure and Reynolds number is the dominant factor

*Corr. Author's Address: Trakya University, Mechanical Engineering Department, 22180 Edirne, Turkey, kamilk@trakya.edu.tr

in the total resistance reduction in microtubes. Yu et al. [9] experimentally investigated slip flow in super-hydrophobic microtubes and concluded that the slip length shows a dependency on the Reynolds number similar to the pressure drop reduction. Lee et al. [10] investigated slip on a nanostructured surface and found that the liquid slip shows an increase with a decrease of the characteristic length, and it is more pronounced when the nonlinearity increases. Malvandi and Ganji [11] performed a theoretical study on the convective heat transfer of nanofluids in a circular microchannel under the effect of a uniform magnetic field. Their results show that the velocity gradients near the solid surface increases when the magnetic field is present. Therefore, slip velocity increases, and an increase is seen in the heat transfer rate and pressure drop. Nikkah et al. [12] investigated the slip flow of nanofluids in a microchannel with an oscillating heat flux and concluded that the Nusselt number experiences an increase when the slip coefficient has higher values. The increase in the Nusselt number has higher values for high values of the Reynolds number.

Another factor important in microscale flows is viscous dissipation. Resulting from high shear stress, viscous dissipation acts as a heat source and therefore influences temperature field severely.

There are a number of studies in the literature on liquid flow and heat transfer in microchannels. Xu et al. [13] investigated the liquid flow in microchannels and found that the viscous dissipation influences temperature, pressure, and velocity distributions significantly. Satapathy [14] studied steady-state heat transfer and fluid flow in an infinite microtube and found that at the fully-developed conditions the Nusselt number shows a decrease with an increase in the slip factor. Ngoma and Erchiqui [15] investigated liquid slip flow between two parallel plates with an imposed heat flux. The results show that the Nusselt number increases when the dimensionless slip coefficient increases. Celata et al. [16] studied forced convection heat transfer in microtubes and observed that a decrease is seen in the Nusselt number with a decrease in the diameter. Garcia-Hernando et al. [17] performed an experimental study on liquid flow in a micro-heat exchanger. The results show that the thickness and material of the plate are two important factors in micro-heat exchanger design. Peng and Peterson [18] studied convective heat transfer and fluid flow of water in microstructures and found that the Nusselt number shows a dependency on the Reynolds number, the Prandtl number, the microchannel aspect ratio, and the ratio between the hydraulic diameter and the microchannel width. They also found that geometrical configuration of microchannel has a critical effect on heat transfer. Yang et al. [19] studied the influence of interfacial electrokinetic phenomena on liquid flow and heat transfer in rectangular microchannels and concluded that flow and heat transfer are considerably affected by the presence of the electric double layer and the induced electrokinetic flow. Asthana et al. [1] investigated the segmented flow of two immiscible liquids in a microchannel experimentally and found that the Nusselt number increases up to four times in the segmented flow as compared to the pure water flow. Liu et al. [20] conducted an experimental study on liquid flow and heat transfer in a rectangular microchannel with longitudinal vortex generators. They found that the heat transfer performance improves 9 % to 21 % for laminar flow and 39 % to 90 % for turbulent flow, while the pressure drop increases 34 % to 83 % for laminar flow and 61 % to 169 % for turbulent flow. Liu et al. [21] performed a numerical study on the heat transfer performance of microchannels with different surface microstructures. The results show that the shield-shaped groove microchannel has the highest heat exchange performance.

From the literature given above, it can be concluded that heat transfer enhancement methods for liquid flow in microchannels have been investigated extensively in recent years. As is well known, one of the heat transfer enhancement methods is to use nanoparticles within a base fluid. The addition of nanoparticles to a base fluid results in an anomalous increase in the effective thermal conductivity of the fluid. There is only a limited number of studies in the literature investigating the effects of nanoparticle usage on flow and heat transfer in microchannels. Koo and Kleinstreuer [22] studied the steady laminar flow of nanofluids in microchannels. The results show that nanoparticles of high thermal conductivity and channels with high aspect ratios are advantageous. Raisi et al. [23] made a numerical investigation on the laminar forced convection of nanofluids in a microchannel and found that the average Nusselt number is considerably influenced by nanofluid solid volume fraction and slip velocity coefficient for high Reynolds numbers. Jung et al. [24] conducted an experimental investigation on the forced convective heat transfer of water-based Al_2O_3 nanofluids in microchannels. Their results show that the convective heat transfer coefficient in a laminar flow regime increases up to 32 % as compared to the pure water at a volume fraction of 1.8 % without a considerable friction loss.

The aim of this study is to perform and analytical investigation on the slip flow of nanofluids between two parallel plates heated with a constant heat flux. The results were analysed to reveal the effects of solid volume fraction and the ratio of the liquid layering thickness to the nanoparticle radius on the flow and heat transfer.

1 METHODS

The geometry and the coordinate system used to investigate the slip flow and heat transfer of nanofluids between parallel plates heated with a constant heat flux are shown in Fig. 1. The fluid flow was assumed to be steady, laminar, incompressible and fully developed with constant thermo-physical properties. The nanofluid was assumed to be a single phase fluid as the solid nanoparticles are of a very small size and are easily fluidized. In the single phase approach, fluid and solid particles are assumed to be in thermal equilibrium and move with the same velocity [25]. The coordinate system is at the centre of the microchannel. The *x*-axis was taken along the centreline of the microchannel, and the *y*-axis was taken normal to it. Under these conditions, the governing equations including the viscous dissipation take the following form:

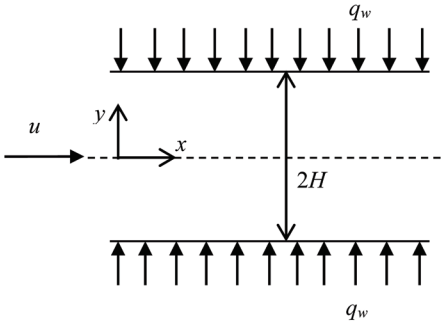

Fig. 1. *Geometry and the coordinate system*

$$\frac{d^2u}{dy^2} = \frac{1}{\mu_{nf}}\frac{dp}{dx}, \tag{1}$$

$$u\frac{\partial T}{\partial x} = \alpha_{nf}\frac{\partial^2 T}{\partial y^2} + \frac{\mu_{nf}}{\left(\rho c_p\right)_{nf}}\left(\frac{du}{dy}\right)^2, \tag{2}$$

where u is the dimensional velocity component in the x direction, p is the dimensional pressure, and T is the temperature. μ is the viscosity, ρc_p is the heat capacity and α is the thermal diffusivity.

As can be seen from Eqs. (1) and (2), flow and heat transfer has only a one-way coupling by the velocity term in the energy equation. This is because the buoyancy forces are negligible, and the thermophysical properties of the fluid were assumed to be constant [26]. The Grashof number, representing the importance of buoyancy forces, is extremely low for this flow regime and configuration as the flow is pressure driven and the Grashof number is proportional to the 3rd power of the characteristic length [$(2h)^3$]. The term $(2h)^3$ has extremely low values for a microchannel.

The viscosity of the nanofluid was estimated in this study using the following model proposed by Brinkman for a two-phase mixture [27]:

$$\mu_{nf} = \frac{\mu_f}{\left(1-\phi\right)^{2.5}}, \tag{3}$$

where ϕ is the solid volume fraction of the nanoparticles. It is useful to express that the experimental results of Xuan et al. [28] for the effective viscosity of the transformer oil-water nanofluid and of the water-copper nanofluid in the temperature range of 20 °C to 50 °C show reasonably good agreement with the Brinkman model.

The thermal diffusivity of nanofluids is defined as following:

$$\alpha_{nf} = \frac{k_{nf}}{\left(\rho c_p\right)_{nf}}, \tag{4}$$

where k is the thermal conductivity.

The reason behind the noticeable heat transfer characteristics of nanofluids is the thermal conductivity, and it is a function of the thermal conductivity of both the base fluid and nanoparticle, as well as the volume fraction, the surface area, the shape of the nanoparticles, and distribution of dispersed particles [25]. Due to the lack of a theoretical formula in the literature for the calculation of thermal conductivity of nanofluids, models for the solid-liquid suspensions with relatively large particles are generally used to estimate it. One model of this type was developed by Yu and Choi [29]. In this model, nanofluid is assumed to consist of a bulk liquid, solid nanoparticles, and solid-like nanolayers (see Fig. 2) acting as a thermal bridge between a solid nanoparticle and a bulk liquid. With the assumption of $k_{layer} = k_s$, the model for spherical nanoparticles takes the following form:

$$\frac{k_{nf}}{k_f} = \frac{k_s + 2k_f + 2\left(k_s - k_f\right)\left(1+\right)^3\varphi}{k_s + 2k_f - \left(k_s - k_f\right)\left(1+\right)^3\varphi}, \tag{5}$$

where β is the ratio of the liquid layering thickness to the nanoparticle radius. To validate their model, Yu and Choi [29] made a comparison between their model results for β = 0.1 and experimental results in the literature and found an acceptable agreement. They observed that the model is more effective for the nanofluids with nanoparticles of less than 10 nm diameter. This model was used in the present study to estimate the effective thermal conductivity of nanofluids.

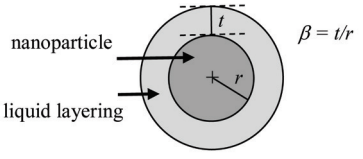

Fig. 2. *Liquid layering around a nanoparticle*

The heat capacity of nanofluids is defined as [16]:

$$\left(\rho c_p\right)_{nf} = \left(1-\phi\right)\left(\rho c_p\right)_f + \phi\left(\rho c_p\right)_s. \tag{6}$$

If the wall is not moving, the velocity-slip and the temperature-jump boundary conditions can be defined as [4]:

$$u_s = \pm\delta \left.\frac{\partial u}{\partial y}\right|_w, \quad T_s - T_w = \pm\frac{\delta}{Pr}\left.\frac{\partial T}{\partial y}\right|_w, \tag{7}$$

where u_s is the slip velocity, δ the slip factor, T_s the temperature of the base fluid at the wall, T_w the wall temperature.

1.1 Velocity Profile

The dimensionless variables can be defined as:

$$X = \frac{x}{H}, \quad Y = \frac{y}{H}, \quad U = \frac{u}{u_{m,f}},$$
$$U_s = \frac{u_s}{u_{m,f}}, \quad \Delta = \frac{\delta}{2H}, \quad P = \frac{pH}{\mu_f u_{m,f}}, \tag{8}$$

where $u_{m,f}$ is the mean velocity of the base fluid and is defined as:

$$u_{m,f} = \frac{1}{2H}\int_{-H}^{H} u dy. \tag{9}$$

The dimensionless x-momentum equation and associated boundary conditions for hydrodynamically fully developed flow can then be obtained as:

$$\frac{d^2U}{\partial Y^2} = \frac{\mu_f}{\mu_{nf}}\frac{dP}{dX}, \tag{10}$$

$$\left.\frac{dU}{dY}\right|_{Y=0} = 0 \quad at \quad Y = 0, \tag{11}$$

$$U = U_s = -2\Delta \left.\frac{dU}{dY}\right|_{Y=1} \quad at\ Y = 1. \tag{12}$$

The analytical solution of Eq. (10) subjected to the boundary conditions given in Eqs. (11) and (12) is:

$$U = \frac{3}{2}\frac{\mu_f}{\mu_{nf}}\left[\frac{1-Y^2+4\Delta}{1+6\Delta}\right]. \tag{13}$$

1.2 Temperature Distribution

The dimensionless temperature can be defined as:

$$\theta\left(Y\right) = \frac{T-T_s}{\frac{q_w H}{k_f}}. \tag{14}$$

The dimensionless energy equation can then be obtained as:

$$\frac{\partial^2\theta}{\partial Y^2} = \frac{k_f}{k_{nf}}\left[\frac{\left(\rho c_p\right)_{nf}}{\left(\rho c_p\right)_f} aU - \frac{\mu_{nf}}{\mu_f} Br\left(\frac{dU}{dY}\right)^2\right], \tag{15}$$

where $a = \dfrac{Hu_{m,f}\left(\rho c_p\right)_f}{q_w}\dfrac{dT_s}{dx}$ and Br is the modified Brinkman number defined as:

$$Br = \frac{\mu_f u_{m,f}^2}{q_w H}. \tag{16}$$

The energy equation is subjected to the following boundary conditions:

$$\left.\frac{d\theta}{dY}\right|_{Y=0} = 0 \quad at \quad Y = 0, \tag{17}$$

$$\theta = 0, \quad \left.\frac{d\theta}{dY}\right|_{Y=1} = \frac{k_f}{k_{nf}} \quad at \quad Y = 1. \tag{18}$$

The solution of Eq. (15) under the thermal boundary conditions given in Eqs. (17) and (18) is:

$$\theta\left(Y\right) = \frac{T-T_s}{\frac{q_w H}{k_f}} = \frac{k_f}{k_{nf}}\left\{\left[\frac{\mu_f}{\mu_{nf}}\frac{3Br}{\left(1+6\Delta\right)^3} + \frac{1}{1+6\Delta}\right]\times\right.$$
$$\times\left[-\frac{1}{8}Y^4 + \frac{3}{4}Y^2 + 3\Delta\left(Y^2-1\right) - \frac{5}{8}\right] -$$
$$\left. -\frac{\mu_f}{\mu_{nf}}\frac{3Br}{4\left(1+6\Delta\right)^2}\left[Y^4-1\right]\right\}. \tag{19}$$

Eq. (19) is in terms of T_s and can be transformed into an equation in terms of T_w using the following conversion formula:

$$\frac{T_s - T_w}{\frac{q_w H}{k_f}} = -2\frac{k_f}{k_{nf}}\frac{\Delta}{Pr}. \tag{20}$$

Therefore, Eq. (19) takes the following form:

$$\tilde{\theta} = \frac{T - T_w}{\frac{q_w H}{k_f}} = \frac{k_f}{k_{nf}}\left\{\left[\frac{\mu_f}{\mu_{nf}}\frac{3Br}{(1+6\Delta)^3} + \frac{1}{1+6\Delta}\right]\times \right.$$
$$\times\left[-\frac{1}{8}Y^4 + \frac{3}{4}Y^2 + 3\Delta\left(Y^2 - 1\right) - \frac{5}{8}\right] -$$
$$\left. -\frac{\mu_f}{\mu_{nf}}\frac{3Br}{4(1+6\Delta)^2}\left[Y^4 - 1\right] - 2\frac{\Delta}{Pr}\right\}. \tag{21}$$

For fully developed flows, the mean fluid temperature is preferred in defining the Nusselt number instead of the centreline temperature. The mean temperature of the fluid is defined as:

$$\tilde{\theta}_{m,nf} = \frac{T_{m,nf} - T_w}{\frac{q_w H}{k_f}} =$$
$$= \frac{k_f}{k_{nf}}\left\{-\frac{1}{35}\left[\frac{\mu_f}{\mu_{nf}}\frac{3Br}{(1+6\Delta)^4} + \frac{1}{(1+6\Delta)^2}\right]\times\right.$$
$$\times\left[420\Delta^2 + 168\Delta + 17\right] +$$
$$\left. \boxplus\frac{\mu_f}{\mu_{nf}}\frac{6Br}{35(1+6\Delta)^3}\left[21\Delta + 4\right] - 2\frac{\Delta}{Pr}\right\}. \tag{22}$$

The dimensionless mean temperature in term of the modified Brinkman number can then be obtained as:

$$\tilde{\theta}_{m,nf} = \frac{T_{m,nf} - T_w}{\frac{q_w H}{k_f}} =$$
$$= \frac{k_f}{k_{nf}}\left\{-\frac{1}{35}\left[\frac{\mu_f}{\mu_{nf}}\frac{3Br}{(1+6\Delta)^4} + \frac{1}{(1+6\Delta)^2}\right]\times\right.$$
$$\times\left[420\Delta^2 + 168\Delta + 17\right] +$$
$$\left. +\frac{\mu_f}{\mu_{nf}}\frac{6Br}{35(1+6\Delta)^3}\left[21\Delta + 4\right] - 2\frac{\Delta}{Pr}\right\}. \tag{23}$$

The convective heat transfer coefficient can be defined as:

$$h_{nf} = \frac{q_w}{T_w - T_{m,nf}}. \tag{24}$$

Therefore, the average Nusselt number takes the following form:

$$Nu = -\frac{2}{\tilde{\theta}_{m,nf}}. \tag{25}$$

After the necessary substitution, the average Nusselt number becomes:

$$Nu = -2\left\{\frac{k_f}{k_{nf}}\left\{-\frac{1}{35}\left[\frac{\mu_f}{\mu_{nf}}\frac{3Br}{(1+6\Delta)^4} + \frac{1}{(1+6\Delta)^2}\right]\times\right.\right.$$
$$\times\left[420\Delta^2 + 168\Delta + 17\right] +$$
$$\left.\left. +\frac{\mu_f}{\mu_{nf}}\frac{6Br}{35(1+6\Delta)^3}\left[21\Delta + 4\right] - 2\frac{\Delta}{Pr}\right\}\right\}^{-1}. \tag{26}$$

2 RESULTS AND DISCUSSION

Hydrodynamically and thermally fully developed slip flow of nanofluids between parallel plates heated with a constant heat flux was investigated in this study. Water was taken as the working fluid with $Pr = 6.2$ and Cu, CuO, and Al_2O_3 as the nanoparticles. The thermo-physical properties of the base fluid and nanoparticles are shown in Table 1. The results were obtained for the slip factor ranging from 0 to 0.04, for the Brinkman number ranging from –0.1 to 0.1 and for the solid volume fraction ranging from 0 % to 8 %, and for the ratio of the liquid layering thickness to the nanoparticle radius ranging from 0 to 0.4.

To validate the analysis, the results obtained for air as the heat transfer fluid were compared with the results of the studies available in the literature. The comparison shows that there is a good agreement between the results (see **[30]**).

Table 1. *Thermo-physical properties of the base fluid and nanoparticles*

Property	Water	Cu	CuO	Al_2O_3
ρ [kg/m³]	997.1	8933	6500	3970
c_p [J/(kgK)]	4179	385	535.6	765
k [W/(mK)]	0.613	400	20	40

The dimensionless axial velocity profile is shown in Fig. 3 for various values of the slip factor and solid volume fraction. As the slip factor increases, slip velocity on the walls increases and velocity in

the core region takes lower values. Higher slip is associated with the lower core velocities as expected. As it is seen in Fig. 3, velocity gets lower values with an increase in the nanoparticle solid volume fraction. As Eq. (3) suggests, an increase in the nanoparticle volume fraction causes an increase in the viscosity of the nanofluid. Therefore, viscose forces get higher values and a decrease in velocity is observed as the nanoparticle volume fraction is increased.

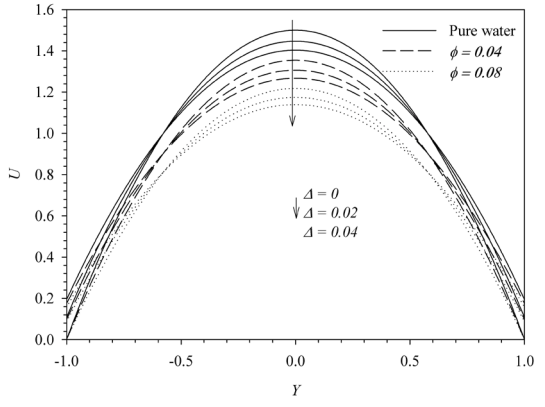

Fig. 3. *Velocity profiles for various values of the slip factor and solid volume fraction*

Variation of the average Nusselt number with the slip factor is seen in Figs. 4 to 6 for various values of the Brinkman number, solid volume fraction, and the ratio of liquid layering thickness to nanoparticle radius. The positive values of the Brinkman number mean that the fluid is being heated by the hot wall, while the negative values mean that the fluid is being cooled by the cold wall. As the slip factor increases, temperature jump at the microchannel walls increases. This has a negative effect on the heat transfer. However, an increase in the slip factor also decreases the viscous forces near the wall. This has a positive effect on the convective heat transfer from the wall to the fluid and a negative effect on the convective heat transfer from the fluid to the wall when the viscous dissipation is at significant levels. As a result of the combined effect of the velocity and temperature jumps, an increase is seen in the heat transfer for the positive values of the Brinkman number and a decrease in the high negative values of the Brinkman number. As it can be seen from Figs. 4 to 6, the effect of the slip factor on the heat transfer decreases when the Brinkman number has lower values. For the hot wall case, viscous dissipation decreases the temperature difference between the solid surface and the fluid. Therefore, the average Nusselt number takes lower values with an increase in the Brinkman

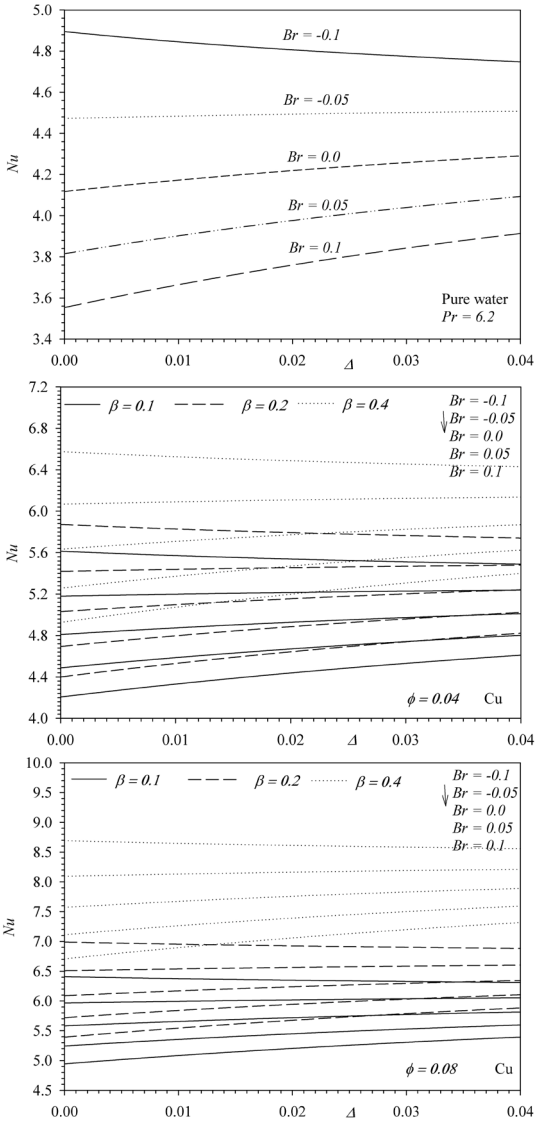

Fig. 4. *Variation of the average Nu number with the slip factor for the Cu nanofluid*

number. For the cold wall case, viscous dissipation causes an increase in the temperature difference between the solid surface and fluid. Therefore, the average Nusselt number increases with an increase in the Brinkman number in the negative direction. As seen from Figs. 4 to 6, the nanoparticle usage has a significant effect on the average heat transfer rate, and the average Nusselt number increases considerably with the increase of the nanoparticle volume fraction. As was observed before, velocity decreases with the increase of the nanoparticle volume fraction. This creates a negative effect on heat transfer. Despite this negative effect, the average Nusselt number increases

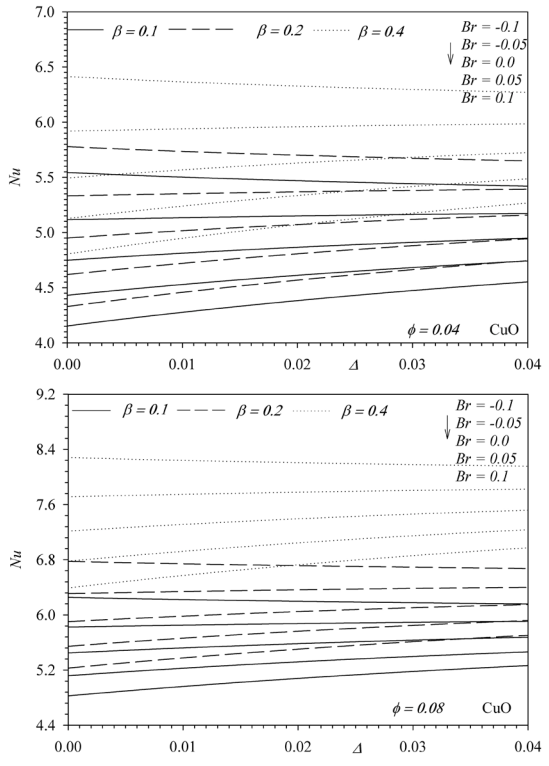

Fig. 5. *Variation of the average Nu number with the slip factor for the CuO nanofluid*

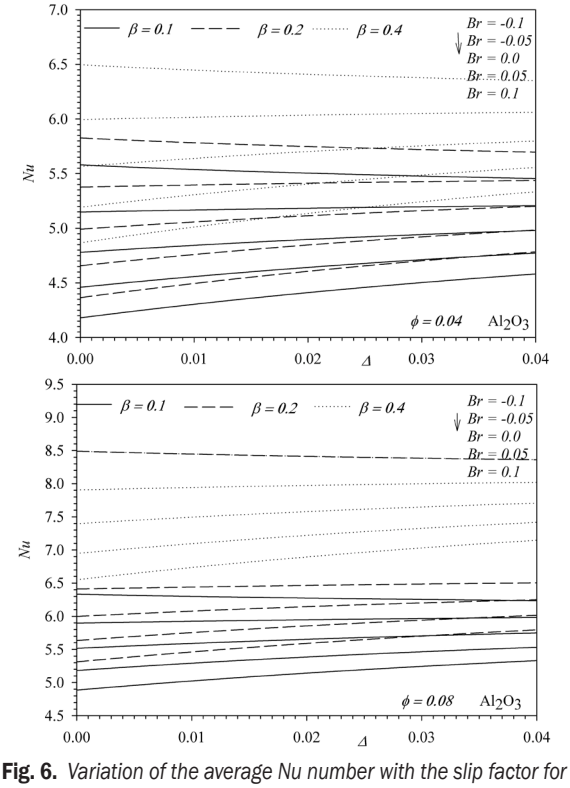

Fig. 6. *Variation of the average Nu number with the slip factor for the Al_2O_3 nanofluid*

with the increase of the nanoparticle volume fraction as the energy transport between the wall and fluid increases considerably as a result of the increase in the thermal conductivity of the fluid. The effect of the slip factor on heat transfer decreases with an increase in the nanoparticle volume fraction as the thermal diffusion has higher values. The average Nusselt number has much higher values for the higher values of the ratio of the liquid layering thickness to the nanoparticle radius, or in other words for lower values of the nanoparticle diameter. As expected, the average Nusselt number for the nanoparticles with a

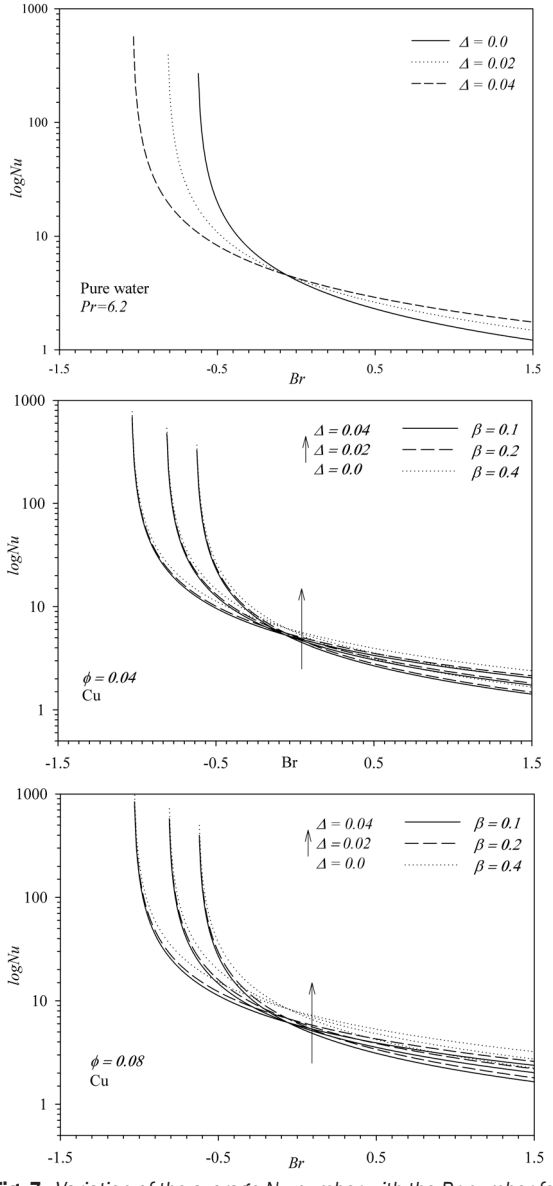

Fig. 7. *Variation of the average Nu number with the Br number for the Cu nanofluid*

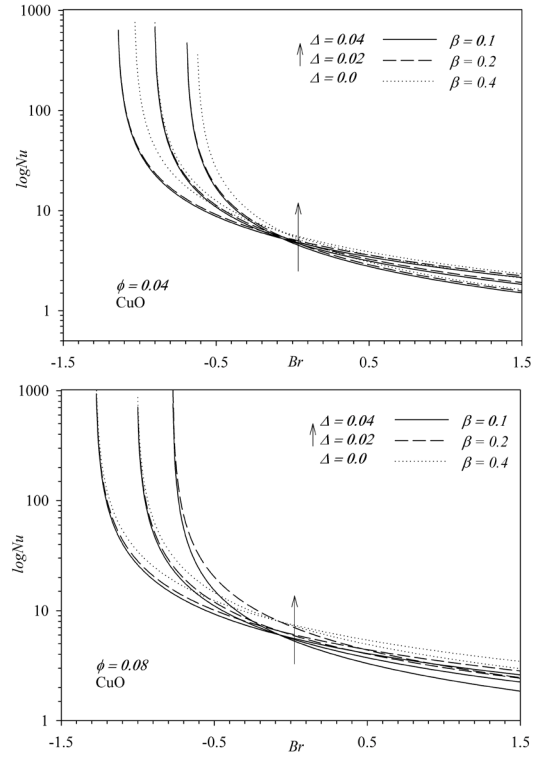

Fig. 8. *Variation of the average Nu number with the Br number for the CuO nanofluid*

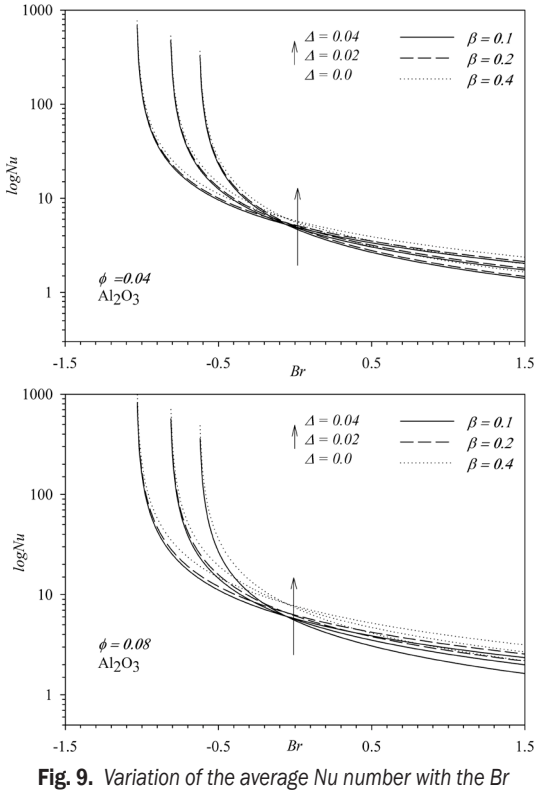

Fig. 9. *Variation of the average Nu number with the Br number for the Al_2O_3 nanofluid*

higher thermal conductivity has higher values. It is the highest for Cu nanoparticles and the lowest for CuO nanoparticles.

The variation of the average Nusselt number with the Brinkman number is seen in Figs. 7 to 9 for various values of the slip factor, solid volume fraction and ratio of the liquid layering thickness to the nanoparticle radius. As it can be observed from the figures, the average heat transfer rate shows a steep decrease first and then progressively approaches to an asymptotic value with the increase of the Brinkman number. As can also be seen from the figures, the average Nusselt number shows a similar trend for all the nanofluids considered in this study. Only a magnitude difference is seen in the average Nusselt number for different nanofluids. As stated before, this can be attributed to the more effective thermal energy transport between the wall and the nanofluid.

3 CONCLUSIONS

The slip flow of nanofluids between two parallel plates heated with a constant heat flux was investigated in this study. Water was taken as the base fluid and Cu, CuO, and Al_2O_3 as the nanoparticles. The concluding remarks are:

- The nanoparticle usage has a significant effect on both the velocity field and the heat transfer characteristics.
- The average heat transfer rate increases considerably as the nanoparticle solid volume fraction is increased.
- The average Nusselt number takes much higher values for the high values of the ratio of the liquid layering thickness to the nanoparticle radius.
- The average heat transfer rate of nanofluids ranges from the highest to the lowest, when Cu, Al_2O_3, and CuO nanoparticles are used, respectively.

4 NOMENCLATURES

Br	modified Brinkman number
c_p	specific heat at constant pressure [J/(kgK)]
h	convective heat transfer coefficient [W/(m²K)]
H	half distance between plates [m]
Kn	Knudsen number
k	thermal conductivity [W/(mK)]
Nu	Nusselt number
p	pressure [Pa]
Pr	Prandtl number
q_w	wall heat flux [W/m²]
T	temperature [K]

u velocity component in the x direction [m/s]
U dimensionless velocity
x dimensional axial coordinate [m]
X dimensionless axial coordinate
y dimensional normal coordinate [m]
Y dimensionless normal coordinate

Greek Symbols
α thermal diffusivity [m^2/s]
β ratio of the liquid layering thickness to the nanoparticle radius
δ slip factor [m]
Δ dimensionless slip factor
θ dimensionless temperature
$\tilde{\theta}$ dimensionless temperature
μ dynamic viscosity [Pas]
ρ density [kg/m^3]
ϕ solid volume fraction

Subscripts
c centreline
f base fluid
$layer$ solid-like nanolayer
m mean
nf nanofluid
s solid nanoparticles or slip
w wall

5 REFERENCES

[1] Asthana, A., Zinovik, I., Weinmueller, C., Poulikakos, D. (2011). Significant Nusselt number increase in microchannels with a segmented flow of two immiscible liquids: An experimental study. *International Journal of Heat and Mass Transfer*, vol. 54, no. 7-8, p. 1456–1464, **DOI:10.1016/j.ijheatmasstransfer.2010.11.048**.

[2] Tuckerman, D.B., Pease, R.F.W. (1981). High-performance heat sinking for VLSI. *IEEE Electron Device Letters*, vol. 2, no. 5, p. 126-129, **DOI:10.1109/EDL.1981.25367**.

[3] Upadhye, H.R., Kandlikar, S.G. (2004). Optimization of microchannel geometry for direct chip cooling using single phase heat transfer. *Proceedings of the 2nd International Conference on Microchannel and Minichannels*, p. 679-685, **DOI:10.1115/ICMM2004-2398**.

[4] Karimipour, A., Nezhad, A.H., D'orazio, A., Esfe, M.H., Safaei, M.R., Shirani, E. (2015). Simulation of copper-water nanofluid in a microchannel in slip flow regime using the lattice Boltzmann method. *European Journal of Mechanics - B/Fluids*, vol. 49, p. 89-99, **DOI:10.1016/j.euromechflu.2014.08.004**.

[5] Eijkel, J. (2007). Liquid slip in micro- and nanofluidics: recent research and its possible implications. *Lab on a Chip*, vol. 7, no. 3, p. 299-301, **DOI:10.1039/B700364C**.

[6] Lee, D.J.,Cho, K.Y., Jang, S., Song, Y.S., Youn, J.R. (2012). Liquid slip on a nanostructured surface. *Langmuir*, vol. 28, no. 28, p. 10488-10494, **DOI:10.1021/la302264t**.

[7] Martini, A., Roxin, A., Snurr, R.O., Wang, O., Lichter, S. (2008). Molecular mechanisms of liquid slip. *Journal of Fluid Mechanics*, vol. 600, p. 257-269, **DOI:10.1017/S0022112008000475**.

[8] Lichter, S., Roxin, A., Mandre, S. (2004). Mechanisms for liquid slip at solid surfaces. *Physical Review Letters*, vol. 93, no. 8, 086001, **DOI:10.1103/PhysRevLett.93.086001**.

[9] Malvandi, A., Ganji, D.D. (2014). Brownian motion and themophoresis effects on slip flow of alumina/water nanofluid inside a circular microchannel in the presence of a magnetic field. *International Journal of Thermal Sciences*, vol. 84, p. 196-206, **DOI:10.1016/j.ijthermalsci.2014.05.013**.

[10] Nikkhah, Z., Karimipour, A., Safaei, M.R., Forghani-Therani, P., Goodarzi, M., Dahari, M., Wongwises, S. (2015). Forced convective heat transfer of water/functionalized multi-walled carbon nanotube nanofluids in a microchannel with oscillating heat flux and slip boundary condition. *International Communications in Heat and Mass Transfer*, vol. 68, p. 69-77, **DOI:10.1016/j.icheatmasstransfer.2015.08.008**.

[11] Guan, N., Liu, Z., Jiang, G., Zhang, C., Ding, N. (2015). Experimental and theoretical investigations on the flow resistance reduction and slip flow in super-hydrophobic micro tubes. *Experimental Thermal and Fluid Science*, vol. 69, p. 45-57, **DOI:10.1016/j.icheatmasstransfer.2015.08.008**.

[12] Yu, Z., Liu, X., Kuang, G. (2015). Water slip flow in superhydrophobic microtubes within laminar flow region. *Chinese Journal of Chemical Engineering*, vol. 23, no. 5, p. 763-768, **DOI:10.1016/j.cjche.2014.12.010**.

[13] Xu, B., Ooi, K.T., Mavriplis, C., Zaghloul, M.E. (2002). Viscous dissipation effects for liquid flow in microchannels. *International Conference on Modeling and Simulation of Microsystems*, p. 100-103.

[14] Satapathy, A.K. (2010). Slip flow heat transfer in an infinite microtube with axial conduction. *International Journal of Thermal Sciences*, vol. 49, no. 1, p. 153-160, **DOI:10.1016/j.ijthermalsci.2009.06.012**.

[15] Ngoma, G.D., Erchiqui, F. (2007). Heat flux and slip effects on liquid flow in a microchannel. *International Journal of Thermal Sciences*, vol. 46, no. 11, p. 1076-1083, **DOI:10.1016/j.ijthermalsci.2007.02.001**.

[16] Celata, G.P., Cumo, M., Marconi, V., McPhail, S.J., Zummo, G. (2006). Microtube liquid single-phase heat transfer in laminar flow. *International Journal of Heat and Mass Transfer*, vol. 49, no. 19-20, p. 3538–3546, **DOI:10.1016/j.ijheatmasstransfer.2006.03.004**.

[17] García-Hernando, N., Acosta-Iborra, A., Ruiz-Rivas, U., Izquierdo, M. (2009). Experimental investigation of fluid flow and heat transfer in a single-phase liquid flow micro-heat exchanger. *International Journal of Heat and Mass Transfer*, vol. 52, no. 23-24, p. 5433–5446, **DOI:10.1016/j.ijheatmasstransfer.2009.06.034**.

[18] Peng, X.F., Peterson, G.P. (1996). Convective heat transfer and flow friction for water flow in microchannel structures. *International Journal of Heat and Mass Transfer*, vol. 39, no. 12, p. 2599-2608, **DOI:10.1016/0017-9310(95)00327-4**.

[19] Yang, C., Li, D., Masliyah, J.B. (1998). Modeling forced liquid convection in rectangular microchannels with electrokinetic effects. International Journal of Heat and Mass Transfer,

vol. 41, no. 24, p. 4229-4249, **DOI:10.1016/S0017-9310(98)00125-2**.

[20] Liu, C,. Teng, J-T., Chu, J.-C., Chiu, Y.-L., Huang, S., Jin, S., Dang, T., Greif, R., Pan, H.-H. (2011). Experimental investigations on liquid flow and heat transfer in rectangular microchannel with longitudinal vortex generators. *International Journal of Heat and Mass Transfer*, vol. 54, no. 13-14, p. 3069-3080, **DOI:10.1016/j.ijheatmasstransfer.2011.02.030**.

[21] Liu, Y., Cui, J., Jiang, Y.X., Li, W.Z. (2011). A numerical study on heat transfer performance of microchannels with different surface microstructures. Applied Thermal Engineering, vol. 31, no. 5, p. 921-931, **DOI:10.1016/j.applthermaleng.2010.11.015**.

[22] Koo, J., Kleinstreuer, C. (2005). Laminar nanofluid flow in microheat-sinks. *International Journal of Heat and Mass Transfer*, vol. 48, no. 13, p. 2652–2661, **DOI:10.1016/j.ijheatmasstransfer.2005.01.029**.

[23] Raisi, A., Ghasemi, B., Aminossadati, S.M. (2011). A numerical study on the forced convection of laminar nanofluid in a microchannel with both slip and no-slip conditions. *Numerical Heat Transfer, Part A: Applications: International Journal of Computation and Methodology*, vol. 59, no. 2, p. 114-129, **DOI:10.1080/10407782.2011.540964**.

[24] Jung, J.-Y., Oh, H.-S., Kwak, H.-Y. (2009). Forced convective heat transfer of nanofluids in microchannels. *International Journal of Heat and Mass Transfer*, vol. 52, no. 1-2, p. 466-472, **DOI:10.1016/j.ijheatmasstransfer.2008.03.033**.

[25] Kahveci, K. (2010). Buoyancy driven heat transfer of nanofluids in a tilted enclosure *Journal of Heat Transfer*, vol. 132, no. 6, 062501, **DOI:10.1115/1.4000744**.

[26] Aydın, O., Avcı, M. (2007). Analysis of laminar heat transfer in micro-Poiseuille flow, *International Journal of Thermal Sciences*, vol. 46, no. 1, p. 30-37, **DOI:10.1016/j.ijthermalsci.2006.04.003**.

[27] Brinkman, H.C. (1952). The viscosity of concentrated suspensions and solutions. *The Journal of Chemical Physics*, vol. 20, p. 571-581, **DOI:10.1063/1.1700493**.

[28] Xuan, Y., Li, Q., Xuan, Y., Li, Q. (1999). *Experimental research on the viscosity of nanofluid*s. Report of Nanjing University of Science and Technology, Nanjing.

[29] Yu, W., Choi, S.U.S. (2003). The role of interfacial layers in the enhanced thermal conductivity of nanofluids: a renovated Maxwell model. *Journal of Nanoparticle Research*, vol. 5, no. 1, p. 167-171, **DOI:10.1023/A:1024438603801**.

[30] Ozturk, A. (2012). MHD slip flow between parallel plates heated with a constant heat flux. *Journal of Thermal Science and Technology*, vol. 33, no. 1, p. 11-20.

Strojniški vestnik - Journal of Mechanical Engineering 62(2016)9, 521-533

DOI:10.5545/sv-jme.2016.3482 Original Scientific Paper
Received for review: 2016-02-03
Received revised form: 2016-05-06
Accepted for publication: 2016-05-09

Numerical Investigation of the Nanoparticle Volume Fraction Effect on the Flow, Heat Transfer, and Entropy Generation of the Fe_3O_4 Ferrofluid under a Non-uniform Magnetic Field

Fazel Hosseinzadeh[1] – Faramarz Sarhaddi [1,*] – Davod Mohebbi-Kalhori[2]
[1] University of Sistan and Baluchestan, Department of Mechanical Engineering, Iran
[2] University of Sistan and Baluchestan, Department of Chemical Engineering, Iran

This paper presents research on the forced flow convective heat transfer of a ferrofluid (water and Fe_3O_4) in a horizontal two-dimensional channel under the influence of a 2D non-uniform magnetic field, which is applied through a line dipole. The governing equations of this research include continuity, momentum, energy and entropy generation, which are solved with a finite volume technique. Moreover, a grid-independent test and the validation of numerical results are carried out. The effect of the Fe_3O_4 volume fraction (1 vol % to 6 vol %) on the hydro-thermal characteristics of the ferrofluid flow and entropy generation is studied. Numerical results show that the flow pattern is highly changed, because the kelvin body force overcomes the viscous force by increasing the volume fraction under applied magnetic field. Furthermore, the average wall friction factor increases linearly. The average Nusselt number ($\overline{Nu}$) increases with the increase of the Fe_3O_4 volume fraction, so that $\overline{Nu}$ increases by 51.1 % in comparison to the base fluid at 6 vol %. It is observed that the Nusselt number ratio (NUR) at 6 vol % is enhanced by 10.4 % whereas the entropy generation ratio (NSR) is increased by only 6.2 % compared to 4 vol %. According to the results of the study, it is concluded that using volume fractions between 4 vol % to 6% would result in an observable improvement in convective heat transfer while enhanced entropy generation is relatively small, so it is thermodynamically affordable.
Keywords: ferrofluid, nanoparticle volume fraction, magnetic field, entropy generation, finite volume

Highlights
- *This paper represents a numerical investigation of laminar forced ferrofluid flow.*
- *A line diploe was used to generate the non-uniform external magnetic field.*
- *The effect of the Fe_3O_4 volume fraction on the hydro-thermal parameters has been investigated.*
- *As the external magnetic field is applied, the kelvin body force overcomes the viscous force.*

0 INTRODUCTION

Ferrofluids are colloidal suspensions comprised of a non-magnetic carrier liquid such as water, hydrocarbon oils or kerosene, and the single-domain ferromagnetic nanoparticles. They appear useful in heat transfer applications and other fields of practice. The magnetic behaviour of the ferrofluid is due to the magnetic nature of the solid phase spread into the liquid. The particles are usually 10 nm large, and they have bipolar magnets; an applied magnetic field causes them to take the same direction as the magnetic field lines and form a unique magnetic domain. To prevent the mixture from the aggregation that is caused by the existing magnetic forces between the particles while producing ferrofluid, they are coated with a 2 nm layer of liquid surfactant **[1]**. Ferrofluids have significant potential to alter the flow field through changing the magnetic field due to the bilateral effects of the fluid's nature and the magnetic properties of particles. Moreover, for every case-specific application, it is possible to regulate the magnetic force applied to the ferrofluid via an appropriate design of the external magnetic field. Ferro-hydrodynamic characteristic lengths differing from micro- to nano-scales bring a wide range of novel applications in the various fields of study **[2]**, including thermal engineering **[3]** and bio-engineering **[4]**. The transport of water in nanoconfined geometries is different than in the bulk phase and has tremendous implications in nanotechnology and biotechnology **[5]**. Using electromagnetic fields for micro-fluid applications presents a new method for controlling the ferrofluid **[6]**. Some applications such as pumping and mixing of the fluid in the micro-dimension apparatuses are possible through the electromagnetic body force (Lorentz force). The Lorentz force is created by an interaction between a magnetic field and an electric current, which is usually provided externally **[7]**. As the heat and momentum transfer are limited to small apparatuses, using an external magnetic field can improve the convective heat transfer characteristics inside them. This issue becomes significant in devices working based on free convection heat transfer for which the dimensions of the geometry are tiny, or the effect of gravity is negligible. Furthermore, with increasing interest in micro-scale heat exchangers used in microelectromechanical systems (MEMS)

*Corr. Author's Address: Department of Mechanical Engineering, University of Sistan and Baluchestan, Zahedan, Iran, fsarhaddi@eng.usb.ac.ir

systems, the application range of ferrofluids has risen considerably. To have an optimal design and a handy control over thermomagnetic heat transfer applications, it is essential to determine the relationship between the applied magnetic field, the ferrofluid flow, and temperature distribution.

Finlayson [8] investigated thermomagnetic convection heat transfer and analytically computed a parameter for the critical stability of this type of convection. Tangthieng et al. [9] numerically investigated the heat transfer of ferrofluid flow between two flat plates and within a square enclosure subjected to a steady magnetic field. Their results indicated that heat transfer caused by the magnetic field gradient is increased significantly. Tzirtzilakis et al. [10] worked on the flow of a biological magnetic fluid in a 3D rectangular duct. Assuming a viscous, laminar, incompressible and developed flow, they simulated a nonconductor biomagnetic fluid under the influence of an external magnetic field. Their research showed that the flow is considerably affected by the magnetic field. Ganguly et al. [2] conducted research on the heat and mass transfer in ferrofluids with application in the MEMS and biomedicine. Their final results suggested that the effect of the external field is nude unless kelvin force overcomes viscous force and heat transfer increases with the strengthening of the magnetic field. Jafari et al. [11] simulated heat transfer of the kerosene-based ferrofluid using a CFD method inside a cylindrical geometry with a two-phase mixture model. They used a range of temperature gradients and magnetic fields. They showed that transfer phenomena increase in the presence of magnetic field. They also demonstrated that, when magnetic particles are aggregated, heat transfer decreases. They concluded that magnetic fields perpendicular to the temperature gradient cause a greater deal of heat transfer in comparison to that of a parallel situation. Lajvardi et al. [12] carried out an experimental investigation on the convective heat transfer of a ferrofluid flowing through a heated copper tube under an applied magnetic field. A significant increase in the amount of heat transfer by applying magnetic field was observed in their experiments. In addition, they examined the effect of magnetic nanoparticle concentration and the magnet position. Their examinations suggested that the main reason behind the increase of heat transfer coefficient is owing to the considerable enhancement in thermo-physical properties of the ferrofluid, which happens because of applying the magnetic field. Aminfar et al. [13] numerically investigated the hydrothermal behaviour of a ferrofluid (water and 4 vol % magnetite) in a rectangular vertical duct using two-phase mixture model and control volume technique under the influence of a transverse magnetic field. Their results showed that applying magnetic fields increases the Nusselt number and friction factor and also creates a pair of vortices, which prevents nanoparticles from aggregating and enhances heat transfer. Afrand et al. [14] investigated the effect of the magnetic field intensity, the Hartmann number, the Rayleigh number, the angle of magnetic field application, the ratio of the inner to outer radii of the annulus on the flow, and the temperature field of molten gallium in a long annulus between two horizontal cylinders. They found that with an increase in the Rayleigh number, the change in Nu with the magnetic field intensity does not occur. Natural convection of an electrically conducting fluid in a tilted cylindrical annulus under the influence of a magnetic field was carried out numerically by the same team of researchers [15]. They showed that the effect of the transverse magnetic field is more significant than that of the axial magnetic field on the average Nusselt number. In another work, Afrand et al. [16] performed 3D numerical simulation and multi-objective optimization of natural convection in a cylindrical annulus mould filled with molten potassium under a magnetic field. Mahmoodi et al. [17] studied magneto-hydrodynamic (MHD) natural convection fluid flow and heat transfer in a square enclosure filled with liquid gallium with a pair of source and sink on its walls. They investigated the effects of the Rayleigh number, the Hartman number, and the locations of the source and sink on the fluid flow and heat transfer inside the enclosure. Their results showed that the flow and temperature distributions inside the enclosure are affected by the strength of the magnetic field, the Rayleigh number, and the relative location of the heat source and sink. Malvandi et al. [18] investigated MHD mixed convection of alumina/water nanofluid inside a vertical annular pipe. They used a model for the nanofluid mixture involving Brownian motion and thermophoresis diffusivities in order to take into account the effects of nanoparticle migration. They showed that the advantage of nanofluids in heat transfer enhancement was reduced in the presence of a magnetic field. Recently Goshayeshi et al. [19] through an experimental work studied the effect of Fe_2O_3/Kerosene nanofluid to the copper closed-loop oscillating heat pipe under the magnetic field for inclination angles ranging from 0° to 90°, under different heat inputs (10 W to 90 W). They showed that Fe_2O_3 nanoparticles could improve the thermal resistance and subsequently thermal performance as

well as the pipe's heat transfer coefficient, especially under the magnetic field.

The problem of entropy generation has attracted a great deal of attention in various engineering applications including heat exchangers, turbo machinery, electronic cooling systems, combustion engines, etc.

Thermodynamic irreversibility is related to entropy generation as a phenomenon appearing in every heat transfer Process. Various factors such as heat transfer and viscous losses affect the entropy generation. Bejan [20] studied entropy generation due to the heat transfer and fluid viscosity as an objective function for geometry optimization of pipes in a heat exchanger. He showed that entropy generation in forced flow convective heat transfer is due to temperature gradient and viscous effects of the fluid. Ibanez et al. [7] optimized an MHD fluid flowing through two infinite parallel plates of limited conductivity by means of the entropy minimization method. They aimed to minimize the total energy loss caused by irreversibilities, which are due to several factors including thermal conductivity, viscous losses, and the Joule dissipations. Thus, they analytically solved velocity, temperature and electric current density fields for computing total entropy generation in terms of the dimensionless parameters of the problem. They demonstrated that with decreasing wall temperatures, entropy generation reaches a minimum value. Mahian et al. [21] analytically studied the first and the second laws of thermodynamics for MHD flow between two rotating cylinders and investigated the effect of MHD flow on the velocity, temperature and entropy generation distribution between them. They investigated the effect of the Hartman number, Brinkman number and radius ratio on the entropy generation. Their investigation suggested that increasing the Hartman number, results in increasing average entropy generation. Rashidi et al. [22] studied effects of magnetic interaction number, slip factor and relative temperature difference on velocity and temperature profiles as well as entropy generation in MHD flow of a fluid with variable properties over a rotating disk using numerical methods. Recently Mojumder et al. [23] numerically analysed magneto-hydrodynamic convection in a half-moon shaped cavity filled with ferrofluid. They used cobalt-kerosene and Fe_3O_4-water ferrofluids for their investigation. They concluded that the entropy generation is increased with the increment of *Ra*, the decrement of *Ha* and a moderate inclination angle (γ = 45°). They found that ferrofluid always causes higher entropy generation and at the same time higher heat transfer rate. Finally, they suggested that the optimum value of solid volume fraction of ferrofluid should be used to optimize the entropy and to enhance the heat transfer simultaneously. However, there is no significant research into entropy generation caused by temperature difference, friction factor and energy losses in ferrofluids. Although, owing to the wide range of ferrofluid applications in industry, the entropy generation investigation can be beneficial and may provide basic knowledge for selecting design parameters in systems of such type. Furthermore, studying thermal and hydrodynamic parameters and entropy generation in ferrofluids seems to be essential for recognizing and eliminating or optimizing the leading causes of energy losses in the system. This research studies the effect of Fe_3O_4 volume fraction on the flow, heat transfer and entropy generation of the water-Fe_3O_4 ferrofluid through numerical investigation.

The problem chosen in this study is supposed to have a small geometry (millimetre order) with low Reynolds numbers. The domain of applications related to this problem is comprehensive, for example in small devices like MEMS, heat exchangers and cooling systems for electronic devices as a possible alternative for natural convection.

1 PROBLEM DESCRIPTION AND GOVERNING EQUATIONS

The main target in the present work is to investigate the effect of Fe_3O_4 volume fraction as the magnetic nanoparticle with a diameter of 10 nm on the hydro-thermal parameters and entropy generation of the ferrofluid. The geometry in which the ferrofluid flows is a two-dimensional rectangular channel (20 mm × 2 mm) in the axial and transverse directions, respectively). The effect of gravitation is neglected due to the small geometry. A line dipole with a dipole strength of 0.1 Am is placed 1 mm below the lower channel wall halfway along the channel length, acting as the external 2D magnetic field. Heated ferrofluid at characteristic Reynolds number Re=20, enters the channel with the temperature of 344 K. The lower wall is considered to be an isothermal heat sink at 300 K, while the upper wall is adiabatic (Fig. 1). The laminar ferrofluid flow is assumed to be steady state, incompressible, and viscous. The effect of the magnetic field on the viscosity and thermal conductivity of the ferrofluid is not considered, and the Lorentz force caused by electric conductivity has been neglected in comparison to the magnetization.

The Knudsen number is given by $Kn=\lambda/L_s$ where λ is the mean free path in a gas and L_s is the

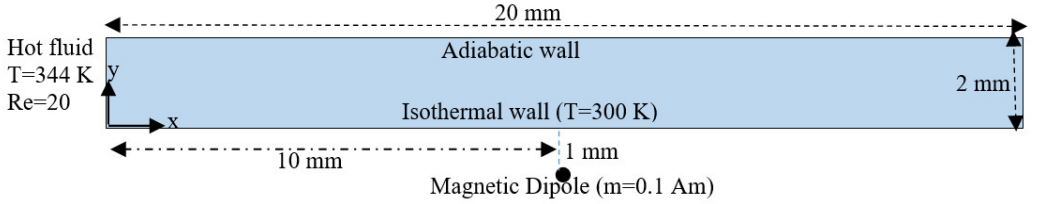

Fig. 1. *Schematic diagram of the physical model*

characteristic channel length. For liquids, the lattice spacing δ can be used as an alternative to mean free path. For water, this spacing is 0.3 nm [24]. In this work L_s is the channel height; therefore, the Knudsen number is approximately about 1.5×10^{-7}, and the continuum flow assumption is satisfied.

Considering all the aforementioned assumptions, the governing equations of the problem are as follows:

- continuity equation:

$$\nabla\cdot\boldsymbol{V}=0, \tag{1}$$

- momentum equation:

$$\rho_{eff}\nabla\cdot(\boldsymbol{VV})=-\nabla p+\nabla\cdot\left(\mu_{eff}\nabla\boldsymbol{V}\right)+(\boldsymbol{M}\cdot\nabla)\boldsymbol{B}, \tag{2}$$

where **V** is the velocity vector, ρ_{eff} is ferrofluid's density and μ_{eff} is effective viscosity. The last term in Eq. (2) $(\boldsymbol{M}\cdot\nabla)\boldsymbol{B}$ is called Kelvin body force. This force is owing to the existence of the magnetic gradient. As it is assumed that the ferrofluid does not conduct electric current, Maxwell's equations are obtained as:

$$\nabla\cdot\boldsymbol{B}=0, \tag{3}$$

and

$$\nabla\times\boldsymbol{H}=0. \tag{4}$$

In Eqs. (3) and (4), $\boldsymbol{B}$ and $\boldsymbol{H}$ are magnetic induction and magnetic field intensity, respectively. If we define $\boldsymbol{M}$ as the magnetization created inside the ferrofluid, $\boldsymbol{B}$, $\boldsymbol{M}$, and $\boldsymbol{H}$ are related to each other through $\boldsymbol{B}=\mu_0(\boldsymbol{M}+\boldsymbol{H})$. When a ferrofluid is exposed to an external magnetic field, magnetic dipoles of nanoparticles become aligned with the direction of the external field vectors. The magnitude of magnetization is a function of the external magnetic field and temperature [8] and [25]:

$$\boldsymbol{M}=M(H,T)\frac{\boldsymbol{H}}{H}, \tag{5}$$

where T is the temperature, $H=|\boldsymbol{H}|$ is the magnitude of the applied magnetic field, and $M=|\boldsymbol{M}|$ is the value of magnetization created inside the ferrofluid [25]. According to Aminfar et al. [13], magnetization is defined as follows:

$$M=M_sL(\xi)=\frac{6m_p\varphi}{\pi d_p^3}\left(\coth(\xi)-\frac{1}{\xi}\right). \tag{6}$$

In Eq. (6), M_s is the saturated magnetization of the particles, φ is the volume fraction of magnetic particles, m_p is the particle magnetic moment, d_p is diameter, and ξ is the Langevin parameter. A unit cell of the crystal structure of magnetite (Fe_3O_4) has a volume of 730 Å^3 and includes 8 molecules of Fe_3O_4, each of which has a magnetic moment of $4\mu_B$. The magnetic moment of magnetite particles is then obtained from Eq. (7):

$$m_p=\frac{4\mu_B\pi d_p^3}{6\times91.25\times10^{-30}}. \tag{7}$$

Langevin parameter is the ratio of magnetic energy to thermal energy which is given by:

$$\xi=\frac{\mu_0m_pH}{k_BT}, \tag{8}$$

where μ_B is the Bohr magneton which equals 9.27×10^{-24} (Am^2) in SI system. The other parameter k_B, is the Boltzmann's constant, which relates the energy level of particle and its temperature. This value is the relative magnitude of the universal gas constant and Avogadro number which equals 1.3806503×10^{-23} J/K. Langevin's function is used to describe the competent behaviour between disordering (random thermal), and ordering (magnetic torque) mechanisms [1] and is defined by Eq. (9):

$$L(\xi)=\coth(\xi)-\frac{1}{\xi}. \tag{9}$$

External magnetic field components made by line dipole in x and y directions are H_x and H_y which are defined through Eqs. (10) and (11), respectively.

$$H_x(x,y)=\frac{2m(x-a)(y-d)}{(x-a)^2+(y-d)^2}, \tag{10}$$

and

$$H_y(x,y)=\frac{m\left[(y-d)^2-(x-a)^2\right]}{(x-a)^2+(y-d)^2}. \tag{11}$$

In Eqs. (10) and (11), m is the magnetic dipole strength per unit length of the electromagnetic coil, which is defined as $m=Ib/2\pi$, I is electric current inside the coil, b is the distance between the conductors, and (a,d) represents the coordinates of the dipole. The magnitude of the magnetic field is computed in Eq. (12):

$$H(x,y)=\frac{m}{(x-a)^2+(y-d)^2}. \tag{12}$$

Through defining magnetic susceptibility as $\chi_m=\boldsymbol{M}/\boldsymbol{H}$, the relationship between magnetization and the external magnetic field becomes:

$$\boldsymbol{M}=\frac{M_s L(\xi)}{H}\boldsymbol{H}=\chi_m \boldsymbol{H}. \tag{13}$$

Magnetic susceptibility of ferrofluid is a dimensionless number that depends on the temperature and the applied magnetic field. Substituting Eq. (13) into Eq. (5), we obtain:

$$\boldsymbol{B}=\mu_0(1+\chi_m)\boldsymbol{H}. \tag{14}$$

Eq. (14) correlates magnetic induction into ferrofluid with the applied magnetic field. The energy equation for incompressible and steady state ferrofluid flow assuming single phase model is as follows [8]:

$$\left[(\rho C_p)_{nf}-\mu_0\boldsymbol{H}\cdot\left(\frac{\partial M}{\partial \mathrm{T}}\right)_H\right]\boldsymbol{V}.\nabla T+$$
$$+\mu_0 T\left(\frac{\partial \boldsymbol{M}}{\partial T}\right)_H\cdot(\boldsymbol{V}\cdot\nabla\boldsymbol{H})=\nabla\cdot(k_{nf}\nabla T)+\mu_{nf}\Phi, \tag{15}$$

where Φ is the loss function that expressed as below:

$$\Phi=2\left[\left(\frac{\partial u}{\partial x}\right)^2+\left(\frac{\partial v}{\partial y}\right)^2\right]+\left[\left(\frac{\partial u}{\partial y}+\frac{\partial v}{\partial x}\right)^2\right]. \tag{16}$$

The entropy generation equation in the absence of electrical effects is as follows [26]:

$$S_G=\frac{k_{eff}}{T_0}(\nabla T)^2+\frac{\mu_{eff}}{T_0}\Phi. \tag{17}$$

The ferrofluid's physical properties in the aforementioned equations are as below:

- ferrofluid's density:

$$\rho_{eff}=\varphi\rho_p+(1-\varphi)\rho_f, \tag{18}$$

- dynamic viscosity [27]:

$$\mu_{eff}=\mu_f(1+2.5\varphi+6.5\varphi^2), \tag{19}$$

- effective thermal conductivity for spherical nanoparticles [28]:

$$k_{eff}=\frac{k_p+2k_f-2\varphi(k_f-k_p)}{k_p+2k_f+\varphi(k_f-k_p)}k_f, \tag{20}$$

- effective specific heat:

$$(\rho C_p)_{eff}=(1-\varphi)(\rho C_p)_f+\varphi(\rho C_p)_p. \tag{21}$$

1.1 Boundary Conditions

The governing equations have been subjected to the following boundary conditions:

- At the inlet (i.e. $x/h=0$), hot ferrofluid enters with a temperature of T_h at characteristic Reynolds $\mathrm{Re}=20$:

$$\frac{x}{h}=0,\quad u=u_\infty,\quad v=0,\quad T=T_h. \tag{22}$$

- At the lower wall, the non-slip condition is established and imposed at constant cold temperature of T_c:

$$\frac{y}{h}=0,\quad u=v=0,\quad T=T_c. \tag{23}$$

- There is a non-slip condition on the upper wall, which is considered to be adiabatic:

$$\frac{y}{h}=1,\quad u=v=0,\quad \frac{\partial T}{\partial y}=0. \tag{24}$$

- At the outlet (i.e. $x/h=10$), the atmospheric pressure is assumed.

2.3 Dimensionless Parameters

In order to investigate hydrodynamic and thermal behaviour, as well as entropy generation in the ferrofluid in the present work, the dimensionless numbers of friction factor on the lower wall, Nusselt number, dimensionless temperature, and entropy generation is defined as follows:

The Reynolds number is the ratio of inertial forces to viscous forces and defined as below:

$$\mathrm{Re}=\frac{\rho_{eff}u_\infty h}{\mu_{eff}}. \tag{25}$$

The Nusselt number is defined as the ratio of convective heat transfer into heat transferred by conduction in system boundaries. The local Nusselt number on isothermal wall is given by:

$$Nu = \frac{q_w^{"} h}{k_{eff}\left(T_b - T_c\right)}, \tag{26}$$

where T_b in is the bulk temperature of ferrofluid flow which is obtained as:

$$T_b = \frac{\int_0^h uTdy}{\int_0^h udy}. \tag{27}$$

The average Nusselt number is obtained by the integration of Eq. (28) in the longitudinal direction.

$$\overline{Nu} = \frac{1}{L}\int_0^L Nu\, dx. \tag{28}$$

The friction factor on the bottom wall can be achieved from Eq. (30).

$$C_f = \frac{\tau_w}{\frac{1}{2}\rho_{eff} u_\infty^2}, \tag{29}$$

where:

$$\tau_w = \mu_{eff} \left.\frac{\partial u}{\partial y}\right|_{wall}. \tag{30}$$

Dimensionless entropy generation number:

$$Ns = \frac{S_g}{S_{g0}}, \tag{31}$$

where, S_{g0} is the characteristic entropy generation rate [29]:

$$S_{g0} = k_{eff}\left(\frac{\Delta T}{hT_0}\right)^2. \tag{32}$$

In Eq. (32), $\Delta T = T_h - T_c$ and T_0 is the reference temperature which is 300 K. the average entropy generation rate is obtained by integrating Eq. (31) over the whole volume from the Eq. (33) given below:

$$\overline{Ns} = \frac{1}{\forall}\int_{\forall} Nsd\forall, \tag{33}$$

where $\forall$ presents the volume of the whole channel.

Dimensionless temperature:

$$\theta_b = \frac{T_b - T_c}{T_h - T_c}. \tag{34}$$

2 NUMERICAL METHOD

Because of the non-linearity of coupled governing differential equations, the numerical method was chosen to solve them. The control volume technique was applied to discretize continuity, momentum and energy equations. For convective and diffusive terms, a second order upwind method was applied while a simple algorithm was developed for pressure-velocity coupling. A structured grid has been used to discretize the computational domain (Fig. 2). As can be seen, the grid is finer near the dipole, because of higher gradient amounts in this area.

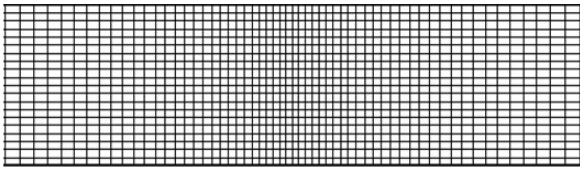

Fig. 2. *Schematic of grid*

Several different grid distributions were examined to ensure that the results are grid independent. For this purpose, the ferrofluid (water and 6 vol % Fe_3o_4) flow into a channel under a magnetic dipole with a strength of 0.1 Am and Reynolds number equal to 20 has been considered. Physical properties of the base fluid (water) and particles (Fe_3O_4) at the temperature of 25 ºC are presented in Table 1.

Table 1. *Properties of the water and magnetite*

property	water	Fe_3O_4
ρ	998.2 kg/m³	5200 kg/m³
C_p	4184.8 J/(kg K)	670 J/(kg K)
k	0.6 W/(m K)	6 W/(m K)
μ	0.001 kg/(m s)	-
diameter	0.2 nm	10 nm

The grid used for calculation has 300 and 90 nodes in the x and y directions, respectively. As shown in Table 2, a further increase of grid nodes does not affect the results.

Table 2. *Grid independent test*

	Node number ($x \times y$)	$\overline{Nu}$	$\overline{Ns}$
x	200×40	5.6415	0.3413
	300×40	5.4822	0.3597
	450×40	5.4513	0.3612
y	300×40	5.4513	0.3612
	300×60	5.7432	0.3584
	300×90	5.9084	0.3458
	300×135	5.9119	0.3441

Because the same lab work has not been done in this context, in order to demonstrate the validity and accuracy of numerical results, a comparison with the

previously published numerical work using a water-based ferrofluid with the following properties at 300 K reference temperature: $\rho=1180\,kg/m^3$, $C_p=4180\,J/(kgK)$, $\mu_0=0.001\,kg/(m\cdot s)$, $Pr=5.5$ and $\chi_0=0.06$ under the influence of a line dipole has been done. The characteristic Reynolds number was $Re=11.8$ and a comparison was performed for dipole strength of 0.19 Am. Fig. 3 indicates the comparison of the bulk temperature along the channel between the present work with the numerical ones of Ganguly et al. [2].

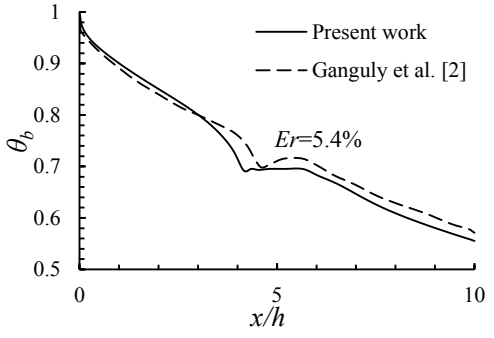

Fig. 3. *Comparison of the bulk temperature along the channel with same numerical results*

As seen, there is a good agreement between them and the average relative error (Er) is 5.4 %.

3 RESULTS AND DISCUSSION

In this work the forced flow of water-based ferrofluid consisting of 1 vol % to 6 vol % Fe_3O_4 particles with 10 nm mean diameter under the influence of a variable external magnetic field applied by a line dipole with dipole strength of 0.1 Am has been investigated numerically using control volume technique. The characteristic Reynolds number $Re=20$ has been considered, so the flow regime is laminar. In the absence of the external magnetic field and zero volume fraction of magnetic nanoparticles, the forced flow reaches a hydro-dynamically fully developed profile at a length of $x/h=2.284$ and achieves a constant velocity magnitude that is 1.5 times of the inlet ones. As the external magnetic field is applied, the kelvin body force overcomes the viscous force, and the fluid flow is strongly changed. Fig. 4a shows the kelvin body force distribution at 5 vol % Fe_3O_4. Vectors denote the kelvin body force direction while contours denote its magnitude. Furthermore, Fig. 4b demonstrate streamlines under the influence of external magnetic field at 5 vol % Fe_3O_4 particles.

Upstream of the dipole, the pressure-driven flow moves forward while a strong kelvin body force drives ferrofluid downward to the line dipole and causes significant momentum transfer toward the bottom wall. By moving ferrofluid toward the dipole at a distance of approximately 8 mm from the inlet ($x/h=4$) Vertical flow barrier due to the magnetic field has been generated then it creates a flow pattern similar to being a vertical wall in a two-dimensional channel; thus, around the dipole a large vortex is formed. Downstream of the dipole, the kelvin body force resists the viscous force that moves the ferrofluid forward, so the fluid near bottom wall recirculate towards the dipole. Fig. 5 shows the velocity magnitude changes in the longitudinal direction at $y/h=0.5$.

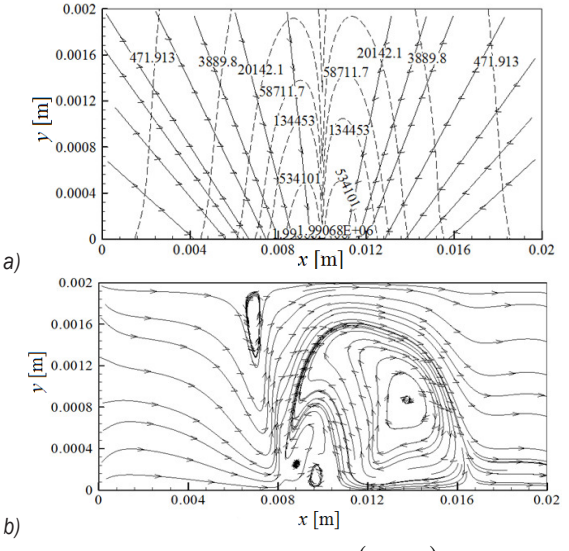

Fig. 4. *a) Kelvin body force distribution, $(\boldsymbol{M}\cdot\nabla)\boldsymbol{B}$ [N/m³], b) streamlines for 5 vol % Fe_3O_4 under influence of magnetic field*

As shown in Fig. 5, increasing the volume fraction of the Fe_3O_4 particles causes a slight reduction in the velocity magnitude at the inlet due to increasing the ferrofluid's density at a constant Reynolds number. Upstream the dipole, the velocity magnitude on the central line of channel reduces markedly because of the increasing kelvin body force by adding more volume fractions of Fe_3O_4 particles. As discussed, this force causes momentum transfer toward the bottom wall. Around the dipole, the vortex makes sinusoidal variations which their amplitude decreases gradually within approximately 8 mm after the dipole downstream and eventually a constant trend has been observed near the outlet. Owing to a larger kelvin body force caused by rising in the Fe_3O_4 volume fraction, more oscillations are observed in the velocity magnitude. The effect of Fe_3O_4 volume fraction on the kelvin body force in the longitudinal direction near the

bottom wall is presented in Fig. 6. As illustrated, the kelvin body force is symmetric about a vertical line passing through the dipole.

Applying the external magnetic field resulting from the dipole will increase the velocity and temperature gradients and leads to change in hydrodynamic and thermal parameters. Fig. 7 shows the variation of the friction factor on the bottom wall at different volume fractions.

It is seen that the friction factor has a relatively large amount at the inlet due to a high-velocity gradient. In the absence of an external magnetic field, the friction factor on the wall decreases along the channel length and reaches a constant amount in the hydrodynamic developed area. As said earlier, applying an external magnetic field while increasing Fe_3O_4 volume fraction will enhance the kelvin body force; thus, upstream the diploe the friction factor increases with a considerably sharp slope along the channel close to the dipole to reach a maximum value at the streamlines' jump due to the momentum transfer toward the bottom wall and consequently rising horizontal velocity gradient near the wall. Afterward, with a drop of the horizontal component of the velocity and upward ferrofluid flow, the friction factor diminishes such that reaches to the zero over the dipole. Downstream the dipole, first because of the backflow, friction factor becomes negative and finally away from dipole reaches to a constant positive amount near by the outflow. Fig. 8 depicts the effect of the Fe_3O_4 volume fraction on the average wall friction factor. As seen, with the increase in the Fe_3O_4 volume fraction, the mean wall friction factor enhances with a linear trend.

To characterize the overall effect of the Fe_3O_4 volume fraction on the pressure drop, the pumping work of the fluid $\dot{W}_p = \dot{m}\Delta p / \rho_{eff}$ (where $\dot{m} = \rho_{eff} u_\infty h$ and Δp is the total pressure difference between inlet and outlet) is presented in Fig. 9.

As seen, applying the external magnetic field enhances the required pumping work. Furthermore, the greater the volume fraction, the more pumping work is needed. Altering the flow field due to applying the magnetic field will cause to changes in temperature distribution. Fig. 10 shows the ferrofluid's temperature distribution under the influence of magnetic dipole strength $m = 0.1$ at 5 vol % Fe_3O_4.

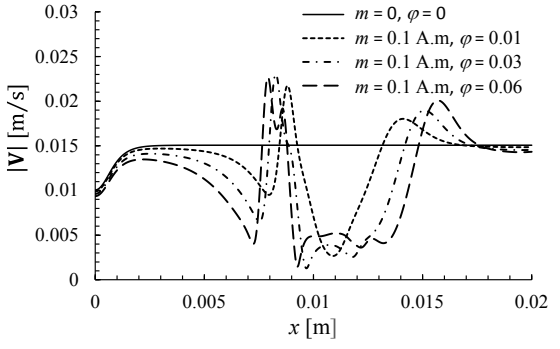

Fig. 5. *Comparison of the velocity magnitude in the longitudinal direction at y/h = 0.5 for different volume fractions.*

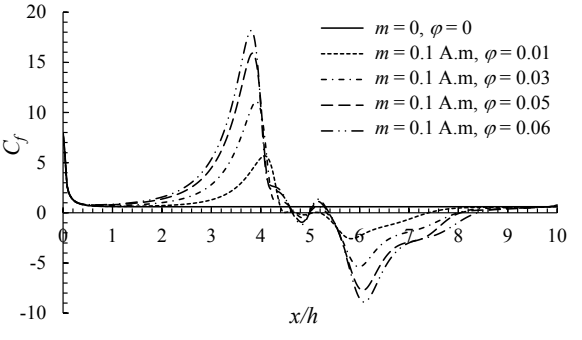

Fig. 7. *Variation of the wall friction factor along the channel length for different values of φ*

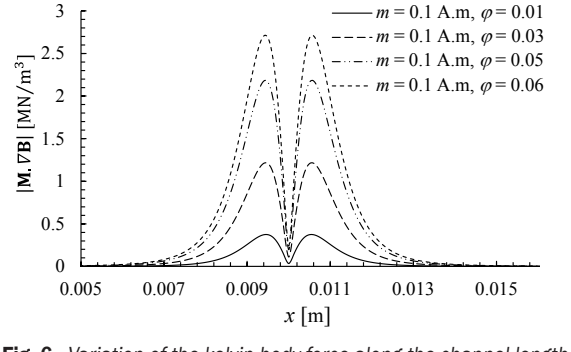

Fig. 6. *Variation of the kelvin body force along the channel length for different values of φ*

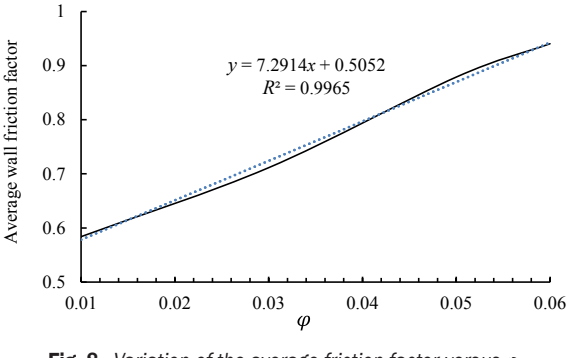

Fig. 8. *Variation of the average friction factor versus φ (m = 0.1 A m)*

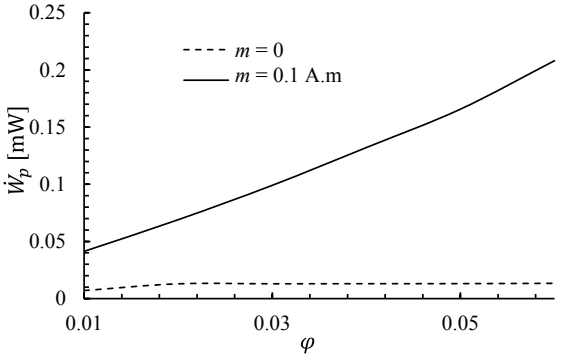

Fig. 9. *Effect of volume fraction on the pumping work*

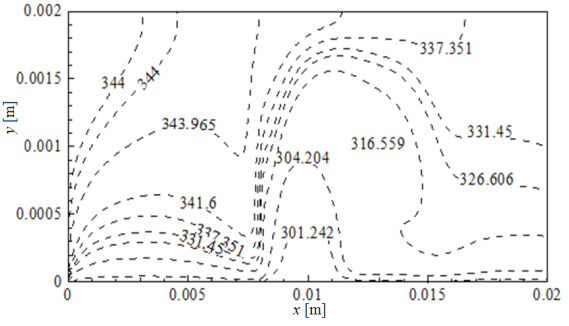

Fig. 10. *Temperature distribution at m = 0.1 and φ = 0.05*

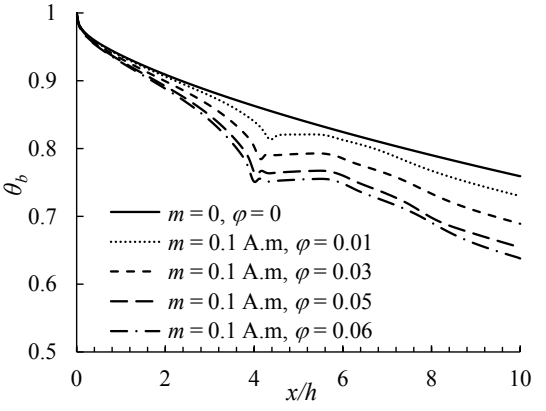

Fig. 11. *Variation of the bulk temperature along the channel length for different values of φ*

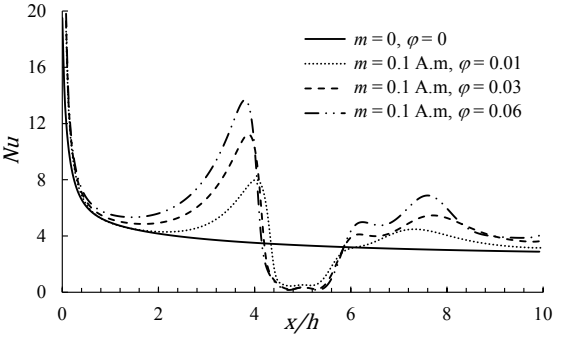

Fig. 12. *Variation of the local Nusselt number along the channel length at different volume fractions*

As the flow field changes, the temperature field is also altered accordingly such that a hump is made in the thermal boundary layer near the dipole. Upstream the dipole, the hot ferrofluid moves toward the bottom wall, and the thermal boundary-layer thickness is reduced. Due to the vertical motion of the ferrofluid before the dipole, the cold fluid near the downwall moves upward and downstream the diploe recirculates towards the dipole, so the thermal boundary-layer thickness Significantly increases. Fig. 11 indicates the variation of dimensionless bulk temperature along the channel length at different volume fractions.

As observed the bulk temperature is regularly reduced along the channel length in the absence of the magnetic field, while it will encounter a sudden drop around the dipole by adding magnetic nanoparticles and applying an external magnetic field. In fact, an augmentation in the Fe_3O_4 volume fraction creates a stronger vortex around the dipole, thus leading to an increase in heat transfer.

Altering the temperature distribution due to the exerted magnetic field causes changes in the temperature gradient within the ferrofluid. Thus, the convective heat transfer and the Nusselt number deals with change. Variation of *Nu* at different volume fractions is presented in Fig. 12.

In the absence of a magnetic field, the amount of *Nu* has been diminished from a maximum value at the inlet to 2.745 when *x*/*h* is 10. It is seen that exerting the magnetic field will increase the local *Nu* with a sharp slope upstream of the dipole. This is because of a high-temperature gradient at the wall, which has resulted in the reduction of the thermal boundary-layer thickness due to downward thermomagnetic convection. At the recirculation region above the dipole, colder ferrofluid formation prevents heat transfer; therefore, the local *Nu* is reduced. After this region, the thermal boundary-layer thickness decreases; the local *Nu* thus rises above the base fluid ones. An increase in the Fe_3O_4 volume fraction, causes the overall heat transfer and *Nu* to rise further from the base fluid. Fig. 13 depicts the effects of Fe_3O_4 volume fraction on the average Nusselt number. As seen, $\overline{Nu}$ is increased as more Fe_3O_4 particles is added, so that for 6 vol % Fe_3O_4, the $\overline{Nu}$ is enhanced by 51.1 % under the influence of the magnetic field and 8.5 % in the absence of a magnetic field in comparison to the base fluid.

The overall heat transfer is given by $Q = \dot{m}C_p\Delta T$, where ΔT is the bulk temperature difference between

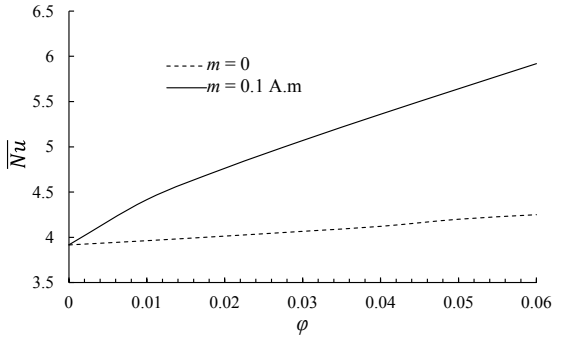

Fig. 13. *Effect of the Fe_3O_4 volume fraction on the average Nusselt number*

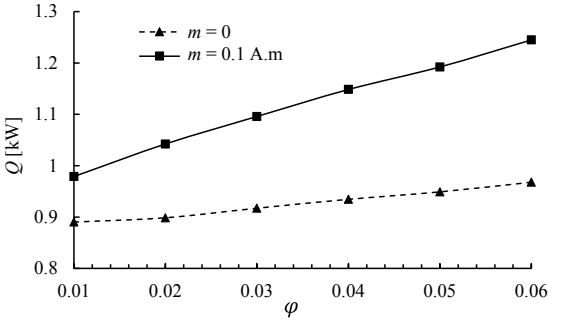

Fig. 14. *Effect of Fe_3O_4 volume fraction on the overall heat transfer*

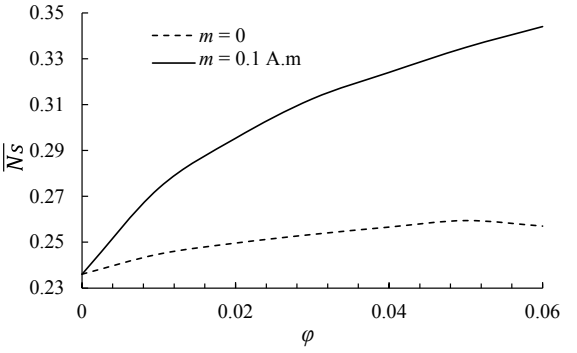

Fig. 15. *Effect of volume fraction on the average entropy generation*

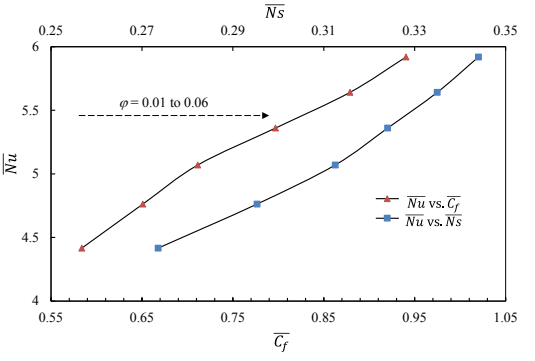

Fig. 16. *$\overline{Nu}$ versus $\overline{Ns}$ and $\overline{C}_f$ under magnetic dipole strength m = 0.1 A·m*

inlet and outlet. Fig. 14 shows the effect of Fe_3O_4 volume fraction on the overall heat transfer.

As illustrated the overall heat transfer increases by applying the external magnetic field, so that its maximum enhancement compared to the absence of a magnetic field accrues in 6 vol % Fe_3O_4 by 28.6%. Furthermore, the value of Q at 6 vol % with respect to 1 vol % Fe_3O_4 increases by 27.2% and 8.7% under magnetic dipole strength of m = 0.1 Am and without an external magnetic field, respectively. According to Figs. 9 and 14, the required pumping work can be neglected against the overall heat transfer.

The flow field and temperature distribution of ferrofluid is changed when an external magnetic field is applied; as a consequence of it, the velocity and temperature gradient of ferrofluid is altered. All these factors affect the entropy generation rate within the system. Fig. 15 depicts the effect of volume fraction on the average entropy generation. As seen, $\overline{Ns}$ increases with higher vol % of Fe_3O_4. Also applying the external magnetic field enhances $\overline{Ns}$ due to higher temperature and velocity gradients.

Fig. 16 shows the variation of $\overline{Nu}$ versus $\overline{Ns}$ and average wall friction factor under the influence of magnetic dipole strength m = 0.1 at different Fe_3O_4 volume fractions.

As seen, increasing nanoparticle volume fraction at the same time enhances $\overline{Nu}$, $\overline{Ns}$ and $\overline{C}_f$. In contrast, although adding nanoparticles to the base fluid increases the heat transfer rate, it also imposes an extra pumping work within the system and causes higher entropy generation. So the value of the solid volume fraction must be chosen so that the maximum heat transfer rate is obtained while having an optimum value of pumping work and entropy generation.

In order to have a better description for the effect of the Fe_3O_4 volume fraction on the thermomagnetic convection, the Nusselt number ratio and the entropy generation ratio have been developed as follows:

Nusselt number ratio:

$$NUR = \frac{\overline{Nu}}{Nu_{m=0,\varphi=0,\mathrm{Re}=20}}, \tag{35}$$

entropy generation ratio:

$$NSR = \frac{\overline{Ns}}{Ns_{m=0,\varphi=0,\mathrm{Re}=20}}. \tag{36}$$

Fig. 17 shows the effect of Reynolds number on the *NUR* and *NSR* within different Fe_3O_4 volume fraction under the influence of magnetic dipole strength $m = 0.1$.

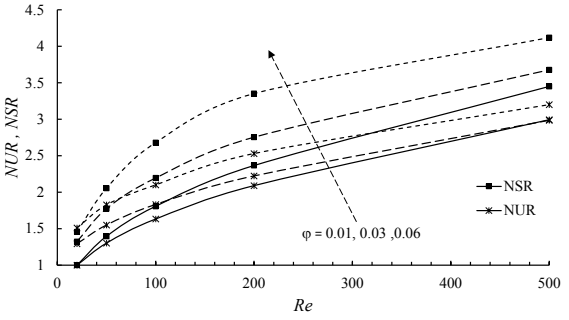

Fig. 17. *Effect of the Reynolds number and nanoparticles volume fraction on the NUR and NSR*

As expected, with an increase in the Reynolds number, both *NUR* and *NSR* enhance. Furthermore, a comparison has been carried out between different values of the Fe_3O_4 volume fractions. It is observed from Fig. 17 that using nanofluids at low Reynolds numbers have a good heat transfer performance while there is relatively less entropy generation.

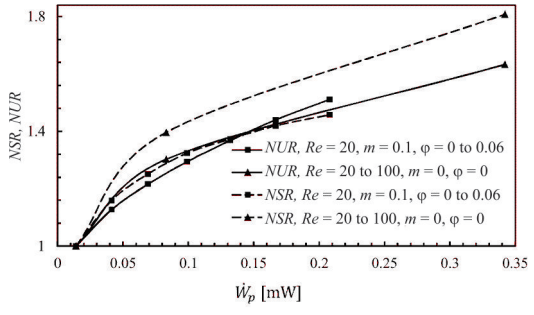

Fig. 18. *Comparison of the effect of base fluid Reynolds number and Fe_3O_4 volume fraction on the NUR and NSR*

Fig. 18 indicates the variation of *NUR* and *NSR* versus required pumping work for two cases of an accelerated base fluid without using nanoparticles and another non-accelerated nanofluid with different nanoparticle volume fractions of Fe_3O_4. As seen for a fixed value of the pumping work, at the low Reynolds numbers a slight increase in the base fluid *Re* (up to $Re = 60$) has a better effect on the heat transfer rate so that *NUR* for the accelerated base fluid is more than the non-accelerated nanofluid (volume fractions up to 0.04), but from the standpoint of thermodynamics causes higher entropy generation (more *NSR* compared to the non-accelerated nanofluid). At the higher values of the base fluid Reynolds number ($Re > 60$), the non-accelerated nanofluid with the volume fractions greater than 0.04 give a better heat transfer performance (more *NUR*) compared to the accelerated base fluid and also cause lower entropy generation.

With increased volume fraction of Fe_3O_4 up to 4 %, *NSR* within the system is greater than *NUR* while for the volume fractions between 0.04 and 0.06, this trend was reversed so that *NUR* at 6 vol % is enhanced by 10.4 % whereas *NSR* is increased by only 6.2 % compared to 4 vol % of the magnetic nanoparticles. This interesting result suggests that using volume fractions between 0.04 and 0.06, while increasing the convective heat transfer is also affordable, from the perspective of the second law of thermodynamics.

4 CONCLUSION

This paper represents a numerical investigation of laminar forced ferrofluid (consisting of water and Fe_3O_4 nanoparticles) flow through a tiny horizontal 2D channel by using the control volume technique. A line diploe was used to generate a non-uniform external magnetic field which is placed 1 mm below the lower channel wall halfway along the channel length. It was considered that the incompressible and viscous ferrofluid flow and the continuum flow assumption was satisfied. The effect of Fe_3O_4 volume fraction on the hydro-thermal parameters and entropy generation of the ferrofluid was studied.

- As the external magnetic field is applied, the kelvin body force overcomes the viscous force, so that the ferrofluid flow is strongly changed and a large vortex is formed around the dipole.
- Increasing the Fe_3O_4 volume fraction under the influence of the magnetic field causes more changes in the velocity and temperature fields, which leads to an obvious enhancement in the heat transfer.
- The required pumping work and average friction factor are enhanced by increasing the value of the Fe_3O_4 volume fraction.
- The average Nusselt number increases as more Fe_3O_4 particles are added, so that for 6 vol % Fe_3O_4, the $\overline{Nu}$ enhances by 51.1 % under the influence of the magnetic field and 8.5 % in the absence of a magnetic field in comparison to the base fluid.
- The results showed that the overall heat transfer is more affected in the presence of the external magnetic field, so that its value at 6 vol % with respect to 1 vol % Fe_3O_4 increases by 27.2 % and 8.7% under a magnetic dipole strength of

m = 0.1 Am and without an external magnetic field, respectively.

- The average entropy generation rises with higher vol % of Fe_3O_4, but the Nusselt number ratio at 6 vol % is enhanced by 10.4 % whereas entropy generation ratio increases by only 6.2 % compared to 4 vol % of the magnetic nanoparticles. This result emphasizes that using volume fractions ranging from 0.04 to 0.06 while increase the convective heat transfer, from the perspective of the second law of thermodynamics is also affordable.

6 NOMENCLATURE

a	x component of the dipole location [m]
$\boldsymbol{B}$	magnetic induction vector [T]
b	distance between the conductors [m]
C_f	friction factor
C_p	specific heat [J/(kg K)]
d	y component of the dipole location [m]
d_p	particle diameter [nm]
$\boldsymbol{H}$	magnetic field vector [A/m]
H_x	x component of magnetic field intensity [A/m]
H_y	y component of magnetic field intensity [A/m]
h	channel height [m]
I	current [A]
k	thermal conductivity [W/(m K)]
k_B	Boltzmann constant [1.3806503×10^{-23} J/K]
Kn	Knudsen number
L_s	characteristic channel length [m]
m	magnetic dipole moment per unit length [A·m]
$\boldsymbol{M}$	Magnetization vector [A/m]
m_p	particle magnetic moment [A·m²]
$\boldsymbol{V}$	velocity vector [m/s]
$\dot{W}_p$	pumping work [W]
x	axis in the Cartesian coordinate
y	axis in the Cartesian coordinate

Greek symbols

δ	Lattice spacing
ξ	Langevin parameter
θ	dimensionless temperature
λ	mean free path in a gas
μ	dynamic viscosity
μ_B	Bohr magneton
μ_0	magnetic permeability in vacuum
$\forall$	volume
Ms	saturation magnetization [A/m]
$\underline{Ns}$	Entropy generation number
$\overline{Ns}$	average entropy generation
NSR	entropy generation ratio
Nu	local Nusselt number
$\overline{Nu}$	average Nusselt number
NUR	Nusselt number ratio
P	pressure [Pa]
Pr	Prandtl number
Q	overall heat transfer [J/s]
q''_w	wall heat flux [W/m²]
Re	Reynolds number
S_g	entropy generation [W/(m³K)]
S_{g0}	characteristic entropy generation
T	temperature [K]
u	x component of velocity [m/s]
v	y component of velocity [m/s]
ρ	Fluid density [kg/m³]
τ	shear stress
φ	volume fraction

Subscripts

b	pertaining to bulk fluid
c	pertaining to cold fluid
eff	effective
f	pertaining to base fluid
h	pertaining to hot fluid
m	mean value
p	pertaining to particle
0	pertaining to reference conditions
w	pertaining to wall

7 REFERENCES

[1] Cruz-Fierro, C.F. (2003). *Coupled Momentum and Heat Transport in Laminar Axisymmetric Pipe Flow of Ferrofluids in Non-Uniform Magnetic Fields: Theory and Simulation*. MSc Thesis, Oregon State University, Oregon.

[2] Ganguly, R., Sen, S., Puri, I.K. (2004). Heat transfer augmentation using a magnetic fluid under the influence of a line dipole. *Journal of Magnetism and Magnetic Materials*, vol. 271, no. 1, p. 63-73, **DOI:10.1016/j.jmmm.2003.09.015**.

[3] Bigdeli, M.B., Fasano, M., Cardellini, A., Chiavazzo, E., Asinari, P. (2016). A review on the heat and mass transfer phenomena in nanofluid coolants with special focus on automotive applications. *Renewable and Sustainable Energy Reviews*, vol. 60, pp. 1615-1633, **DOI:10.1016/j.rser.2016.03.027**.

[4] Gizzatov, A., Key, J., Aryal, S., Ananta, J., Cervadoro, A., Palange, A.L., Fasano, M., Stigliano, C., Zhong, M., Mascolo, D.D., Guven, A., Chiavazzo, E., Asinari, P., Liu, X., Ferrari, M., Wilson, L.J., Decuzzi, P. (2014). Hierarchically structured magnetic nanoconstructs with enhanced relaxivity and cooperative tumor accumulation. *Advanced Functional Materials*, vol. 24, p. 4584-4594, **DOI:10.1002/adfm.201400653**.

[5] Chiavazzo, E., Fasano, M., Asinari, P., Decuzzi P. (2014). Scaling behaviour for the water transport in nanoconfined geometries. *Nature Comunication*, 5:3565, **DOI:10.1038/ncomms4565**.

[6] Qian, S., Bau, H.H. (2009). Magneto-hydrodynamics based microfluidics. *Mechanics Research Communications*, vol. 36, no. 1, p. 10-21, **DOI:10.1016/j.mechrescom.2008.06.013**.

[7] Ibánez, G., Cuevas, S., López de Haro, M. (2006). Optimization of a magneto-hydrodynamic flow based on the entropy generation minimization method. *International Communications in Heat and Mass Transfer*, vol. 33, no. 3, p. 295-301, **DOI:10.1016/j.icheatmasstransfer.2005.12.003**.

[8] Finlayson, B.A. (1970). Convective instability of ferromagnetic fluids. *Journal of Fluid Mechanics*, vol. 40, no. 4, p. 753-767, **DOI:10.1017/S0022112070000423**.

[9] Tangthieng, C., Finlayson, B.A., Maulbetsch, J., Cader, T. (1999). Heat transfer enhancement in ferrofluids subjected to steady magnetic fields. *Journal of Magnetism and Magnetic Materials*, vol. 201, no. 1-3, p. 252-255, **DOI:10.1016/S0304-8853(99)00062-1**.

[10] Tzirtzilakis, E.E., Sakalis, V.D., Kafoussias, N.G., Hatzikonstantinou, P.M. (2004). Biomagnetic fluid flow in a 3D rectangular duct. *International Journal for Numerical Methods in Fluids*, vol. 44, no. 12, p. 1279-1298, **DOI:10.1002/fld.618**.

[11] Jafari, A., Tynjälä, T., Mousavi, S.M., Sarkomaa, P. (2008). Simulation of heat transfer in a ferrofluid using computational fluid dynamics technique. *International Journal of Heat and Fluid Flow*, vol. 29, no. 4, p. 1197-1202, **DOI:10.1016/j.ijheatfluidflow.2008.01.007**.

[12] Lajvardi, M., Moghimi-Rad, J., Hadi, I., Gavili, A., Dallali Isfahani, T., Zabihi, F., Sabbaghzadeh, J. (2010). Experimental investigation for enhanced ferrofluid heat transfer under magnetic field effect. *Journal of Magnetism and Magnetic Materials*, vol. 322, no. 21 p. 3508–3513, **DOI:10.1016/j.jmmm.2010.06.054**.

[13] Aminfar, H., Mohammadpourfard, M., Ahangar Zonouzi, S. (2013). Numerical study of the ferrofluid flow and heat transfer through a rectangular duct in the presence of a non-uniform transverse magnetic field. *Journal of Magnetism and Magnetic Materials*, vol. 327, p. 31-42, **DOI:10.1016/j.jmmm.2012.09.011**.

[14] Afrand, M., Farahat, S., Hossein Nezhad, A., Sheikhzadeh, G.A., Sarhaddi, F. (2014). Numerical simulation of electrically conducting fluid flow and free convective heat transfer in an annulus on applying a magnetic field. *Heat Transfer Research*, vol. 45, no. 8, p. 749-766, **DOI:10.1615/HeatTransRes.2014007285**.

[15] Afrand, M., Farahat, S., Hossein Nezhad, A., Sheikhzadeh, G.A., Sarhaddi, F. (2014). 3-D numerical investigation of natural convection in a tilted cylindrical annulus containing molten potassium and controlling it using various magnetic fields. *International Journal of Applied Electromagnetics and Mechanics*, vol. 46, no. 4, p. 809-821, **DOI:10.3233/JAE-141975**.

[16] Afrand, M., Farahat, S., Hossein Nezhad, A., Sheikhzadeh, G.A., Sarhaddi, F., Wongwises, S. (2015). Multi-objective optimization of natural convection in a cylindrical annulus mold under magnetic field using particle swarm algorithms. *International Communications in Heat and Mass Transfer*, vol. 60, p. 13-20, **DOI:10.1016/j.icheatmasstransfer.2014.11.006**.

[17] Mahmoodi, M., Esfe, M.H., Akbari, M., Karimipour, A., Afrand, M. (2015). Magneto-natural convection in square cavities with a source-sink pair on different walls. *International Journal of Applied Electromagnetics and Mechanics*, vol. 47, no. 1, p. 21-32, **DOI:10.3233/JAE-130097**.

[18] Malvandi, A., Safaei, M.R., Kaffash, M.H., Ganji, D.D. (2015). MHD mixed convection in a vertical annulus filled with Al203-water nanofluid considering nanoparticle migration. *Journal of Magnetism and Magnetic Materials*, vol. 382, p. 296-306, **DOI:10.1016/j.jmmm.2015.01.060**.

[19] Goshayeshi, H.R., Goodarzi, M., Safaei, M.R., Dahari, M. (2016). Experimental study on the effect of inclination angle on heat transfer enhancement of a ferrofluid in a closed loop oscillating heat pipe under magnetic field. *Experimental Thermal and Fluid Science*, vol. 74, p. 265-270, **DOI:10.1016/j.expthermflusci.2016.01.003**.

[20] Bejan, A. (1982). *Entropy Generation through Heat and Fluid Flow*, Wiley, New York.

[21] Mahian, O., Mahmud, Sh., Pop, I. (2012). Analysis of first and second laws of thermodynamics between two isothermal cylinders with relative rotation in the presence of MHD flow. *International Journal of Heat and Mass Transfer*, vol. 55, no. 17-18, p. 4808-4816, **DOI:10.1016/j.ijheatmasstransfer.2012.04.048**.

[22] Rashidi, M.M., Kavyani, N., Abelman, S. (2014). Investigation of entropy generation in MHD and slip flow over a rotating porous disk with variable properties. *International Journal of Heat and Mass Transfer*, vol. 70, p. 892-917, **DOI:10.1016/j.ijheatmasstransfer.2013.11.058**.

[23] Mojumder, S., Rabbi, Kh.Md., Saha, S., Hasan, M.N., Saha, S.C. (2016). Magnetic field effect on natural convection and entropy generation in a half-moon shaped cavity with semi-circular bottom heater having different ferrofluid inside. *Journal of Magnetism and Magnetic Materials*, vol. 407, p. 412-424, **DOI:10.1016/j.jmmm.2016.01.046**.

[24] Sharp, K.V., Adrian, R.J., Santiago, J.G., Molho, J.I. (2001). *Liquid Flows in Microchannels*. The MEMS Handbook, Gad-El-Hak, M. (ed.), CRC Press, Boca Raton, p. 6.1-6.38, **DOI:10.1201/9781420050905.ch6**.

[25] Shivakumara, I.S., Lee, J., Ravisha, M., Gangadhara Reddy, R. (2011). Effects of MFD viscosity and LTNE on the onset of ferromagnetic convection in a porous medium. *International Journal of Heat and Mass Transfer*, vol. 54, no. 11-12, p. 2630-2641, **DOI:10.1016/j.ijheatmasstransfer.2011.01.022**.

[26] Arikoglu, K., Ozkol, I., Komurgoz, G. (2008). Effect of slip on entropy generation in a single rotating disk in MHD flow. *Applied Energy*, vol. 85, no. 12, p. 1125-1236, **DOI:10.1016/j.apenergy.2008.03.004**.

[27] Batchelor, G.K. (1977). The effect of Brownian motion on the bulk stress in a suspension of spherical particles. *Journal of Fluid Mechanics*, vol. 83, no. 1, p. 97-117, **DOI:10.1017/S0022112077001062**.

[28] Hamilton, R.L., Crosser, O.K. (1962). Thermal conductivity of heterogeneous two-component system. *Industrial and Engineering Chemistry Fundamentals*, vol. 1, no. 3, p. 187-191, **DOI:10.1021/i160003a005**.

[29] Saleem, M., Anwar Hossain, Md., Mahmud, Sh., Pop, I. (2011). Entropy generation in Marangoni convection flow of heated fluid in an open ended cavity. *International Journal of Heat and Mass Transfer*, vol. 54, no. 21-22, p. 4473-4484, **DOI:10.1016/j.ijheatmasstransfer.2011.06.033**.

Strojniški vestnik - Journal of Mechanical Engineering 62(2016)9, 534-542

DOI:10.5545/sv-jme.2015.3071 Original Scientific Paper
Received for review: 2015-09-28
Received revised form: 2016-02-18
Accepted for publication: 2016-05-04

Dynamic Characterization of Microcantilevers with a Shock Wave Excitation Method under High Temperature

Dongsheng She[1,*] – Yiliu Yang[2] – Zefei Wei[1] – Zhen Yu[1]
[1]Bohai University, College of Engineering, China
[2]Bohai University, Research and Teaching Institute of College Computer Science, China

Aiming at the dynamic characteristics of silicon microcantilevers under a high-temperature environment, a shock wave excitation method was proposed, and a dynamic testing system with high-temperature loading unit for MEMS microstructures was established. In the system, the shock wave generated by electrical discharging was used to excite the testing microcantilever. The vibration response signals were acquired by laser Doppler vibrometer system. A T-shaped microcantilever and a microcantilever with uniform rectangular crossing section were fabricated and tested under the high-temperature environment ranging from 299 K to 773 K. Their temperature coefficients of natural frequency were obtained. The results show that for both two microcantilevers, the temperature coefficients of the natural frequency is very close to each other, which is only decided by the temperature coefficient of the elastic modulus and the linear thermal expansion coefficients.
Keywords: dynamic characteristics testing, microcantilever, shock wave, temperature coefficient of natural frequency, high temperature

Highlights
- *The temperature coefficient of natural frequency of a single crystal silicon microcantilever was reported.*
- *A shock wave excitation method was proposed to excite the microcantilevers in a high-temperature environment.*
- *The T-shaped silicon microcantilever and the silicon microcantilever with uniform rectangular crossing section have the same TCF.*
- *The TCF of the single crystal silicon microcantilever is negative.*
- *Results can be used in the design of MEMS sensors and actuators for high-temperature application.*

0 INTRODUCTION

Microelectromechanical system (MEMS) sensors and actuators have shown great potential in many areas including automotive, aerospace, missile weapon and nuclear power, etc. [1] and [2]. Thus, there is a need for MEMS devices to work in high-temperature environments. Because the performance of MEMS devices is strongly influenced by the dynamic characteristics of its internal microstructures, studying the dynamic characteristics of microstructures under high-temperature environments is urgently needed.

The temperature coefficient of natural frequency (TCF) is an important parameter for MEMS design. Based on the TCF, the variation tendency of resonant frequencies for microstructures can be predicted when the temperature changes. Many researchers have studied the TCFs of basic MEMS microstructures. Sandberg, et al. tested the TCF of the first five modes of SiO_2 microcantilevers under the temperature ranging from 303 K to 353 K. They found that the TCF of the uncoated SiO_2 microcantilever is a constant of ca. 9.79 E-5 K^{-1} [3]. However, the TCF of the gold-coated SiO_2 microcantilever is highly irregular for different modes. Boyd, et al. studied the TCFs of single crystal silicon microcantilevers and 3C silicon carbide microcantilever at temperatures ranging from 200 K to 273 K, respectively. They found that the TCF of single crystal silicon microcantilevers is about −2.47 E-5 K^{-1}, and the TCF of 3C silicon carbide microcantilevers is about −1.8 E-5 K^{-1} [4]. Chuang tested the T-shaped silicon nitride microcantilevers under a cryogenic temperature environment. They found that there was a slight decrease in the resonance frequency when the temperature was elevated from 30 K to 298 K. The TCF of the T-shaped silicon nitride microcantilevers are –5.65 E-5 K^{-1} [5]. It can be seen that there are great differences in TCF for different materials.

To obtain the TCFs of microstructures experimentally, a dynamic testing system with a temperature loading unit is needed. For the last three decades, much effort has been made on developing methods and techniques for the dynamic testing of microstructures. The dynamic testing techniques for microstructures mainly include the vibration measurement techniques and the excitation methods. Because the microstructures have the features of small size, light weight, and high natural frequency, conventional measurement methods cannot be applied without modification. So far, the vibration measurement techniques for microstructures can be divided into two types: built-in self-test (BIST) methods and non-contact optical methods. The BIST

*Corr. Author's Address: Bohai University, No. 19, Keji Road, Jinzhou, China, mems-sds@163.com

methods need to integrate the embedded sensing elements, such as piezoresistive elements [6] and capacitive elements [7], into the microstructures. The non-contact optical methods, such as laser Doppler vibrometer (LDV) [8], stroboscopy and interferometry technique [9] and electronic speckle pattern interferometry (ESPI) [10], have several advantages over the BIST methods. Since there are no additional elements needed, the dynamic characteristics of the original microstructures will not be modified. In particular, laser Doppler vibrometer is widely used in out-of-surface vibration measurement due to its high accuracy. Regarding excitation methods, there are three categories: excitation method with embedded elements [11] to [13], non-contact excitation method [14] to [16] and base excitation method with a bulk piezoelectric ceramic transducer (PZT) [17] and [18]. Compared to other excitation methods, base excitation with bulk PZT is non-destructive, simple, and suitable for microstructures with high resonant frequency. However, this method cannot be used in high-temperature environments, because the piezoelectric ceramic is non-effective when the temperature is elevated approaching its Curie point.

In this paper, the TCF of single crystal silicon microcantilevers was studied under high temperatures ranging from 299 K to 773 K. A dynamic testing system with a high-temperature loading unit was established. In the system, an impact base excitation device with shock wave was developed to excite the microstructures. A LDV was used to obtain the vibration response signals of microstructures. A silicon microcantilever with uniform rectangular crossing section and a T-shaped silicon microcantilever were fabricated. The TCFs of two microcantilevers were tested, and the results were discussed.

1 METHOD

An impact base excitation method with shock wave was proposed to excite the microcantilevers. In this method, the testing microcantilever is attached on one side of a base structure that is installed on a rigid platform. A plate electrode is attached on the other side of the base structure. A needle electrode is fixed on a feeder. The distance between two electrodes can be changed by adjusting the feeder. Two electrodes are wired to the two poles of a capacitor. A direct current (DC) high voltage supply is used to charge the capacitor. The shock wave can be generated when the distance between two electrodes meets the requirement of electrical discharging. The base structure will be impacted by the action of the shock wave. The microcantilever can be excited by the movement of the base structure.

The laser Doppler vibrometer technique is used to obtain the vibration response signals of microcantilevers. The principle of this method is as follows: when a laser is projected to the surface of a moving object, the Doppler effect will occur. The frequency of the reflected light will be changed. The frequency shift is related to the moving speed of the object, and can be written by:

$$f_D = \frac{2v}{c - v}, \tag{1}$$

where f_D is the frequency shift of the reflected light, c is the speed of the light and v is the moving speed of the object. The moving speed of the object can be obtained if the frequency shift has been measured. Furthermore, the vibration parameters of the object can also be obtained based on its moving speed.

2 TESTING SYSTEM SETUPS

A dynamic testing system was established to measure the dynamic characteristics of microstructures under the high-temperature environment ranging from 299 K to 773 K. In the system, an impact base excitation device with shock wave was developed to excite the microcantilevers. A laser Doppler vibrometer was employed to detect the vibration response signals of the microcantilevers.

2.1 Excitation Device

An excitation device was developed basing on the principle of the impact base excitation method with a shock wave, as is shown in Fig. 1.

Five high voltage capacitors were connected in parallel with each other to provide a high impact voltage power. The capacitance of each capacitor is 0.22 μf. The discharging electrodes were fabricated with Wu-Cu alloy material due to its high-temperature resistance and ablative resistance. A crossing leaf spring was used as the base structure. A straight micrometer was chosen as the feeder to adjust the distance between the two electrodes. A ceramic disc was attached between the crossing leaf spring and the plate electrode for the electrical insulation. For the same purpose, a ceramic tube was installed between the needle electrode and the straight micrometer.

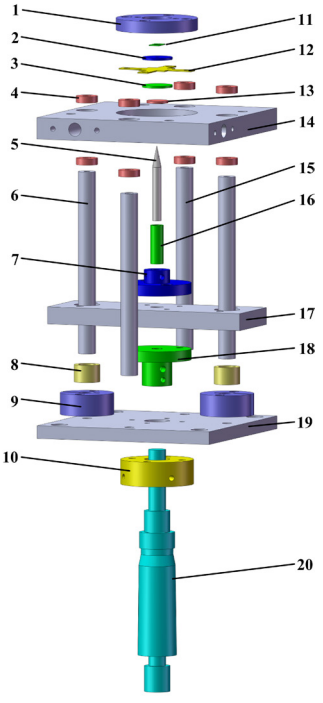

Fig. 1. *Exploded views of excitation device*

2.2 Data Acquisition and Analysis System

A Polytec OFV-534 laser Doppler vibrometer system was employed to measure the dynamic characteristics of microstructures. The system mainly consists of a compact vibrometer sensor head, a CCD camera, a He-Ne laser, an illumination unit, a VDD-E-600 digital front end, a PCI-6110E date acquisition card, and VIBSOFT-VDD vibration measurement software.

The principle of the OFV-534 laser Doppler vibrometer system is as follows: the He-Ne laser emits a 632 nm laser into the compact vibrometer sensor head, in which the laser is split into two laser beams. One is used as the reference laser; the other is used as the incident laser which is irradiated on the testing microcantilever. As soon as the microcantilever vibrates, due to the Doppler effect, the reflected laser contains the frequency signal of the microcantilever. The reflected laser enters the compact vibrometer sensor head in which the reflected laser interferes with the reference laser. Then the interference signal is fed into the VDD-E-600 digital front end, and converted to a standard electrical signal. The obtained standard electrical signal is read through the PCI-6110E data acquisition card, using the VIBSOFT-VDD vibration measurement software. Thus, the vibration response signal of the testing microcantilever is obtained.

As shown in Fig. 2, the compact vibrometer sensor head was mounted on a translation and rotation stage, which contains three translational degrees of freedom and two rotational degrees of freedom. With the aid of the CCD camera and the illumination unit, the laser spot can be positioned on the testing microcantilever easily and precisely by adjusting the translation and rotation stage.

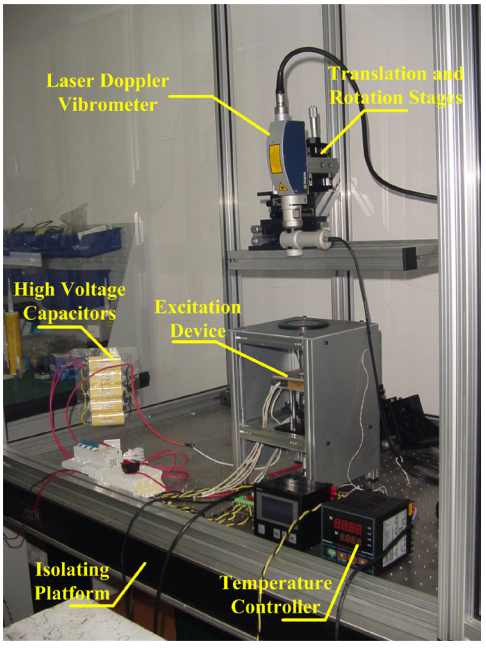

Fig. 2. *Dynamic testing system for microstructures with high-temperature loading unit*

2.3 High-Temperature Environment

Four resistive heaters were installed into the brass block, which can change the temperature of the microcantilever from room temperature 299 K up to 773 K. The heat transferred from the heaters to the testing microcantilever through the brass block and the crossing leaf spring. The excitation device was installed in a protective chamber to decrease the heat loss. Through the quartz glass window on the top of the chamber, the dynamic response of the testing microcantilever can be obtained by the laser Doppler vibrometer.

3 MICROCANTILEVERS

Two single crystal silicon microcantilevers were fabricated and named Microcantilever #1 and Microcantileva #2. Microcantileva #1 is a T-shaped silicon microcantilever, and Microcantileva #2 is a

microcantilever with uniform rectangular crossing section. Their scanning electron microscope (SEM) photographs were shown in Fig. 3.

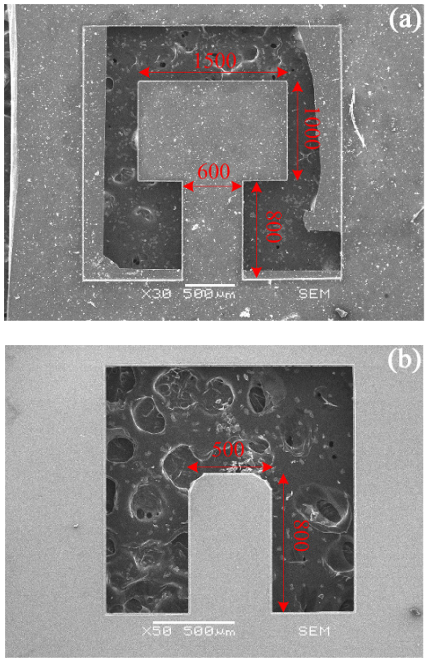

Fig. 3. *SEM photos of microcantilevers. a) #1, b) #2*

The dimensions of Microcantileva #1 are as follows: l_{beam} is the length of the microcantilever beam, which is equal to 800 μm. w_{beam} is the width of the microcantilever beam, which is equal to 600 μm. l_{mass} is the length of the proof mass, which is equal to 1000 μm. w_{mass} is the width of the proof mass, which is equal to 1500 μm. h_1 is the thickness of the microcantilever, which is equal to 10 μm.

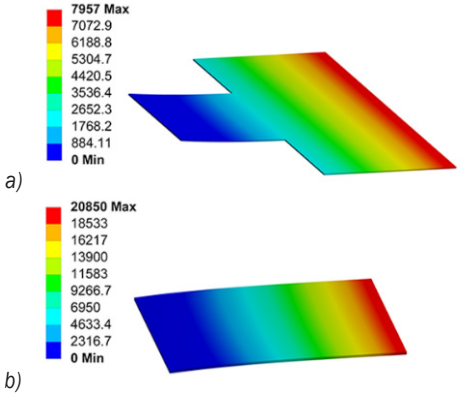

Fig. 4. *Finite element analysis results of natural frequencies at the room temperature. a) #1, b) #2*

The dimensions of Microcantileva #2 are as follows: l is the length of the microcantilever, which is equal to 800 μm. w is the width of the microcantilever, which is equal to 500 μm. h_2 is the thickness of the microcantilever, which is equal to 10 μm.

The first-order natural frequencies of both microcantilevers in 293 K were simulated with ANSYS software. The reference values of material properties of silicon are as follows. The elastic modulus E is equal to 167 GPa. The density **ρ** is equal to 2330 kg/m³. Poisson's ratio is equal to 0.278 [19]. The results are shown in Fig. 4. It is 2.7995 kHz for Microcantileva #1, and 21.988 kHz for Microcantileva #2.

4 EXPERIMENTS AND DISCUSSION

4.1 Natural Frequency at Room Temperature

Two microcantilevers were tested with the developed dynamic testing system at room temperature. The obtained vibration response signals are shown in Figs. 5 and 6, respectively. Applying FFT to these signals, the frequency domain signals were obtained, as shown in Figs. 7 and 8, respectively.

In Fig. 7, there are two distinct peaks at 2.692 kHz and 45.632 kHz. In Fig. 8, there are two distinct peaks at 20.712 kHz and 45.649 kHz. According to the finite element analysis (FEA) results of two microcantilevers in Section 3, it can be inferred that the first-order resonant frequency of Microcantileva #1 is 2.692 kHz, and the first-order resonant frequency of Microcantileva #2 is 20.712 kHz. The common frequency peak, 45.6 kHz, may be the resonant frequency of the base structure or the resonant frequency of the substrate of the silicon chip. The first-order resonant frequencies of the microcantilevers can be considered to be approximately equal to their first-order natural frequencies because the air damping is negligible compared with the structural damping.

There are some differences between the obtained natural frequencies and the FEA results. The following reasons may cause the differences. Firstly, the material properties, such as elastic modulus, density, and Poisson's ratio, will be changed by the fabrication process of silicon microcantilevers. Thus, the actual values of silicon material parameters are different from the selected values in FEA. Secondly, the actual boundary conditions of microcantilevers are different from the ideal conditions. Thirdly, the dimensions of microcantilevers are different from the theoretical values, such as the length, the width, the thickness and the shape of the crossing section. Finally, the measurement error is another affecting factor.

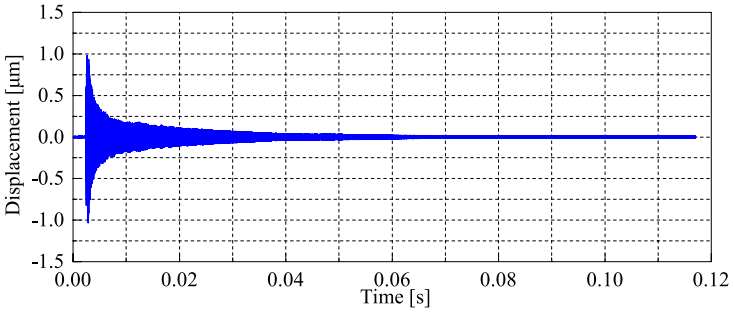

Fig. 5. *Vibration response signal of Microcantileva #1*

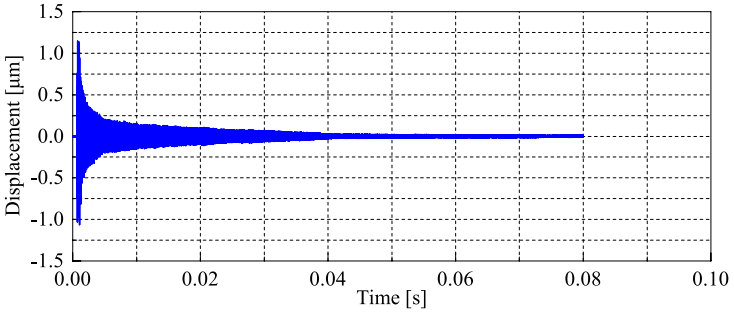

Fig. 6. *Vibration response signal of Microcantileva #2*

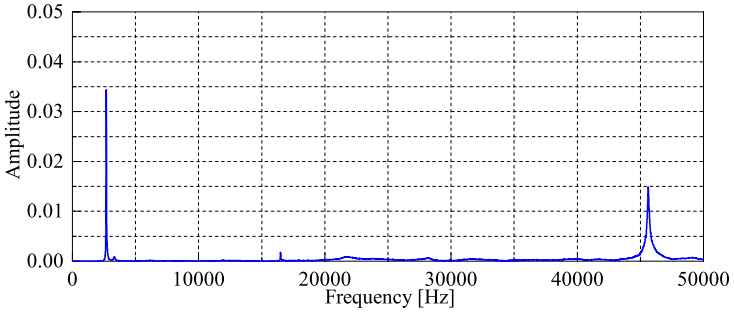

Fig. 7. *Frequency spectrogram of Microcantileva #1*

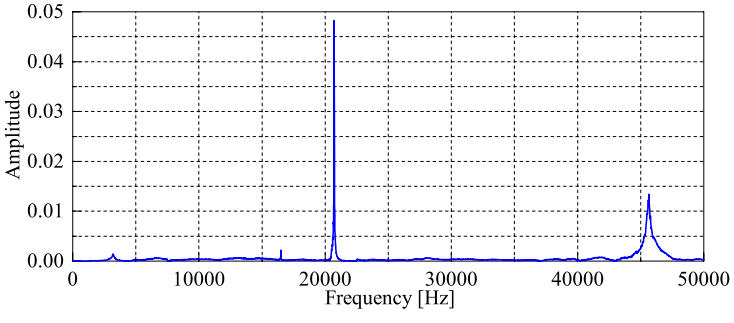

Fig. 8. *Frequency spectrogram of Microcantileva #2*

4.2 Natural Frequency versus Temperature

The dynamic testing experiment was carried out under a high-temperature environment ranging from room temperature to 773 K, and the results are shown in Figs. 9 and 10.

It can be seen that for both microcantilevers, their first-order natural frequencies slightly decrease

with the elevated temperature. Furthermore, there is an almost linear dependence between the first-order natural frequency and the temperature. The rate of change is about –0.069 Hz/K for Microcantileva #1, and –0.51 Hz/K for Microcantileva #2.

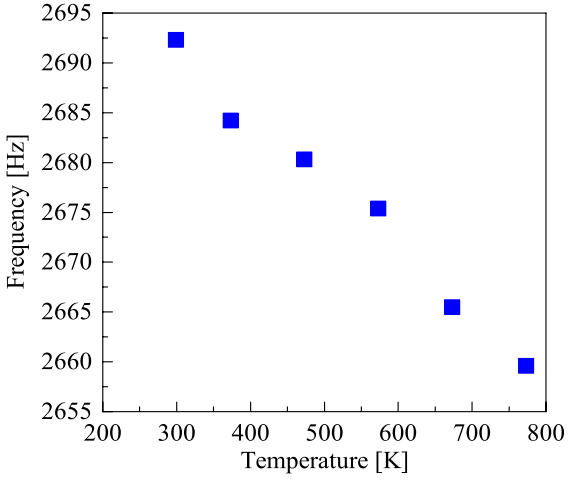

Fig. 9. *The first-order natural frequency of Microcantileva #1 at the different testing temperature*

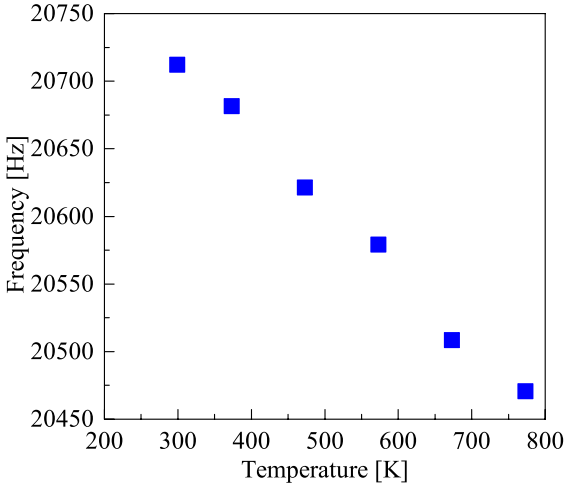

Fig. 10. *The first-order natural frequency of Microcantileva #2 at the different testing temperature*

To determine the TCFs of microcantilevers, the normalized natural frequencies of two microcantilevers were calculated and are shown in Fig. 11. For each microcantilever, its TCF is the slope of the corresponding linear fitting line. It can be seen that the two microcantilevers almost have the same TCF. The obtained TCF is –2.56 E-5 K^{-1} for Microcantileva #1, and –2.46 E-5 K^{-1} for Microcantileva #2. They are very close to the value reported in reference **[11]**. To figure out why both two different shaped microcantilevers have the same TCF, the theoretical TCFs for both microcantilevers were analysed as follows.

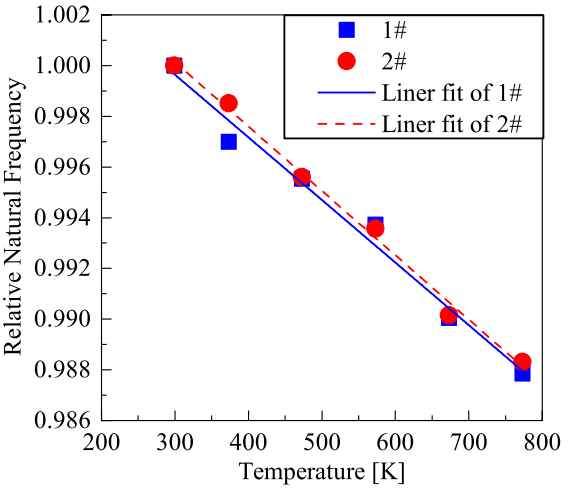

Fig. 11. *Normalized natural frequencies of microcantilevers as functions of temperature*

Generally, the TCF can be determined by:

$$TCF = \frac{1}{f(T_0)} \cdot \frac{\partial f(T)}{\partial T}, \tag{2}$$

where T_0 is the starting temperature, $f(T_0)$ means the reference natural frequency.

For the microcantileva #1, its first-order natural frequency can be expressed as **[20]**:

$$f_1 = \frac{1}{2\pi}\sqrt{\frac{3EI_1}{L^3(m_{mass} + cm_{beam})}}, \tag{3}$$

where f_1 is the first-order natural frequency, E is the elastic modulus, m_{mass} is the proof mass, m_{beam} is the mass of microcantilever beam, c is a constant that is equal to 0.2357 **[21]**, L is the effective length of the T-shaped microcantilever, and I_1 is the area moment of inertia. L and I can be determined by Eqs. (4) and (5), respectively.

$$L = l_{beam} + \frac{1}{2}l_{mass}, \tag{4}$$

$$I_1 = \frac{1}{12}w_{beam}h_1^3. \tag{5}$$

Inserting Eqs. (4) and (5) into Eq. (3), and then introducing the temperature variable T into Eq. (1), the first-order natural frequency of Microcantileva #1 can be written as:

$$f_1(T) = k_1 \cdot E(T)^{\frac{1}{2}} \cdot w_{beam}(T)^{\frac{1}{2}} \cdot h_1(T)^{\frac{3}{2}} \cdot \cdot \left(l_{beam}(T) + \frac{1}{2} l_{mass}(T) \right)^{-\frac{3}{2}}. \quad (6)$$

In Eq. (6), k_1 is a temperature-independent constant, which can be expressed as:

$$k_1 = \frac{1}{4\pi \sqrt{c m_{beam} + m_{mass}}}. \quad (7)$$

Differentiating Eq.(6) with respect to the temperature and dividing by Eq.(6), then inserting T_0 to the results, the TCF of the T-shaped microcantilever can be obtained.

$$TCF = -\frac{3}{2} \cdot \frac{l_{beam}(T)}{l_{beam}(T) + l_{mass}(T)/2} \cdot \alpha_L - -\frac{3}{4} \frac{l_{mass}(T)}{l_{beam}(T) + l_{mass}(T)/2} \cdot \alpha_L + +\frac{3}{2} \cdot \alpha_h + \frac{1}{2} \cdot \alpha_w + \frac{1}{2} \cdot \beta, \quad (8)$$

where α_L is the linear thermal expansion coefficient in the length direction, α_h is the linear thermal expansion coefficient in the height direction, α_w is the linear thermal expansion coefficient in the width direction, β is the temperature coefficient of the elastic modulus. Thus, the TCF of the T-shaped microcantilever can be simplified as:

$$TCF = -\frac{3}{2}\alpha_L + \frac{3}{2}\alpha_h + \frac{1}{2}\alpha_w + \frac{1}{2}\beta. \quad (9)$$

For the microcantileva #2, its first-order natural frequency can be expressed as **[20]**:

$$f_2 = \frac{3.515}{2\pi} \sqrt{\frac{EI_2}{ml^3}}, \quad (10)$$

where m is the mass of the microcantilever, I_2 is the area moment of inertia. I_2 can be determined by the Eq. (11).

$$I_2 = \frac{1}{12} w h_2^3. \quad (11)$$

By introducing the temperature variable T into Eq. (10), the first-order natural frequency of Microcantileva #2 can be written as:

$$f_2(T) = k_2 \cdot E(T)^{\frac{1}{2}} \cdot w(T)^{\frac{1}{2}} \cdot h_2(T)^{\frac{3}{2}} \cdot l(T)^{-\frac{3}{2}}. \quad (12)$$

In Eq. (12), k_2 is a temperature-independent constant, which can be expressed as:

$$k_2 = \frac{3.515}{4\pi\sqrt{3m}}. \quad (13)$$

Using a similar method as for Microcantilever 1#, the TCF of Microcantileva #2 can be obtained.

$$TCF = -\frac{3}{2}\alpha_l + \frac{3}{2}\alpha_h + \frac{1}{2}\alpha_w + \frac{1}{2}\beta, \quad (14)$$

where α_l is the linear thermal expansion coefficient in the length direction.

It can be seen that for both the T-shaped microcantilever and microcantilever with a uniform rectangular crossing section, the TCF is only decided by the temperature coefficient of the elastic modulus and the linear thermal expansion coefficients. Both microcantilevers were fabricated using a 220 μm thick, [100] oriented, single crystal silicon wafer. The length directions of the microcantilevers were all along the [110] crystal orientation. Thus, the same TCF can be obtained.

According to Eq. (10), the first-order natural frequency of Microcantileva #2 can also be expressed as:

$$f_2 = \frac{3.515}{2\pi\sqrt{12}} \cdot \frac{h}{l^2} \cdot \sqrt{\frac{E}{\rho}}, \quad (15)$$

where ρ is the density of the microcantilever. By introducing the temperature variable T into Eq.(15), the first-order natural frequency of Microcantileva #2 can also be written as:

$$f_2(T) = k_3 \cdot E(T)^{\frac{1}{2}} \cdot h(T) \cdot l(T)^{-2} \cdot \rho(T)^{-\frac{1}{2}}. \quad (16)$$

In Eq. (16), k_3 is a temperature-independent constant, which is approximately equal to 0.162. Differentiating Eq. (16) with respect to the temperature and dividing by Eq. (16), then inserting T_0 to the results, the TCF of Microcantilever 2# can be obtained.

$$TCF = -2\alpha_l + \alpha_h + \frac{1}{2}\beta - \frac{1}{2}\delta, \quad (17)$$

where δ is the temperature coefficient of density. As for the single crystal silicon material, its temperature coefficient of elastic modulus is about $-5.2\,\text{E-}5\,\text{K}^{-1}$ **[22]** and **[23]**, and its temperature coefficient of density is about $-1.3\,\text{E-}5\,\text{K}^{-1}$ **[24]**. The linear thermal expansion coefficient in the [110] crystal orientation, α_l, is almost equal to the linear thermal expansion coefficient α_h in the [100] crystal orientation **[25]**. Moreover, they increase with the elevated temperature. The linear thermal expansion coefficient in the length direction or in the height direction is $2.57\,\text{E-}6\,\text{K}^{-1}$ in

293 K, and 4.14 E-6 K^{-1} in 800 K. Thus, according to the Eqs. (9), (14) and (17), the theoretical TCF of both two microcantilevers is about between −2.207 E-5 K^{-1} and −2.364 E-5 K^{-1}. The experimental results are very close to the theoretical values.

5 CONCLUSION

The dynamic testing system for MEMS microstructures was developed, and the TCF of two single crystal silicon microcantilevers was tested. The impact base excitation method with shock wave was proved to be effective for the dynamic measurement of microstructures under the high-temperature environment. The experimental results show that under the high-temperature environment, the first-order natural frequencies of silicon microcantilevers slightly and linearly decrease with the elevated temperature. The variation is induced by the changes in the elastic modulus and physical dimensions. Both the T-shaped microcantilever and the microcantilever with a uniform rectangular crossing section almost have the same TCF. The experimental result is very close to the theoretical analysis.

6 ACKNOWLEDGEMENT

This work was supported by the National Natural Science Foundation of China (Grant no. 51305191) and the General Project of Liaoning Provincial Education Department of China (grant no. L2015009).

7 REFERENCES

[1] Robert, B. (2004). Recent developments in MEMS sensors: A review of applications, markets and technologies. *Sensor Review*, vol. 33, no. 4, p. 300-304, **DOI:10.1108/SR-05-2013-678**.

[2] Michael, K., White, N. (eds.) (2013). *MEMS for Automotive and Aerospace Applications*. Elsevier, Oxford.

[3] Sandberg, R., Svendsen, W., Mølhave, K., Boisen, A. (2005). Temperature and pressure dependence of resonance in multi-layer microcantilevers. *Journal of Micromechanics and Microengineering*, vol. 15, no. 8, p. 1454-1458, **DOI:10.1088/0960-1317/15/8/011**.

[4] Boyd, E.J., Li, L., Blue, R., Uttamchandani, D. (2013). Measurement of the temperature coefficient of Young's modulus of single crystal silicon and 3C silicon carbide below 273K using micro-cantilevers. *Sensors and Actuators A: Physical*, vol. 198, p. 75-80, **DOI:10.1016/j.sna.2013.04.032**.

[5] Chuang, W., Luger, T., Fettig, R., Ghodssi, R. (2004). Mechanical property characterization of LPCVD silicon nitride thin films at cryogenic temperatures. *Journal ofMicroelectromechanical Systems*, vol. 13, no. 5, p. 870-879, **DOI:10.1109/JMEMS.2004.836815**.

[6] Partridge A., Reynolds J.K., Chui B.W., Chow, E.M, Fitzgerald, A.M., Zhang, L., Malus, N.I., Kenny, T.W. (2000) A high-performance planar piezoresistive accelerometer. *Journal of Microelectromechanical System*, vol. 9, no. 1, p. 58-66, **DOI:10.1109/84.825778**.

[7] Xiong, X., Wu, Y.-L. D., Jone, W.-B. (2005). A dual-mode built-in self-test technique for capacitive MEMS devices. *IEEE Transactions on Instrumentation and Measurement*, vol. 54, no. 5, p. 1739-1750, **DOI:10.1109/TIM.2005.855094**.

[8] Burdess, J.S., Harris, A.J., Wood, D., Pitcher, R.J., Glennie, D. (1997). A system for the dynamic characterization of microstructures. *Journal of Microelectromechanical Systems*, vol. 6, no. 4, p. 322-328, **DOI:10.1109/84.650129**.

[9] Hart, M.R., Conant, R.A., Lau, K.Y., Muller, R.S. (2000). Stroboscopic interferometer system for dynamic MEMS characterization. *Journal of Microelectromechanical Systems*, vol. 9, no. 4, p. 409-418, **DOI:10.1109/84.896761**.

[10] Flynn, E.B., Bassman, L.C., Smith, T.P., Lalji, Z., Fullerton, L.H., Leung, T.C., Greenfield, S.R. Koskelo, A.C. (2006). Three-wavelength electronic speckle pattern interferometry with the Fourier-transform method for simultaneous measurement of microstructure-scale deformations in three dimensions. *Applied Optics*, vol. 45, no. 14, p. 3218-3225, **DOI:10.1364/AO.45.003218**.

[11] Kim, P., Bae, S., Seok, J. (2012). Resonant behaviors of a nonlinear cantilever beam with tip mass subject to an axial force and electrostatic excitation. *International Journal of Mechanical Sciences*, vol. 64, no. 1, p. 232-257, **DOI:10.1016/j.ijmecsci.2012.06.008**.

[12] Littrell, R., Grosh, K. (2012). Modeling and characterization of cantilever-based MEMS piezoelectric sensors and actuators. *Journal of Microelectromechanical Systems*, vol. 21, no. 2, p. 406-413, **DOI:10.1109/JMEMS.2011.2174419**.

[13] Wu, C.-T., Hsu, W. (2002). An electro-thermally driven microactuator with two dimensional motion. *Microsystem Technologies*, vol. 8, no. 1, p. 47-50, **DOI:10.1007/s00542-001-0129-7**.

[14] Xiong, L., Zhou, Q., Wu, Y., Chen, P. (2015). New laser excitation method for modal analysis of microstructure. *Mechanical Systems and Signal Processing*, vol. 50-51, p. 227-234, **DOI:10.1016/j.ymssp.2014.05.012**.

[15] Huber, T., Hagemeyer, S., Ofstad, E., Fatemi, M., Kinnick, R., Greenleaf, J. (2007). Noncontact modal excitation of small structures using ultrasound radiation force. *Proceedings of the SEM Annual Conference and Exposition on Experimental and Applied Mechanics*, p. 604-610.

[16] Ricci, J., Cetinkaya, C. (2007). Air-coupled acoustic method for testing and evaluation of microscale structures. *Review of Scientific Instruments*, vol. 78, no. 5, p. 005105, **DOI:10.1063/1.2735574**.

[17] Wang, X.D., Li, N., Wang, T., Liu, M.W., Wang, L.D. (2007). Dynamic characteristic testing for MEMS micro-devices with base excitation. *Measurement Science and Technology*, vol. 18, no. 6, p. 1740-1747, **DOI:10.1088/0957-0233/18/6/s12**.

[18] Burak Ozdoganlar, O., Hansche, B.D., Carne, T.G. (2005). Experimental modal analysis for microelectromechanicalsystems. *Experimental Mechanics*, vol. 45, no. 6, p. 498-506, **DOI:10.1007/bf02427903**.

[19] Madou, M.J. (2011). *Fundamentals of Microfabrication and Nanotechnology: Manufacturing Techniques for Microfabrication and Nanotechnology*. CRC Press, Boca Raton.

[20] Pilkey, W. (1994). *Formulas for Stress, Strain, and Structural Matrices*. Wiley, New York.

[21] Young, W.C. (1989). *Roark's Formulas for Stress and Strain*. McGraw-Hill, New York.

[22] Petersen, K.E. (1982). Silicon as a mechanical material. *Proceedings of the IEEE Electron Devices*, vol. 70, no. 5, p. 420-457, **DOI:10.1109/PROC.1982.12331**.

[23] McSkimin, H.J. (1953). Measurement of elastic constants at low temperatures by means of ultrasonic waves–data for silicon and germanium single crystals, and for fused silica. *Journal of Applied Physics*, vol. 24, no. 8, p. 988-997, **DOI:10.1063/1.1721449**.

[24] Soma, T., Kagaya H.M. (1988). *Properties of Silicon, EMIS Data Reviews Series*, no. 4, Wiley, New York.

[25] Watanabe, H., Yamada, N., Okaji, M. (2004). Linear thermal expansion coefficient of silicon from 293 to 1000 K. *International Journal of Thermophysics*, vol. 25, no. 1, p. 221-236, **DOI:10.1023/B:IJOT.0000022336.83719.43**.

Strojniški vestnik - Journal of Mechanical Engineering 62(2016)9, 543-550

DOI:10.5545/sv-jme.2016.3531 Original Scientific Paper
Received for review: 2016-02-26
Received revised form: 2016-05-27
Accepted for publication: 2016-06-07

Volume Flow Characterization of PWM-Controlled Fast-Switching Pneumatic Valves

Miha Pipan* – Niko Herakovič
University of Ljubljana, Faculty of Mechanical Engineering, Slovenia

In this paper we present results of an experimental analysis of the dependence of volume flow on pulse width modulation (PWM) control signal through a fast-switching pneumatic valve. The main goal of this study is to determine how the PWM frequency and duty cycle (pulse width) influence the volume flow and if there is a correlation between them. The highest PWM signal frequencies that can control the tested fast-switching valve were used. This way we minimised the influence of pressure pulsation that can make a pneumatic system, pressure regulator and flow sensor unstable at lower frequencies. The aim was also to determine if pressure difference and PWM frequency have any influence on the shortest pulse needed to open the valve. The volume flow was measured with a state-of-the-art mass flow sensor that can calculate average volume flow and isn't influenced by high-frequency pressure pulsation. We also made temperature measurement in a valve solenoid and pressure chamber during an 8-hour excitation with a PWM signal.
Keywords: fast switching valves, PWM, flow characteristics, pulse width

Highlights
- *The minimum width of PWM pulse needed for a fast-switching valve to open increases with the increase of pressure difference.*
- *The correlation between pulse width and average volume flow of the valve is highly nonlinear with initial steep response at lower pressure differences.*
- *Maximum PWM frequency used to control the fast-switching valve is limited by response time of the valve and also by the maximum number of valve cycles.*
- *Experimental results show that digital PWM control technique can be used effectively with fast-switching valves.*

0 INTRODUCTION

Pneumatic actuators are widely used in industry and are generally used for two position controls. When the continuous position control is required, pneumatic servo or proportional valves are used. Pneumatic servo valves are expensive and proportional valves do not have the fastest response time due to the spool dead band. The alternative is to use fast-switching valves with digital control techniques to achieve linear flow control characteristics with the fastest possible response. The implementation of fast switching valves for position control using digital control techniques has been in development for the last 10 years. The main reason that enables us to use pulse width modulation (PWM) control method is newly developed valves with response times shorter than a few milliseconds. PWM signal is [1] a sequence of short electrical pulses that open a valve for a fraction of time. After each pulse another pulse with the same or different pulse width follows. The change of pulse width achieves different air pressure bursts. The change in number and duration of these pressure bursts modifies the average flow through the fast-switching valve. In this paper we wanted to analyse the influence of different PWM control signals on the average flow characteristics of the fastest switching pneumatic valve that is currently available in the market.

The results will be used for the development of a control algorithm for fast-switching valves that control contraction of pneumatic artificial muscles. This has been done before with switching valves that have shorter switching time of 2 ms [2], 20 ms [3], 2 ms [4] and without taking into account the change of minimum pulse and nonlinear relation between pulse width and air flow. If flow pulsation is in high frequency domain it can be defined as average flow since a pneumatic muscle with a large enough volume acts as a low-pass filter similar to DC motors controlled via PWM [5]. The natural frequency of muscle changes depending on internal pressure and contraction but based on our and other research [6] the natural frequency has values between 9 Hz to 42 Hz. With the use of high PWM frequency we excitate the muscle with pulsation that is in over-critical frequency domain and does not make the pneumatic muscle unstable.

Many researchers used PWM control techniques to drive pneumatic switching valves with good results. The PWM signal frequencies f_{PWM} [Hz] used depend on the valve response time and were between 10 and

*Corr. Author's Address: University of Ljubljana, Faculty of Mechanical Engineering, Askerceva 6, Ljubljana, Slovenia, miha.pipan@fs.uni-lj.si

50 Hz [7], 100 Hz [8], up to 50 Hz [9], 100 Hz [10], 50 Hz [11] and 20 to 60 Hz [12]. Efforts were made to develop electro-pneumatic valve models based on the electrical and pneumatic parts modelling and to use these models in a PWM-driven pneumatic system [8], [9] and [13]. The relationship between the pulse width and the fluid flow was always defined to be linear, and the minimum PWM pulse was used in only one paper, [7] and [14]. The relationship between electrical, magnetic and mechanical components can be modelled with lumped parameter valve model to simulate switching times and to compare results with obtained valve experimental data [15]. An interesting finding was that the closing time of the valve is not only a function of pressure difference but also of magnetic hysteresis, magnet supply voltage and Eddy current. In the latest research, the relationship between the pressure difference and the solenoid current in pneumatic switching valves [16] is considered.

But there were no experimental analyses performed or models developed that would directly describe the influence of the valve pressure difference on the minimum pulse width. The standard equation of the fluid flow through a pneumatic valve is defined in the ISO 6358 standard, Eq. (1) [17], and is used in this form in almost all mathematical models of pneumatic switching valves.

$$\dot{V}_a = \begin{cases} P_1 C \dfrac{T_0}{T_1} \sqrt{1 - \left(\dfrac{\dfrac{P_2}{P_1} - b}{1 - b} \right)^2} & \text{for} \quad \dfrac{P_2}{P_1} > b \\ P_1 C \dfrac{T_0}{T_1} & \text{for} \quad \dfrac{P_2}{P_1} \le b \end{cases}, \quad (1)$$

where $\dot{V}_a$ represents the volume flow [m³/s], P_1 the absolute inlet pressure [Pa], P_2 the absolute outlet pressure [Pa], C the acoustic conductivity [m³/(s·Pa)], T_0 the ambient temperature [K], T_1 the temperature of inlet air [K], and b the critical ratio. The characteristics of the tested valve MHJ10-MF are as follows: $C = 2.6167 \times 10^{-9}$ m³/(s·Pa) and $b = 0.433$. But this model does not describe what happens when the valve is controlled via the PWM signal and when the valve is in constant transit states between being opened and closed. Therefore, this model can only be used when the valve is fully opened. To accurately simulate air flow through a valve in transit state and single switching (probably multiple Eddy flows), a combination of Lumped Parameter Valve Model [15] for determining the spool position as a function of time for a single actuation with additional field simulation for flow rate calculation [18] is needed. Simulation model based on this will be developed in future work and will be compared with experimental data presented in this paper.

Experimental data will also enable verification of a new valve model developed in the future based on a similar simulation model [19], the development of control algorithm for position and force control [20], failure analysis [21] and deformation analysis of controlled pneumatic actuator [22].

In this paper, we present the results of an extensive analysis of the behaviour of fast- switching valves when using different PWM signals and the way the average flow changes. In the first part of the paper the executed test plan with all PWM frequencies, pulse widths and pressure differences is described. Later the experimental setup with all the components is presented. In the last part of the paper results are presented, compared and discussed.

1 METHODS

The Experimental analysis is performed under various pressure differences ΔP [bar], three different frequencies and multiple pulse widths. The tested valve is MHJ10-LF. This valve has an open time t_{on} and close time t_{off} less than 1 ms. The maximum usable frequency is therefore 500 Hz if it takes 1 ms to open the valve and 1 ms to close the valve. But at this frequency we can only open and close the valve without having any influence on the duration in which the valve is opened. Therefore, we chose to test frequencies between 200 Hz and 300 Hz. With these frequencies we were able to control the duration in which the valve is opened and closed while staying as far from the natural frequency of the pneumatic systems as possible. At lower frequencies the long-lasting pressure bursts can cause problems [23] and the controlled pneumatic systems can become unstable since we come closer to pneumatic components' natural frequencies that are between 9 Hz to 42 Hz [6].

The pulse width can be measured in time (t_{pulse} [ms]) or as the percentage of the PWM period width ($t_{pulse\%}$ [%]) called '*duty cycle*'. In Fig. 1 the valve input control PWM signal with the amplitude of 24 V, frequency f_{PWM} = 250 Hz and 25 % duty cycles (pulse widths) and measured average volume flow is shown.

The average flow measurement was taken when measured flow stabilised after 10 seconds of continuous valve control with PWM for single frequency and duty cycles. The 10 seconds are needed because of slow response of the flow sensor.

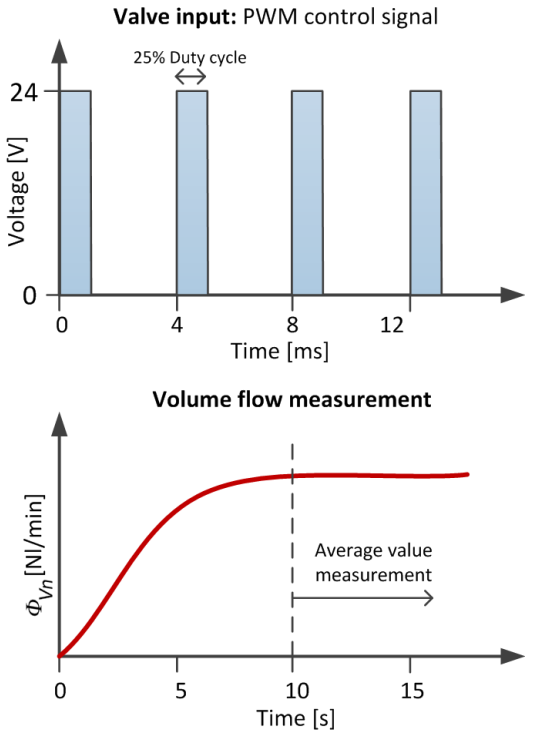

Fig. 1. *Valve input PWM signal and average volume flow measurement*

Different pulse widths were chosen to measure the influence on the average volume flow. The pulse width was changed in steps of 1 % for the range of 0 % to 10 % and with steps of 10 % from 10 % to 100 % of pulse width (duty cycle). Smaller steps of pulses between 0 % and 10 % are needed to accurately measure how the average volume flow changes when the valve is just beginning to open. The minimum pulse width $t_{min\%}$ [%] when the air mass flow sensor detects the flow is set with the accuracy of 0.1 %. Maximum pulse that still has an influence on volume flow $t_{max\%}$ is set with the same accuracy. The executed experimental analysis plan with all used frequencies, pressure differences and pulse widths is shown in Table 1.

Table 1. *Fast switching valve PWM test plan*

f_{PWM} [Hz]	ΔP [bar]	$t_{pulse\%}$ 0 to 10 [%]	$t_{pulse\%}$ 10 to 90 [%]	$t_{min\%}$ [%]	$t_{max\%}$ [%]
200 250 300	0.10 0.30 0.50 1.00 2.00 3.00 4.00 5.00 6.00	1 % step	10 % step	manual with 0.1 % step	manual with 0.1 % step

Experimental analysis was performed for every frequency using the following steps:

1. Set the PWM frequency, f_{PWM}.
2. Set the desired pressure difference, ΔP, with the pressure regulator and fine tune it using the pressure sensor for reference.
3. Increase the PWM pulse, $t_{pulse\%}$, until the flow is detected to find $t_{min\%}$.
4. Increase the $t_{pulse\%}$ from 0 % to 10 % in 1 % steps and save the measured flow.
5. Increase the $t_{pulse\%}$ from 10 % to 90 % in 10 % steps and save the measured flow.
6. Find the maximum pulse width, $t_{max\%}$ which still has an effect on the flow.
7. Set the new pressure difference, ΔP, and repeat steps 3 to 7.
8. Repeat steps from 1 to 7 for all frequencies, f_{PWM} = 200 Hz, 250 Hz and 300 Hz.

2 EXPERIMENTAL

The dependence of the fluid flow characteristics on the pulse width and frequency needs to be accurately measured. Fig. 2 shows the experimental setup scheme and all electrical and pneumatic components used where: A is air preparation, B is pressure regulator, C is pressure sensor, D is fast-switching valve, E is air mass flow sensor, F is PC with Matlab/Bronkhorst FlowPlot software and G is CX controller with modules for pressure sensor and PWM modulation. The CX controller communicates with the PC via LAN network while mass flow sensor data is gathered on the PC via RS-232.

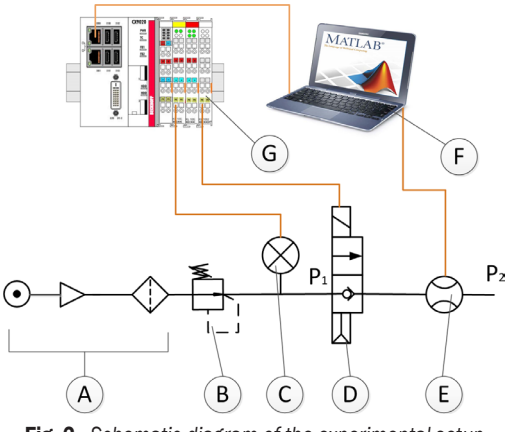

Fig. 2. *Schematic diagram of the experimental setup*

The pressure sensor, the fast-switching valve and the air mass flow sensor are connected via piping with an internal diameter of 4 mm. To avoid air turbulence,

the components must be mounted 100 mm apart, as shown on the experimental setup photography in Fig. 3.

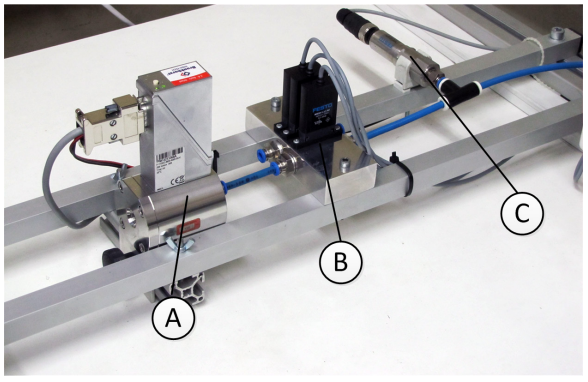

Fig. 3. *Photograph of experimental setup main pneumatic components connected: A is air mass flow sensor, B fast-switching valve, and C pressure sensor*

The most important part of the experimental setup is the air mass flow sensor F-112AC by Bronkhorst. Sensor's measuring range in normal litres per minute is Φ_{Vn} = 1.4 Nl/min to 200 Nl/min with an accuracy of 0.5 % of measured value plus 0.1 % of full-scale [24]. Because of the sensor used and a relatively high PWM frequency, there is no need for special measurement equipment due to pressure pulsation [25]. The average volume flow of pulsation air flow can be measured with thermal anemometers if certain rules are taken into account [26]. First there must be no backflow. Since the inlet pressure is always higher at the valve outlet and there is no nozzle at the F-112AC outlet port, the backflow should not occur. F-112AC has two combined windings for heating and temperature measurement mounted on the capillary tube bypass [24]. The mass of the capillary tube with winding and housing, where the temperature drop is measured, is much greater than in hot-wire sensors. Air flow pulses with high frequency are damped since the mass temperature cannot change with same frequency. To get the average value of the air flow, the FlowPlot acquisition software sensor's exponential smoothing filter was set to slow the response [27]. The response time of F-112AC $t_{63\%}$ is 2 to 4 seconds, therefore the measurement for every pulse width will be at a minimum 10 seconds to achieve accurate measurement.

The tested valve, MHJ10-MF, is the fastest switching valve from Festo with the following specifications: nominal flow rate of Φ_V = 100 l/min, response time for opening t_{on} = 0.7 ms, closing time t_{off} = 0.5 ms at pressure difference ΔP = 0.1 bar, and t_{on} = 0.9 ms, closing time t_{off} = 0.4 ms at ΔP = 6 bar [28]. The opening time, t_{on}, increases and the closing time, t_{off}, decreases with the increase of the pressure difference due to the internal structure of the valve. The valve is normally closed due to pressure forces acting on the spool. The increased pressure difference increases the necessary electromagnetic force to open the valve and also closes the valve more rapidly. The internal structure schematics of the fast-switching pneumatic valve is presented in Fig. 4, where A is the solenoid, B is the air gaps that enable air pressure to close the valve, C is the metallic control spool, D is the valve inlet, E is the metering edge and F is the valve outlet.

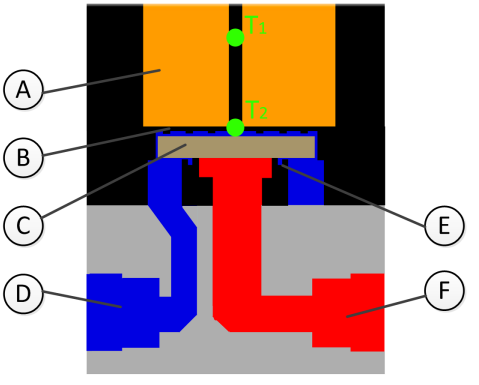

Fig. 4. *Schematics of the fast switching valve internal components*

T_1 and T_2 are positions of holes made on the valve housing 1.6 mm deep where we measured temperature during continuous excitation with PWM signal of 250 Hz and 50 % duty cycle.

The pressure difference is set with the help of the pressure regulator and the pressure sensor positioned before the valve. Measurement uncertainty is calculated using the sensor and an A/D converter with specifications shown in Table 2.

Table 2. *Measurement uncertainty*

Measurement element		Uncertainty	Uncertainty [% FS]
ΔP	Pressure sensor SDET-22T	Repeatability	0.25
		Linearity	0.4
		Temperature	0.15
	A/D converter EL3104	Repeatability	0.3
		Res. 16 bit	0.00385
	Pressure measurement	Combined Uncertainty	0.62916
Φ_V	Volume flow sensor F-112AC	Repeatability	0.5 % measured value + 0.1 % FS
	Volume flow measurement	Combined Uncertainty	0.5 % M.V. value + 0.1 % FS
T	EasyCal 315	Accuracy	±1.1 °C

From the calculation we can conclude with 95 % certainty that the measured pressure difference ΔP is in the range of ±0.0503 bar and volume flow Φ_{Vn} is in the range from ±0.207 Nl/min at flowrate 1.4 Nl/min to ±1.2 Nl/min at flowrate 200 Nl/min.

2.1 Experimental Results

All gathered data is available in Matlab data matrices for further analysis. The pulse width, $t_{pulse[\%]}$ [%], was converted to time, t_{pulse} [ms] for better compatibility between frequencies. Fig. 5 presents the results for the measured flow at $\Delta P = 6$ bar, Fig. 6 for $\Delta P = 3$ bar and Fig. 7 for $\Delta P = 0.1$ bar.

At the pressure difference of $\Delta P = 6$ bar, the relation between pulse width and flow is almost linear. The maximum flow is reached at different pulse width as a function of PWM period and is defined by the PWM frequency period. Therefore the maximum flow for $f_{PWM} = 200$ Hz is reached with pulse a width around $t_{pulse} = 5$ ms, for $f_{PWM} = 250$ Hz in 4 ms and $f_{PWM} = 300$ Hz in 3.33 ms.

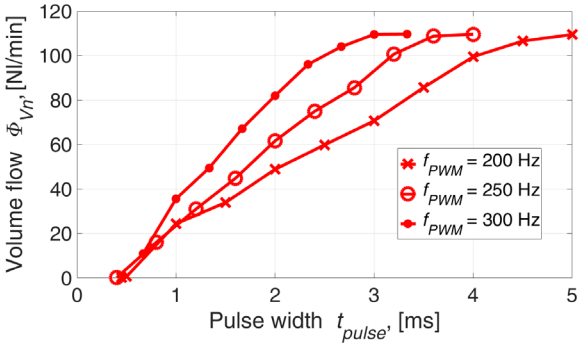

Fig. 5. *Comparison of test results for pressure difference $\Delta P = 6$ bar and different PWM frequencies*

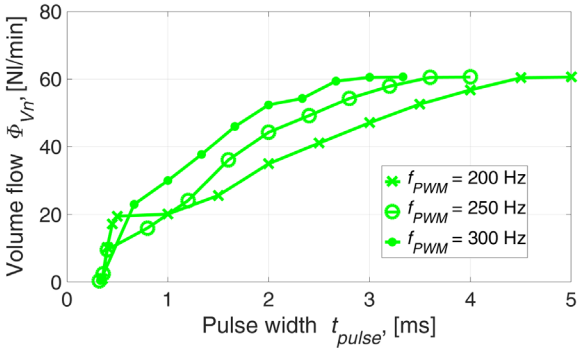

Fig. 6. *Comparison of test results for the pressure difference $\Delta P = 3$ bar and different PWM frequencies*

As the pressure difference drops, the relationship between valve control signal pulse widths and volume flow becomes nonlinear. This is most prominent at lower frequencies when the valve starts to open. The volume flow has a steeper slope in the beginning and later becomes flatter.

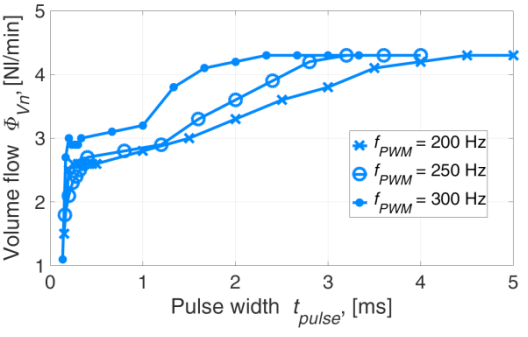

Fig. 7. *Comparison of test results for the pressure difference $\Delta P = 0.1$ bar and different PWM frequencies*

At the lowest pressure difference, the flow increases almost vertically when the valve starts to open. Also at $f_{PWM} = 200$ Hz the relation between the pulse width and the volume flow is not linear even at the initial steep response.

The minimum pulse t_{min} [ms] increases from 0.14 ms to 0.4 ms and increases with pressure difference. In Fig. 8, the comparison of all three frequencies and different pressure differences is given. There is a slight difference between frequencies in Fig. 8. Since the resolution of $t_{min\%}$ is 0.1 % and the measurement accuracy of the pulse width is ± 0.01 ms. The extended normal distribution of measurements is ± 0.00944 ms. which means, that differences between all the three frequencies is within 95 % certainty (Table 1) of the measurement error domain and is not a function of different PWM frequencies.

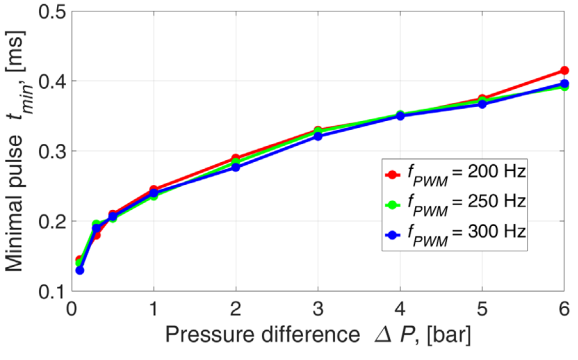

Fig. 8. *Minimum PWM pulse tmin as a function of ΔP*

The widest pulse that still has an effect on the volume flow characteristics t_{max} [ms] is the function of frequency because the frequency determines the period of the pulse. Experimental results of the maximum pulse width are presented in Fig. 9.

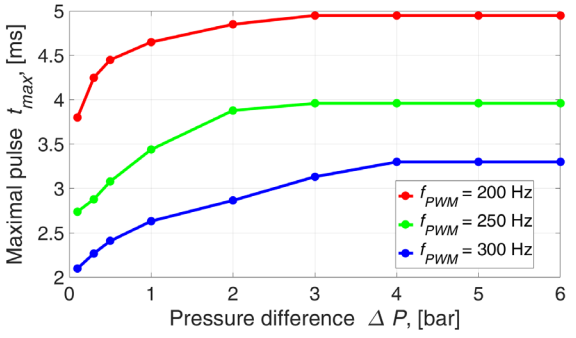

Fig. 9. *Maximum PWM pulse tmax as a function of* ΔP

To choose the best of three tested frequencies, the comparison of flow characteristics and pulse widths for three pressure differences is necessary.

Presented data shows that there are differences between frequencies but it is hard to see clearly which one has the smoothest transition for lower pressure differences. To choose the optimal PWM frequency, all the data is normalized. This is done by converting the mass air flow data to volume flow as percentage at a given pressure difference. Also pulse widths are converted from milliseconds to percentages. In Fig. 10, the comparison of all three different frequencies at three differential pressures is shown.

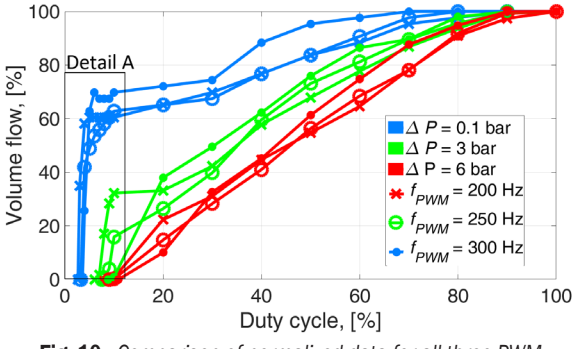

Fig. 10. *Comparison of normalized data for all three PWM frequencies and three pressure differences*

It is obvious that at lower pressure differences the flow through the valve has a very steep curve which normalizes at about 10 % or 0.5 ms of the pulse width and then progresses relatively linearly. At higher pressure differences, the characteristics are almost linear. To achieve the best control of the volume flow through the valve using fast pneumatic valves and PWM, it is crucial to have smooth characteristics at lower pressure differences as well. The smoothest transition from the closed valve to the first 10 % (0.5 ms) of the PWM duty cycle was found for the frequency f_{PWM} = 250 Hz as shown in detail A of Figs. 10 in 11. Higher frequencies decrease the life span and the control resolution of the valve.

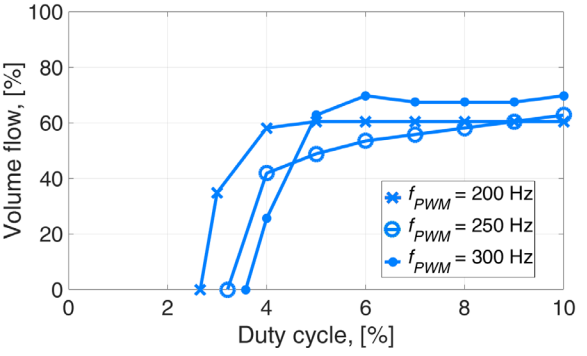

Fig. 11. *Detail A of Fig. 10: PWM frequency comparison for* ΔP *= 0.1 bar*

Experimental results show that with faster response of fast-switching valves higher PWM frequencies can be used. The maximum tested frequency so far was 100 Hz. With even higher PWM frequencies we get further away from natural frequencies of pneumatic components and achieve more stable control and faster responses.

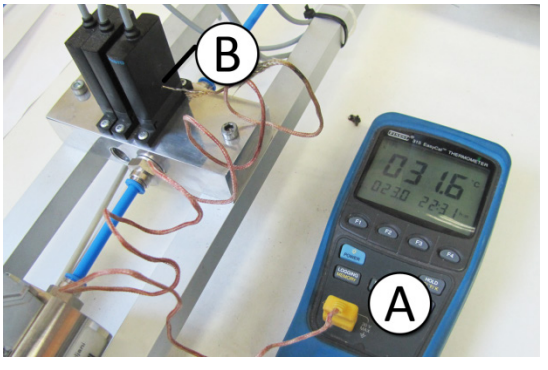

Fig. 12. *Temperature measurement of* T_1 *during temperature testing of Festo valve (A is a digital thermometer EasyCal 315, and B Festo valve with thermocouple inserted in position* T_1

Measurement of the temperatures T_1 (measured in a hole made in the valve housing between 2 solenoids) and T_2 (measured in a hole made on the bottom of two solenoids) was made for duration of 8 hours using a digital thermometer EasyCal 315 with thermocouple. The ambient air temperature was 24.2

°C. The measurement was taken automatically every minute. Measurement during temperature T_1 test is shown on Fig. 12. Fig. 13 shows temperatures T_1 and T_2 during the 8 hour testing of the Festo Valve with the PWM frequency f_{PWM} = 300 Hz and duty cycle of 50 %. The solenoid temperature T_1 becomes stable at approximately 70 °C and T_2 at 28 °C. Both temperatures are below maximum temperature defined by the manufacturer (T_{1max} = 155 °C and T_{2max} = 60 °C) [28]. The temperature T_1 increases due to the heating of the solenoid and heat is mainly transferred through valve housing into ambient air. T_2 is also heated with solenoid but the majority of the heat is transferred via constant air flow through the valve.

Valve temperature T_1 and T_2 achieves its maximum value after approximately 10 minutes as shown in Fig 14.

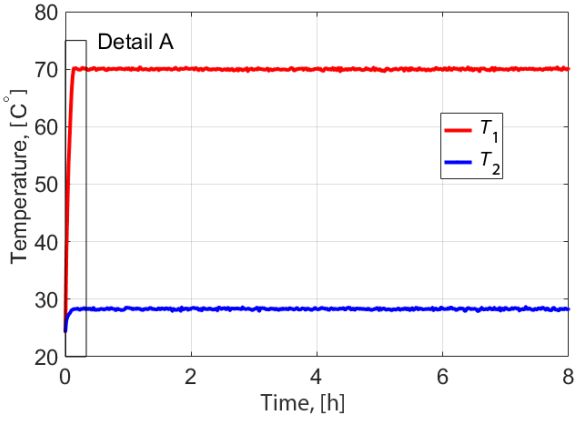

Fig. 13. *Change of valve temperature T_1 and T_2*

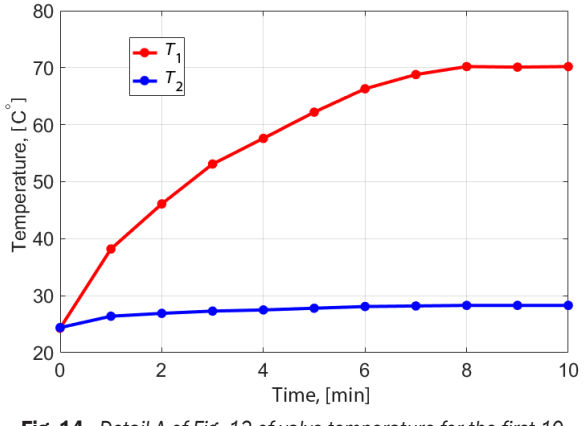

Fig. 14. *Detail A of Fig. 13 of valve temperature for the first 10 minutes*

4 CONCLUSIONS

In this paper, we presented an experimental analysis of flow characteristics of fast-switching valve controlled via different PWM signals. We tested the effects of different frequencies and pulse widths of PWM signals at various pressure differences on volume flow through the fast-switching valve. Experiments clearly show that minimal pulse width needed to open the valve increases with the incensement of pressure difference from 0.14 ms to 0.4 ms. This is the result of air pressure forcing the spool into the closed position and therefore electromagnetic force needs more time to open the valve.

At lower pressure differences (ΔP < 1 bar), when the valve is just starting to open, the volume flow increases almost vertically. This is due to the unstable dynamic equilibrium of low pressure forces that are controlled by stronger pulses of electromagnetic forces.

At pressure differences higher than 1 bar, the correlation between PWM duty cycle and volume flow becomes almost linear and does not have initial vertical responses.

The frequency f_{PWM} = 250 Hz is the most stable and has the most continuous transition at lower pressures. It is 5 times higher than the natural frequency of standard pneumatic components. Considering the calculation that the valve lifespan is 5 billion of switching cycles, the valve could work continuously for 243 days.

Experimental results will be used to develop a new control algorithm that will be able to continuously control volume flow via PWM control signals and fast-switching pneumatic valves. To achieve short response time and linear volume flow control, the smart algorithm must be based on the following conditions:

1. The pressure difference must be measured or calculated so that the control algorithm can calculate the best solution for the given system state.
2. The control algorithm must define the minimal PWM pulse as a function of the pressure difference. This way the shortest response time that mimics the characteristics of pneumatic servo valve can be achieved.
3. Depending on the pressure difference and the desired volume flow, the pulse width must be calculated.
4. The PWM frequency will be 250 Hz.

The new control algorithm will be based on mathematically modelled experimental data to accurately describe the correlation between the pulse width and the desired valve opening. Valve temperature measurement showed that the temperature does not exceed maximum allowed valve temperature

when exciting the valve with PWM f_{PWM} = 300 Hz. Therefore, we have proved that the PWM frequency of up to f_{PWM} = 300 Hz can be used without additional cooling. Experimental data will also be used to validate a new Lumped Parameter Model simulation model.

5 REFERENCES

[1] Keski-Honkola, P., Pietola M. (2008). Generating Vibration with Artificial Muscles. Ventil, vol. 14, no. 6, p. 558-564.

[2] Zhu, X., Tao, G., Yao, B., Cao, J. (2009). Adaptive robust posture control of a parallel manipulator driven by pneumatic muscles with redundancy. IEEE Transactions on Mechatronics, vol. 17, no. 3, p. 576–588, **DOI:10.1109/TMECH.2008.2000825**.

[3] Leephakpreeda, T. (2011). Fuzzy logic based PWM control and neural controlled-variable estimation of pneumatic artificial muscle actuators. *Expert System with Application*, vol. 38, no. 6, p. 7837-7850, **DOI:10.1016/j.eswa.2010.12.120**.

[4] Chandrapal, M., Chen, X., Wang, W., Hann, C. (2012). Nonparametric control algorithms for a pneumatic artificial muscle. *Expert Systems with Applications*, vol. 39, no. 10, p. 8636-8644, **DOI:10.1016/j.eswa.2012.01.190**.

[5] Giurgiutiu, V., Lyshevski, S.E. (2009). Microcontrollers for sensing, actuation and process control. Giurgiutiu, V., Lyshevski, S.E. (eds.) *Micromechatronics: Modeling Analysis, and Design with MATLAB*, p. 727–884, CRC Press, Boca Raton, **DOI:10.1201/b15830-13**.

[6] Liptak, B.G. (1999). *Instrument Engineers' Handbook: Process measurement and analysis*, CRC Press, Boca Raton.

[7] Belforte, G., Mauro, S., and Mattiazzo, G. (2004). A method for increasing the dynamic performance of pneumatic servo systems with digital valves. *Mechatronics*, vol. 14, no. 10, p. 1105-1120, **DOI:10.1016/j.mechatronics.2004.06.006**.

[8] Ying, C., Jia-fan, Z., Can-jun, Y., Bin, N. (2007). Design and hybrid control of the pneumatic force-feedback systems for Arm-Exoskeleton by using on/off valve. *Mechatronics*, vol. 17, no. 6, p. 325-335, **DOI:10.1016/j.mechatronics.2007.04.001**.

[9] Topçu, E.E., Yüksel, I., Kamiş, Z. (2006). Development of electro-pneumatic fast switching valve and investigation of its characteristics. *Mechatronics*, vol. 16, no. 6, p. 365–378, **DOI:10.1016/j.mechatronics.2006.01.005**.

[10] Ahn, K., Yokota, S. (2005). Intelligent switching control of pneumatic actuator using on/off solenoid valves. Mechatronics, vol. 15, no. 6, p. 683-702, **DOI:10.1016/j.mechatronics.2005.01.001**.

[11] Taghizadeh, M., Ghaffari, A., Najafi, F. (2009). Improving dynamic performances of PWM-driven servo-pneumatic systems via a novel pneumatic circuit. *ISA Transactions*, vol. 48, no. 4, p. 512-518, **DOI:10.1016/j.isatra.2009.05.001**.

[12] Taghizadeh, M., Ghaffari, A., Najafi, F. (2009). Modeling and identification of a solenoid valve for PWM control applications. *Comptes Rendus Mécanique*, vol. 337, no. 3, p. 131-140, **DOI:10.1016/j.crme.2009.03.009**.

[13] Najjari, B., Barakati, S.M., Mohammadi, A., Futohi, M.J., Bostanian, M. (2014). Position control of an electro-pneumatic system based on PWM technique and FLC. *ISA Transations*, vol. 53, no. 2, p. 647-657, **DOI:10.1016/j.isatra.2013.12.023**.

[14] Wang, Q., Yang, F., Yang, Q., Chen, J., Guan, H. (2011). Experimental analysis of new high-speed powerful digital solenoid valves. *Energy Conversion and Management*, vol. 52, no. 5, p. 2309-2313, **DOI:10.1016/j.enconman.2010.12.032**.

[15] Xiang, Z., Liu, H., Guoliang, T. (2010). Development and investigation of high-speed pneumatic jet valves by lumped parameter modeling. *7th International Fluid Power Conference, Workshop proceedings*, p. 261-271.

[16] Zhang, J., Lv, C., Yue, X., Li, Y., Yuan, Y. (2014). Study on a linear relationship between limited pressure difference and coil current of on/off valve and its influential factors. *ISA Transactions*, vol. 53, no. 1, p. 150-161, **DOI:10.1016/j.isatra.2013.09.008**.

[17] ISO 6358-1:2013. (2013). *Determination of flow-rate characteristics of components using compressible fluids -- Part 1: General rules and test methods for steady-state flow.* International Organization for Standardization, Geneva.

[18] S.-N. Yun, D.-W. Yun, H.-H. Kim (2010). Flow characteristics of the piezoelectric driven pneumatic valve for grain sorter. *7th International Fluid Power Conference, Workshop proceedings*, p. 273-283.

[19] Lovrec, D. Kastrevc, M. (2011). Modelling and simulating a controlled press-brake supply system. *International Journal of Simulation Modelling*, vol. 10, no. 3, p. 133-144, **DOI:10.2507/IJSIMM10(3)3.184**.

[20] Lotz, M., Bruhm, H., Czinki, A. (2014). An new force control strategy improving the force control capabilities of standard industrial robots. *Journal of Mechanics Engineering and Automation*, vol. 4, p. 276-283.

[21] Yuan, L.-W., Li, S.-M., Peng, B, Chen, Y.-M. (2015). Study on failure process of tailing dams based on particle flow theories. *International Journal of Simulation Modelling*, vol. 14, no. 4, p. 658-668, **DOI:10.2507/IJSIMM14(4)8.322**.

[22] Cuesta, E., Mantaras, D.A., Luque, P. Alvarez, B.J. (2015). Dynamic deformations in coordinate measuring arms using virtual simulation. *International Journal of Simulation Modelling*, vol. 14, no. 4, p. 609-620, **DOI:10.2507/IJSIMM14(4)4.311**.

[23] Karadžić, U., Bulatović, V., Bergant, A. (2014). Valve-induced water hammer and column separation in a pipeline apparatus. *Strojniški vestnik - Journal of Mechanical Engineering*, vol. 60, no. 11, p. 742-754, **DOI:10.5545/sv-jme.2014.1882**.

[24] Bronkhorst (2014). *Instruction manual EL-FLOW Base series Mass Flow Sensors*. Bronkhorst High - Tech B.V., p. 8–10.

[25] Berson, A., Blanc-Benon, P., Comte-Bellot, G., (2010). On the use of hot-wire anemometry in pulsating flows. A comment on 'A critical review on advanced velocity measurement techniques in pulsating flows'. *Measurement Science and Technology*, vol. 21, no. 12, p. 1-6, **DOI:10.1088/0957-0233/21/12/128001**.

[26] Bronkhorst (2016). *Instruction manual: FlowPlot Software tool for monitoring FLOW-BUS parameter values and optimizing controller settings of digital instruments*. Ruurlo, p. 14.

[27] Grabe, C., Bebber, D., Murrenhoff, H. (2012). Development of a method to evaluate CNG-injection valves. *ASME/BATH 2015 Symposium on Fluid Power and Motion Control*, Chicago.

[28] FESTO (2012). *Solenoid valves MHJ - fast-switching valves technical data,* Festo.

Vsebina

Strojniški vestnik - Journal of Mechanical Engineering
letnik 62, (2016), številka 9
Ljubljana, september 2016
ISSN 0039-2480

Izhaja mesečno

Razširjeni povzetki (extended abstracts)

Strojniški vestnik - Journal of Mechanical Engineering 62(2016)9, SI 83

Prejeto v recenzijo: 2016-04-11
Prejeto popravljeno: 2016-05-30
Odobreno za objavo: 2016-06-01

Avksetični celični materiali - pregled

Nejc Novak* – Matej Vesenjak – Zoran Ren
Univerza v Mariboru, Fakulteta za strojništvo, Slovenija

Avksetični celični materiali so sodobni materiali, ki imajo številne edinstvene mehanske lastnosti v primerjavi s konvencionalnimi celičnimi materiali. Avksetični materiali so materiali z negativnim Poissonovim številom, kar pomeni, da se ob enoosni natezni obremenitvi prečni prerez materiala na to smer poveča, obratno pa velja ob tlačni obremenitvi. Učinek takšnega obnašanja materiala je uporaben pri različnih aplikacijah, kjer lahko z uporabo avksetičnih materialov izboljšamo mehanske lastnosti (npr. trdnost, lomno žilavost, absorpcijo energije in dušenje). Te lastnosti so lahko tudi prilagojene različnim vrstam obremenitev z uporabo različnih geometrij in razporeditev gostote, kar lahko dosežemo s funkcionalno gradiranimi avksetičnimi celičnimi materiali. V preglednem članku je predstavljeno področje avksetičnih celičnih materialov, njihov razvoj, najpogostejše geometrije, proizvodni postopki, mehanske lastnosti, aplikacije in nadaljnje možnosti za razvoj teh materialov.

Na podlagi pregleda literature je v članku podan strukturiran pregled zgodovine razvoja avksetičnih materialov, od začetkov transformiranja konvencionalnih odprto-celičnih pen, do sodobnih avksetičnih struktur z zapleteno geometrijo, ki so izdelane s pomočjo dodajalnih tehnologij. Predstavljenih je nekaj najznačilnejših dvodimenzionalnih avksetičnih struktur (satovij), na osnovi katerih je shematično prikazan postopek njihove deformacije in vzrok za doseženo negativno Poissonovo število. Na osnovi enačb mehanike kontinuuma so podane teoretične prednosti teh materialov in vpliv negativnega Poissonovega števila na mehanske lastnosti, ob tem pa so zbrani tudi podatki iz literature o vrednostih Poissonovega števila in modula elastičnosti že izdelanih avksetičnih materialov.

Avksetični celični materiali lahko s svojimi edinstvenimi mehanskimi lastnosti nudijo napredek v različnih aplikacijah. S sposobnostjo boljše absorpcije energije, ki je dosežena tudi s tem, da se material steka v smeri področja udarca in ne stran od tega področja, imajo ti materiali izjemen potencial za uporabo na področju balistične zaščite vozil, stavb in ljudi. Zaradi edinstvenega deformacijskega obnašanja lahko z uporabo avksetičnih celičnih materialov izboljšamo tudi različna področja v letalski in vesoljski industriji, medicini ter športnih aplikacijah.

Pregled literature pokaže, da se na področju avksetičnih materialov trenutno odvija intenziven razvoj novih geometrij, ki pa so bile zaenkrat le redko testirane pri visokih hitrostih deformacije, tako da je potrebno odziv avksetičnih celičnih materialov na visoke hitrosti deformacije še preučiti. Odziv materiala na različne hitrosti deformacije in načine obremenitve pa je možno z uporabo numeričnih simulacij in optimizacijskih metod tudi vnaprej predvideti in geometrijo avksetične celične strukture konstruirati tako, da bo med obremenjevanjem povzročila želen odziv na konstrukcijo (konstantna reakcijska sila) ali na udarno telo (konstanten pojemek). To je mogoče doseči z uporabo funkcionalno gradiranih avksetičnih celičnih materialov, kar je lahko zelo koristno pri balistični zaščiti in zaščiti pri trku.

Članek podaja izčrpen pregled področja avksetičnih celičnih materialov, s tem pa prispeva k boljšemu razumevanju lastnosti teh sodobnih materialov, ki kažejo velik potencial, da v prihodnosti postanejo pomembni lahki konstrukcijski materiali. Podane so smernice za nadaljnji razvoj avksetičnih celičnih materialov, predvsem v smeri funkcionalno gradiranih struktur, ki nudijo dodatno izboljšanje mehanskih lastnosti avksetičnih celičnih materialov.

Ključne besede: celični materiali, avksetični materiali, negativno Poissonovo število, satovje, kompoziti

*Naslov avtorja za dopisovanje: Univerza v Mariboru, Fakulteta za strojništvo, Smetanova ulica 17, 2000 Maribor, Slovenija, nejc.novak5@um.si

Strojniški vestnik - Journal of Mechanical Engineering 62(2016)9, SI 84

Prejeto v recenzijo: 2015-09-13
Prejeto popravljeno: 2016-04-08
Odobreno za objavo: 2016-05-09

Analiza mikrogibanj mikroprijemala po metodi grafa povezav

Chao Lin[1,*] – Yi-hang Ren[1] – Jiu-xiang Ji[1] – Li-zhong Cai[1] – Ji-ming Shao[2]
[a] Univerza v Chongqingu, Državni laboratorij za mehanske prenose, Kitajska
[b] Državni laboratorij v Šanghaju za mehanizme vesoljskih plovil, Kitajska

Mikro- in nanotehnologije so v zadnjih letih s hitrim razvojem znanosti in tehnologije postale ena od glavnih raziskovalnih smeri po vsem svetu. V mnogih industrijah se povečuje povpraševanje po mikromehanizmih, še posebej za manipulacijo z biološkimi celicami, mikrokirurgijo in montažo mikrostrojev. Zaradi miniaturizacije so se pojavile nujne potrebe po razvoju fleksibilnih, visokonatančnih in preprosto vodljivih mikrorobotov, vse več pozornosti pa pridobivajo tudi mikromanipulatorji v kombinaciji s tehnologijo mikropozicioniranja in robotsko tehnologijo. Mikroprijemala postajajo vse pomembnejši del sistemov za mikromanipulacijo. Prenos gibanj pri fleksibilnih mikroprijemalih je odvisen od deformacij materiala, zato je težko jamčiti za točnost modeliranja kinematike. Prav tako je težko zajeti specifične spremembe stanj pri internih komponentah mikroprijemal. Nelinearnost sistemov je mogoče intuitivno popisati z metodo grafa povezav, pri čemer so vse spremenljivke stanj v modelu fizikalne spremenljivke in omogočajo popis sprememb stanj sistema. Pomembno je tudi ujemanje med grafom povezav in enačbami sistemskih stanj. Na podlagi grafa povezav sistema je mogoče postaviti ustrezen matematični model in takšen pristop je bil do zdaj uporabljen pri analizi mehanizma Stewartove platforme. Za analizo fleksibilnih mehanizmov pa bi bilo treba metodo grafa povezav še dodatno izpopolniti.

Zaradi prednosti uporabe grafov povezav pri analizi fizičnih modelov kompleksnih sistemov je v tem članku postavljen model grafa povezav za mikroprijemalo, in sicer na podlagi analize principa delovanja, togosti ojačevalnega mehanizma BTAM in PDM. Izpeljane so karakteristične enačbe in enačbe prostora stanj. S simulacijo in analizo v okolju MATLAB sta bili pridobljeni simulacijski krivulji za odmik izhoda in za kotni odmik fleksibilnega tečaja. Mikroprijemalo je bilo izdelano s pomočjo laserske tehnologije za hitro izdelavo prototipov, za verifikacijo eksperimentov pa je bila narejena primerjava eksperimentalnih in teoretičnih rezultatov.

Članek predstavlja zasnovo tristopenjskega ojačevalnega mikroprijemala, za katerega je postavljen model psevdotogega telesa (PRB). Analizirana je togost BATM in izpeljana je vhodna togost mikroprijemala. Postavljen je model grafa povezav mikroprijemala, izpeljane pa so tudi karakteristične enačbe in enačbe stanj mikroprijemala. Krivulje vhodno/izhodnih odmikov mikroprijemala ter kotnega odmika fleksibilnega tečaja so bile pridobljene s simulacijo v Matlabu na podlagi enačb stanj. Opravljena je bila analiza mikroprijemala po metodi končnih elementov, kakor tudi eksperimenti za verifikacijo. Primerjava rezultatov simulacij v Matlabu, rezultatov analize po metodi končnih elementov in rezultatov eksperimentov je pokazala, da so prvi in drugi praktično enaki. Razlika med rezultati simulacij v Matlabu in rezultati analiz po MKE je majhna, kar potrjuje pravilnost in uporabnost tega modela grafa povezav. Metoda grafa povezav je torej primerna nova metoda za analizo sprememb stanj pri fleksibilnih mehanizmih in njihovih komponentah.

Za izboljšanje praktičnosti mikroprijemala je treba raziskati tudi vpenjalne sile. Uporabljeno metodo grafa povezav je treba še dodatno izpopolniti na drugih mehanizmih.

Ključne besede: mikroprijemalo, psevdotogo telo (PRB), fleksibilen tečaj, graf povezav, Matlab, 3D-tiskanje

*Naslov avtorja za dopisovanje: Univerza v Chongqingu, Državni laboratorij za mehanske prenose, Chongqing, Kitajska, linchao@cqu.edu.cn

Strojniški vestnik - Journal of Mechanical Engineering 62(2016)9, SI 85

Prejeto v recenzijo: 2016-01-28
Prejeto popravljeno: 2016-03-23
Odobreno za objavo: 2016-04-25

Optimizacija zavornega faktorja pri bobnastih zavorah z S-odmikalom po metodi odzivne površine

Irfan Sayim – Dan Zhang

Univerza v Ontariu, Inštitut za tehnologijo, Oddelek za strojništvo, avtomobilski in proizvodni inženiring, Kanada

Zavorni sistem spada med varnostne podsisteme vozila in kot tak opravlja pomembne delovne naloge. Predpisi zahtevajo nadzorovano, stabilno, predvidljivo in ponovljivo delovanje zavornega sistema na vsaki cesti, pri vsaki obremenitvi ali vremenskih razmerah, pa tudi v primeru delnega izpada. Zaradi vseh naštetih pričakovanj mora biti delovanje zavor stabilno. Deli zavornega podsistema, kot so ventili in izvršni členi, so dobro nadzorovani in ne prispevajo pomembneje k variabilnosti učinkovitosti delovanja zavornih sestavov na oseh. Ta je tako odvisna predvsem od nepredvidljivih fizičnih razmer, npr. od obremenitev, stanja vozišča in vremena. Te razmere se lahko v zavornem sistemu odražajo kot vročina ali vlaga, ki vplivata na trenje in s tem na celoten zavorni sistem. Elektronski podsistemi lahko delno zmanjšajo variabilnost učinkovitosti delovanja zavor tako, da preprečujejo blokiranje koles ali omogočijo porazdelitev vertikalnih sil z upravljanjem tlaka v zračnih vodih. Ti sistemi pa vseeno ne morejo jamčiti za to, da bo delovanje zavor popolnoma stabilno. Predstavljena študija raziskuje variabilnost učinkovitosti delovanja zavor pri gospodarskih vozilih z ozirom na zavorni faktor (BF). Zavorni faktor je povezan z zavorno silo vozila in celotna variabilnost učinkovitosti delovanja zavornih sestavov na oseh pri gospodarskih vozilih je tako odvisna od variabilnosti BF. Popis težav zaradi variabilnosti BF je ključnega pomena za kvantifikacijo variabilnosti učinkovitosti delovanja zavornega sistema vozila. Z drugimi besedami: učinkovitost delovanja zavornih sestavov na oseh ima prednost pri zagotavljanju učinkovitosti delovanja celotnega sistema.

V zadnjem desetletju je bil opazen trend zamenjave bobnastih zavor na oseh gospodarskih vozil s kolutnimi zavorami, do katerih pa mnogi proizvajalci ostajajo skeptični. Bobnaste zavore (v izvedbi z S-odmikalom, razpiralom itd.) so še vedno prva izbira pri proizvajalcih tovornjakov, avtobusov in prem. Med proizvajalci vozil velja konsenz, da imajo bobnasti zavorni sestavi na oseh z S-odmikalom še vedno velik potencial, če bo le mogoče izboljšati njihovo učinkovitost delovanja. Izkušnje so pokazale, da je mogoče vibracije na vozilih pripisati visoki stopnji variabilnosti BF pri sestavih bobnastih zavor, medtem ko so te težave pri kolutnih zavorah zaradi manjših vrednosti BF razmeroma neznatne. Bobnasta zavora z S-odmikalom predstavlja v tem kontekstu glavno konkurenco kolutnim zavoram glede vrednosti BF. Če bi pri bobnastih zavorah z S-odmikalom uspeli doseči primerljivo učinkovitost delovanja kot pri kolutnih zavorah, bi bila to zanje gotova konkurenčna prednost na trgu tudi v prihodnje.

Predstavljeno delo obravnava optimizacijo BF v fazi snovanja bobnaste zavore z S-odmikalom v sklopu dimenzijskih lastnosti, in sicer z namenom izboljšanja učinkovitosti delovanja zavor vozila. Najprej so opredeljene vrste obrabe zavornih oblog in vplivi položaja odmikalnega valja. S spreminjanjem dimenzijskih parametrov znotraj tehnično izvedljivega območja je bila teoretično kvantificirana variabilnost BF. Za identifikacijo kombinacij dimenzij z zmanjšano vrednostjo BF znotraj teoretičnih rezultatov je bila uporabljena metodologija odzivne površine (RSM). Nato sta bila preizkušena dva vzorca za validacijo relativnega izboljšanja. Preizkušen je bil en vzorec z imenskimi dimenzijami, kot se vgrajuje v vozila na trgu, zgrajen pa je bil tudi nov vzorec z dimenzijami, spremenjenimi na podlagi analize RSM. Izkazalo se je, da je z izbiro ustreznih dimenzij v fazi snovanja mogoče doseči pomembno izboljšanje BF.

Ključne besede: zavorni faktor, obraba oblog, bobnasta zavora na osi z S-odmikalom, kolutna zavora, metoda odzivne površine, položaj odmikalnega valja

*Naslov avtorja za dopisovanje: Univerza v Ontariu, Inštitut za tehnologijo, Oddelek za strojništvo, avtomobilski in proizvodni inženiring, L1H 7K4 Oshawa, ON, Kanada, irfan.sayim@uoit.ca

Strojniški vestnik - Journal of Mechanical Engineering 62(2016)9, SI 86

Prejeto v recenzijo: 2015-11-11
Prejeto popravljeno: 2016-03-30
Odobreno za objavo: 2016-05-16

Drseči tok nanofluidov med vzporednima ploščama, ogrevanima s konstantnim toplotnim tokom

Ayşegül Öztürk - Kamil Kahveci*
Univerza Trakya, Turčija

Predstavljena študija preučuje stacionarni, polno razviti laminarni tok in prenos toplote v nanofluidih med vzporednima ploščama, ogrevanima s konstantnim toplotnim tokom. V literaturi je dostopnih veliko študij toka plinov in kapljevin v mikrokanalih, po drugi strani pa obstaja le malo študij vpliva nanodelcev v osnovnem fluidu na drseči tok. Namen predstavljenega dela je zato analitična preiskava vpliva nanofluidov na drseči tok ter razkrivanje vpliva različnih parametrov na tok in prenos toplote.

Privzet je stacionaren, laminaren, nestisljiv in popolnoma razvit tok s konstantnimi termofizikalnimi lastnostmi. Nanofluid je obravnavan kot enofazen fluid, saj so trdni nanodelci zelo majhni in se zlahka fluidizirajo. Momentne in energijske enačbe so bile analitično razrešene pri robnih pogojih neničelne hitrosti na površini in temperaturnega skoka. Osnovni fluid je voda, dodani pa so ji bili nanodelci Cu, CuO in Al_2O_3. Viskoznost nanofluida je bila ocenjena po Brinkmanovem modelu za dvofazno zmes. Dejanska toplotna prevodnost nanofluidov je bila ocenjena po modelu Yu-Choi. Nanofluid je po tem modelu sestavljen iz glavne mase kapljevine, trdnih nanodelcev in trdnim podobnih nanoplasti, ki delujejo kot toplotni most med trdnimi nanodelci in maso kapljevine. Pridobljeni so bili rezultati za faktor drsenja v območju od 0 do 0,04, za Brinkmanovo število v območju od –0,1 do 0,1, za tri različne vrednosti razmerja med debelino tekočih plasti in polmera delcev (0,1, 0,2 in 0,4), ter za volumski delež trdnih delcev v območju od 0 % do 8 %.

Rezultati kažejo, da se s povečevanjem faktorja drsenja povečuje hitrost fluida ob stenah, hitrost v sredini kanala pa se zmanjšuje. Prav tako se povečuje temperaturni skok na stenah, kar pa negativno vpliva na prenos toplote. S povečevanjem faktorja drsenja se zmanjšujejo tudi viskozne sile v bližini stene, kar ima pozitiven vpliv na konvektivni prenos toplote iz stene na fluid ter negativen vpliv na konvektivni prenos toplote iz fluida na steno v razmerah nezanemarljive viskozne disipacije. Kombiniran vpliv hitrostnih in temperaturnih skokov se kaže v povečanju/zmanjšanju prenosa toplote pri pozitivnih/negativnih vrednostih Brinkmanovega števila. Vpliv faktorja drsenja na prenos toplote je manjši pri manjših vrednostih Brinkmanovega števila. Viskozna disipacija ob vroči steni zmanjša temperaturno razliko med trdno površino in fluidom in povprečno Nusseltovo število se tako s povečevanjem Brinkmanovega števila zmanjšuje. Viskozna disipacija ob hladni steni poveča temperaturno razliko med trdno površino in fluidom. Povprečno Nusseltovo število tako raste z večanjem Brinkmanovega števila v negativni smeri. Iz rezultatov sledi, da prisotnost nanodelcev v osnovnem fluidu pomembno vpliva tako na hitrostno polje kakor tudi na lastnosti prenosa toplote. Povprečno Nusseltovo število se z rastjo volumskega deleža trdnih nanodelcev občutno poveča, prav tako pa zavzame bistveno večje vrednosti pri večjih vrednostih razmerja med debelino tekočega sloja in polmerom nanodelcev. Povprečni toplotni tok pri nanofluidih z različnimi nanodelci je tako razvrščen od največjega do najmanjšega: Cu, Al_2O_3 in CuO. Izkazalo se je tudi, da povprečni toplotni tok najprej strmo pade, nato pa se z rastjo Brinkmanovega števila postopoma približuje asimptotski vrednosti.

Ključne besede: drseči tok, nanofluid, vzporedna plošča, faktor drsenja, Nusseltovo število

*Naslov avtorja za dopisovanje: Univerza Trakya, Oddelek za strojništvo, 22180 Edirne, Turčija, kamilk@trakya.edu.tr

Strojniški vestnik - Journal of Mechanical Engineering 62(2016)9, SI 87

Prejeto v recenzijo: 2016-02-03
Prejeto popravljeno: 2016-05-06
Odobreno za objavo: 2016-05-09

Numerična preiskava vpliva volumskega deleža nanodelcev na pretok, prenos toplote in ustvarjanje entropije v ferofluidu Fe_3O_4 v neenakomernem magnetnem polju

Fazel Hosseinzadeh[1] – Faramarz Sarhaddi[1,*] – Davod Mohebbi-Kalhori[2]

[1] Univerza v Sistanu in Balučistanu, Oddelek za strojništvo, Iran
[2] Univerza v Sistanu in Balučistanu, Oddelek za kemijsko tehnologijo, Iran

Ferofluidi so koloidne suspenzije, sestavljene iz nemagnetne nosilne tekočine, kot je voda, organsko olje ali kerozin, ter enodomenskih feromagnetnih nanodelcev. Ferofluidi imajo potencial za uporabo v nalogah prenosa toplote. Za optimalno zasnovo in nadzor nad termomagnetnimi aplikacijami prenosa toplote je treba poiskati povezave med apliciranim magnetnim poljem, pretokom ferofluida in porazdelitvijo temperature. Članek predstavlja raziskavo konvektivnega prenosa toplote s prisilnim tokom ferofluida (voda in Fe_3O_4) v vodoravnem dvodimenzionalnem kanalu pod vplivom neenakomernega dvorazsežnostnega magnetnega polja, ustvarjenega z linijskim dipolom.

Glavni cilj je preučitev vpliva volumskega deleža magnetnih nanodelcev Fe_3O_4 premera 10 nm na hidrotermalne lastnosti in ustvarjanje entropije v ferofluidu. Ogrevani ferofluid vstopa v kanal pri temperaturi 344 K. Spodnja stena je izotermni toplotni ponor s temperaturo 300 K, zgornja stena pa je adiabatna. Laminarni tok ferofluida je stacionaren, nestisljiv in viskozen. Vpliv magnetnega polja na viskoznost in toplotno prevodnost ferofluida ni upoštevan, prav tako pa je zanemarjena majhna Lorentzova sila zaradi električne prevodnosti v primerjavi z magnetizacijo. Zaradi nelinearnosti sklopljenih vodilnih diferencialnih enačb je bila uporabljena numerična metoda reševanja. Pri diskretizaciji kontinuitetnih, momentnih in energijskih enačb je bila uporabljena tehnika kontrolnih volumnov.

Za konvektivne in difuzijske člene je bila uporabljena gorvodna metoda drugega reda, za sklapljanje tlaka in hitrosti pa je bil razvit preprost algoritem. Za neodvisnost rezultatov od mreže je bilo raziskanih več različnih porazdelitev mreže. Veljavnost in točnost numeričnih rezultatov dokazuje primerjava z objavljenimi rezultati numeričnih raziskav vodnih ferofluidov pod vplivom linijskega dipola. Vsiljeni tok v odsotnosti zunanjega magnetnega polja in pri ničelnem volumskem deležu magnetnih nanodelcev doseže hidrodinamično popolnoma razvit profil pri dolžini x/h = 2,284 ter konstantno hitrost, ki ustreza 1,5-kratniku vstopne. Ob aktiviranju zunanjega magnetnega polja Kelvinova sila na telo premaga viskozno silo in tok fluida se močno spremeni. Ko se spremeni pretočno polje, se spremeni tudi temperaturno polje tako, da v termični mejni plasti blizu dipola nastane grba. Sprememba temperaturne porazdelitve zaradi magnetnega polja povzroči tudi spremembo temperaturnega gradienta v ferofluidu. Rezultati kažejo rast povprečnega Nusseltovega števila z dodajanjem delcev Fe_3O_4, tako da se vrednost v primerjavi z osnovnim fluidom pri 6 vol. % Fe_3O_4 poveča za 51,1 % pod vplivom magnetnega polja oz. za 8,5 % v odsotnosti magnetnega polja. Ugotovljeno je bilo, da imajo ferofluidi pri majhnih Reynoldsovih številih dobro sposobnost prenosa toplote, ker se ustvarja razmeroma malo entropije. Pri fiksni vrednosti črpalnega dela in majhnih vrednostih Reynoldsovega števila rahlo povečanje vrednosti Re za osnovno tekočino (približno do Re = 60) ugodno vpliva na prenos toplote. NUR za pospešeno osnovno tekočino je tako večji kot pri nepospešenem nanofluidu (volumski delež do 0,04), z vidika termodinamike pa se ustvarja več entropije (večji NSR v primerjavi z nepospešenim nanofluidom).

Nepospešeni nanofluid z volumskim deležem nad 0,04 ima pri večjih vrednostih Reynoldsovega števila za osnovno tekočino (Re > 60) boljše lastnosti prenosa toplote (večja vrednost NUR) v primerjavi s pospešeno osnovno tekočino, ustvarja pa se tudi manj entropije. Vrednost NSR z rastjo volumskega deleža Fe_3O_4 do 4 % v sistemu presega vrednost NUR, pri volumskih deležih med 0,04 in 0,06 pa se trend obrne. NUR pri 6 vol. % je tako v primerjavi s 4-odstotnim volumskim deležem magnetnih nanodelcev večji za 10,4 %, NSR pa le za 6,2 %. Iz tega zanimivega rezultata sledi, da je s stališča drugega zakona termodinamike primerno tudi povečanje volumskega deleža nanodelcev iz 0,04 na 0,06 ob povečanju konvektivnega prenosa toplote.

Ključne besede: ferofluid, volumski delež nanodelcev, magnetno polje, ustvarjanje entropije, končni volumni

*Naslov avtorja za dopisovanje: 1 Univerza v Sistanu in Balučistanu, Oddelek za strojništvo, Zahedan, Iran, fsarhaddi@eng.usb.ac.ir

Strojniški vestnik - Journal of Mechanical Engineering 62(2016)9, SI 88

Prejeto v recenzijo: 2015-09-28
Prejeto popravljeno: 2016-02-18
Odobreno za objavo: 2016-05-04

Karakterizacija dinamike mikrokonzol po metodi vzbujanja z udarnim valom

Dongsheng She[1,*] – Yiliu Yang[2] – Zefei Wei[1] – Zhen Yu[1]
[1] Univerza Bohai, Tehniški kolidž, Kitajska
[2] Univerza Bohai, Raziskovalni in učni institut pri kolidžu za računalništvo, Kitajska

Senzorji in aktuatorji MEMS za visoke temperature imajo velik potencial na različnih področjih, kot so avtomobilska, letalska in vesoljska, oborožitvena in jedrska industrija. Na učinkovitost delovanja naprav MEMS močno vplivajo dinamične karakteristike njihove notranje mikrostrukture, zato je nujna preučitev dinamičnih značilnosti mikrostrukture v visokotemperaturnem okolju. Pomemben parameter zasnove MEMS je temperaturni količnik lastne frekvence (TCF). Na podlagi TCF je mogoče napovedati variabilnost resonančnih frekvenc mikrostruktur v režimu spreminjajoče se temperature. Za eksperimentalno določitev vrednosti TCF za mikrostrukture je potreben sistem za dinamično preizkušanje z enoto za toplotno obremenjevanje.

Za preučitev TCF mikrokonzol iz enokristalnega silicija pri visokih temperaturah od 299 do 773 K je bil postavljen sistem za dinamično preizkušanje z enoto za toplotno obremenjevanje. Predlagana je metoda vzbujanja mikrokonzol z udarnim podstavkom po metodi udarnega vala, vibracijski odziv mikrokonzol pa se zajema s tehniko laserske Dopplerjeve vibrometrije. Sistem za dinamično preizkušanje je sestavljen iz treh glavnih delov: sistema za zajem in analizo podatkov, priprave za vzbujanje in enote za visokotemperaturno obremenjevanje. Izdelani sta bili dve mikrokonzoli iz enega kristala silicija, poimenovani mikrokonzola 1 in mikrokonzola 2. Mikrokonzola 1 je v obliki črke T, mikrokonzola 2 pa je enakomernega pravokotnega prereza.

Obe mikrokonzoli sta bili preizkušeni v visokotemperaturnem območju od sobne temperature do 773 K. Rezultati kažejo, da so se lastne frekvence pri povišanih temperaturah pri obeh mikrokonzolah nekoliko zmanjšale, odvisnost med lastno frekvenco prvega reda in temperaturo pa je praktično linearna. Obe mikrokonzoli imata skoraj enako vrednost TCF. Da bi ugotovili, zakaj imata mikrokonzoli različnih oblik enak TCF, smo analizirali teoretični TCF za obe mikrokonzoli. Iz teoretične analize sledi, da na vrednost TCF tako pri mikrokonzoli v obliki črke T kakor tudi pri mikrokonzoli z enakomernim pravokotnim prerezom vpliva le temperaturni količnik modula elastičnosti in temperaturnega koeficienta linearnega raztezka.

Predlagana metoda vzbujanja z udarnim valom je učinkovita pri mikrostrukturah z visokimi lastnimi frekvencami. Gre za brezkontaktno in neporušno metodo, ki uporablja tlačni impulz udarnega vala kot silo za vzbujanje mikrostrukture. Metoda vzbujanja z udarnim valom ima prednost pred vzbujanjem podstavka s piezoelektričnim keramičnim pretvornikom (PZT), ki je najbolj razširjen način za dinamično karakterizacijo mikrostruktur. Pri vzbujanju z udarnim valom prejme preizkušana mikrostruktura samo en udarec, pri vzbujanju prek podstavka s PZT pa je teh udarcev včasih tudi več zaradi kompleksnih elektromehanskih sklopitev. Metoda vzbujanja z udarnim valom je primerna tudi za visokotemperaturna okolja, je pa zahtevnejša v smislu potrebne opreme in upravljanja eksperimenta. Prav tako ne omogoča določanja vrednosti FRF za mikrostrukturo, saj je sila vzbujanja težko merljiva.

Ključne besede: preizkušanje dinamičnih karakteristik, mikrokonzola, udarni val, temperaturni količnik lastne frekvence, visoka temperatura, laserski Dopplerjev vibrometer

*Naslov avtorja za dopisovanje: Bohai univerza, Tehniški kolidž, No. 19, Keji cesta, Jinzhou, Kitajska, mems-sds@163.com

Strojniški vestnik - Journal of Mechanical Engineering 62(2016)9, SI 89

Prejeto v recenzijo: 2016-02-26
Prejeto popravljeno: 2016-05-27
Odobreno za objavo: 2016-06-07

Karakterizacija volumskega toka skozi PWM krmiljen hitri preklopni ventil

Miha Pipan* – Niko Herakovič
Univerza v Ljubljani, Fakulteta za strojništvo, Slovenija

Namen raziskave je podrobno analizirati vpliv različnih frekvenc in širine pulza PWM krmilne metode na karakteristiko volumskega toka hitrega preklopnega pnevmatičnega ventila. Prav tako je namen analizirati vpliv drugih pomembnih parametrov kot so tlačna razlika in najmanjša širina pulza potrebna za odprtje ventila. Pomemben cilj predstavljajo raziskave možnosti izdelave novih krmilnih algoritmov za hitre preklopne ventile s PWM metodo.

Pnevmatični servo sistemi, ki uporabljajo hitre preklopne ventile in so krmiljeni z digitalno tehniko, imajo prednost pred konvencionalnimi zvezno delujočimi pnevmatičnimi servo ventili glede ekonomičnosti, zanesljivosti in odziva. Uporabljene frekvence PWM signala za krmiljenje pnevmatičnih hitrih preklopnih ventilov so bile do sedaj med 20 Hz in 100 Hz in so pretežno omejene z odzivnim časom ventilov. Novejši preklopni ventili, ki delujejo na osnovi JetFlow tehnologije, uporabljajo krmilne membrane z majhno maso, in dosegajo odzivne čase pod 1 ms, s čimer omogočajo krmiljenje s PWM metodo frekvence do 500 Hz.

Pnevmatični hitri preklopni ventil smo krmilili z uporabo PWM krmilne metode pri frekvencah 200 Hz, 250 Hz in 300 Hz in merili volumski tok na izhodnem priključku pri tlačnih razlikah 0.1 bar do 6 bar. Analizirali smo vpliv tlačne razlike na minimalno širino pulza, pri kateri se je ventil odprl, ter odvisnost volumskega toka od širine pulza krmilnega signala. Za natančnejši popis odziva ventila, se je širina PWM-pulzov v prehodnem področju spreminjala od 0 % do 10 % s korakom 1 % in od 10 % do 100 % s korakom 10 %. Posebej smo z natančnostjo 0.1% širine pulza določili najkrajši pulz potreben za prvi odziv ventila.

Na podlagi rezultatov raziskav smo ugotovili, da s spreminjanjem širine pulza lahko zvezno krmilimo velikost odprtja ventila in s tem pretok skozi ventil. Minimalna širina pulza, potrebna za odpiranje ventila, se spreminja nelinearno glede na tlačno razliko in znaša med 0.1 ms in 0.4 ms. Povezava med širino PWM pulza in povprečnim tokom skozi ventil pri višjih tlačnih razlikah (nad 2 bar) postane linearna. Pri nižjih tlačnih razlikah (do 2 bar) in širini pulza, ko se ventil začenja odpirati, pojavi strmo povečanje volumskega toka, ki se nato stabilizira in postane linearen.

Z upoštevanjem rezultatov analiz je mogoče izdelati krmilni algoritem, ki bo uporabil PWM metodo s frekvenco 250 Hz, ki je za 150 % višja od sedanjih krmilnih algoritmov in se nahaja v nadkritičnem frekvenčnem območju pnevmatičnih komponent. Prav tako je prvič eksperimentalno izmerjena odvisnost spreminjanja minimalne širine pulza v odvisnosti od tlačne razlike.

Za linearno krmiljenje volumskega toka skozi ventil bomo odvisnost med želenim odprtjem ventila in širino PWM pulza upoštevali pri izdelavi krmilnega algoritma, ki bo glede na tlačno razliko določil minimalno širino pulza in upošteval strm začetni prehod. Razvit krmilni algoritem bo zaradi visoke frekvence in majhnih tlačnih udarov omogočil natančno zvezno krmiljenje aktuatorjev pnevmatičnih komponent. Odvisnost med širino pulza in želenim odprtjem ventila se bo določila z matematičnim popisom odvisnosti pretoka od širine pulza, oz. če to ni mogoče, z uporabo numeričnih metod. S tem bo omogočena izdelava hitro odzivnega digitalnega servo pnevmatičnega sistema za krmiljenje pnevmatičnih linearnih pogonov, tudi pnevmatičnih mišic, v zaprti zanki.

Ključne besede: hitri preklopni ventil, pulzno širinska modulacija, pretočne karakteristike, širina pulza

*Naslov avtorja za dopisovanje: Univerza v Ljubljani, Fakulteta za strojništvo, Aškerčeva 6, 1000 Ljubljana, Slovenija, miha.pipan@fs.uni-lj.si

DOKTORSKA DISERTACIJA

Na Fakulteti za strojništvo Univerze v Ljubljani so obranili svojo doktorsko disertacijo:

- dne *5. julija 2016* **Andrej ŠKRLEC** z naslovom: »Razvojna metoda za napoved obnašanja konstrukcij pri delovanju kratkotrajnih sunkovitih mehanskih obremenitev« (mentor: izr. prof. dr. Jernej Klemenc);

V delu je predstavljena metodologija za ocenjevanje parametrov materialnih modelov, ki opisujejo obnašanje materiala pri povišanih hitrostih specifičnih deformacij. Postopek ocene parametrov materialnih modelov, ki opisujejo vpliv hitrosti specifičnih deformacij, je osnovan na preizkusu vtiska kroglice v pločevinast preizkušanec. V ta namen smo izdelali napravo, s katero smo nadgradili že obstoječe preizkuševališče za razpočni test ohišij turbokompresorjev. Na osnovi eksperimentalnih rezultatov smo ocenjevali parametre Cowper-Symonds-ovega in Johnson-Cook-ovega materialnega modela, s katerima izvajamo kompleksna numerična vrednotenja izdelkov oz. posameznih komponent v primerih udarnih mehanskih obremenitev. Za oceno optimalnih vrednosti parametrov materialnih modelov smo med seboj povezali numerične simulacije, metode načrtovanja preizkusov, nov način modeliranja odzivnih površin in numerični optimizacijski algoritem. Dobljene parametre smo primerjali z vrednostmi iz literature in rezultate simulacij z optimalnimi parametri primerjali z eksperimentalnimi vrednostmi. Predstavljena metoda ocenjevanja parametrov s kombinacijo genetskega algoritma in razvitega globalno-lokalnega modela odzivne površine občutno skrajša čas za oceno parametrov materialnih modelov in je zato uporabna tudi na inženirskem nivoju;

- dne *5. julija 2016* **Gašper ŠKULJ** z naslovom: »Samoorganizacija avtonomnih delovnih sistemov v decentraliziranem proizvodnem sistemu« (mentor: prof. dr. Alojzij Sluga, somentor: doc. dr. Rok Vrabič);

Doktorska disertacija obravnava organizacijo proizvodnih sistemov v nepredvidljivem okolju sodobnega globaliziranega sveta z namenom razvoja konceptualnega modela personalizirane proizvodnje. Razvit konceptualni model dCM temelji na samoorganizaciji avtonomnih delovnih sistemov. Model je eksperimentalno preizkušen z uporabo metod eksperimentalne ekonomije. Lastnosti eksperimentalnega proizvodnega sistema so opazovane z vidika robustnosti in organiziranosti. Organiziranost sistema je analizirana z uporabo mere samoorganizacije decentraliziranega proizvodnega sistema, ki je razvita na podlagi teorije informacij. Potrjeno je, da se v eksperimentalnem proizvodnem sistemu izvede proces samoorganizacije;

- dne *6. julija 2016* **Jošt POTRPIN** z naslovom: »Mehansko optimiranje položajev gomoljev v lehi krompirja« (mentor: prof. dr. Rajko Bernik; interdisciplinarni študij Bioznanosti);

V letih 2011, 2012 in 2013 smo na poskusnem polju Biotehniške fakultete v Ljubljani izvajali poljski poskus s štirimi različnimi sortami krompirja (faluka, manitou, madeleine in stirling). Namen poskusa je bil ugotoviti, če obstajajo statistično značilne razlike v rastnih zahtevah različnih sort po prostoru v lehi krompirja. V ta namen smo opredelili in preučili naslednje parametre: površino oblike okrog gomoljev (elipsa), površino prečnega preseka lehe krompirja, vertikalni in horizontalni razpon gomoljev v lehi krompirja, dolžino a in b polosi elipse, najmanjšo oddaljenost gomoljev od zunanje stranice lehe krompirja in najmanjšo oddaljenost elipse od zunanje stranice lehe krompirja. Ker smo v letu 2012 ugotovili, da obstoječa metoda ME določanja površine oblike okrog gomoljev (elipsa) ni dovolj natančna, saj zavzema preveč praznega prostora v lehi in posledično ni dovolj statistično značilnih razlik, smo v letu 2013 nadgradili matematični model (metoda MCP), ki v izračun površine oblike okrog gomoljev (ogrinjača) vključi tudi fizikalno lastnost gomoljev - maso. Ugotovili smo, da imajo različne sorte različne rastne zahteve po prostoru v lehi krompirja. Za izbrane sorte smo določili optimalno obliko lehe na tak način, ki zagotavlja kar največji pridelek in kakovost krompirja;

- dne *11. julija 2016* **David KALJUN** z naslovom: »Optimizacija načrtovanja optičnega sistema LED svetilke« (mentor: prof. ddr. Janez Žerovnik, somentor: prof. dr. Jožef Duhovnik);

Delo obravnava področje simulacije prostorske porazdelitve svetlobe z vidika možnosti implementacij optimizacijskih metod. Sestavljeno je iz analitičnega in eksperimentalnega dela. Analitični del raziskave predstavlja implementacijo matematičnega modela in razvoj več iskalnih računalniških algoritmov potrebnih za delovanje optimizacijskih metod. Eksperimentalni del zajema računalniške simulacije za verifikacijo razvitih algoritmov in realno meritev za dokončno potrditev razvitih metod.Zaključek dela predstavljajo: razvita metoda za optimizacijo prostorske porazdelitve svetilnosti LED svetila,

potrditev ustreznosti matematičnega modela, predlog novega zapisa datoteke prostorske porazdelitve svetilnosti in optimizacijska aplikacija.

- dne *12. julija 2016* **Ivan DEMŠAR** z naslovom: »Kinematika in dinamika nadkolenske proteze za dvosledno smučanje« (mentor: prof. dr. Jožef Duhovnik, somentor: izr. prof. dr. Matej Supej);

Delo prestavlja rezultate teoretične in eksperimentalne analize in razvoja proteznega kolena za običajno dvosledno alpsko smučanje oseb z nadkolensko amputacijo. Delo temelji na analizi naravnega procesa kinematike in dinamike nog pri laboratorijski simulaciji gibanja smučarja v zavoju. Izdelana je simulacija kinematike, dinamike in trdnosti obstoječega proteznega kolena. Ustreznost matematičnega modela je preverjena z meritvami. Glede na vključenost smučarskega čevlja smo izdelali tudi meritve togosti smučarskega čevlja. Z meritvami kinematike in dinamike proteze in zdrave noge pri osebi z nadkolensko amputacijo in kontrolne skupine smo preverili ustreznost obstoječe proteze in oblikovali konstrukcijske smernice za nadaljnji razvoj proteze za dvosledno alpsko smučanje oseb z nadkolensko amputacijo;

- dne *12. julija 2016* **Vladimir PEJAKOVIĆ** z naslovom: »Vpliv ionskih tekočin na mejno mazanje jeklenih površin« (mentor: prof. dr. Mitjan Kalin);

V doktorski disertaciji smo raziskovali tribološke lastnosti različnih kombinacij kationov in anionov v sulfatnih ionskih tekočinah, ki smo jih uporabljali kot dodatke v baznih oljih za mejno mazanje v kontaktih jekla. Raziskovali smo vpliv baznih olj, koncentracije ionskih tekočin v baznem olju, dolžine alkilne verige in kontaktnih pogojev ter v povezavi s tem predlagali mehanizme mazanja. Uporabljena sulfatna skupina ionskih tekočin pred tem še ni bila raziskana v literaturi, kar predstavlja znanstveno novost naloge. Rezultati so pokazali jasen vpliv vrste kationov, kakor tudi dolžine alkilne verige anionov na tribološko obnašanje maziv. Za nekatere kontaktne razmere je bila ugotovljena tudi optimalna koncentracija ionskih tekočin. Zaščitni površinski mejni filmi, ki se tvorijo med tribološkimi kontakti temeljijo predvsem na osnovi sulfidov, ki omogočajo znižanje trenja.

*

Na Fakulteti za strojništvo Univerze v Mariboru so obranili svojo doktorsko disertacijo:

- dne *7. julija 2016* **Gregor VEDENIK** z naslovom: »Upravljanje sprememb za prestrukturiranje poslovnih procesov v proizvodnji duroplastov s pomočjo generičnega modela« (mentor: doc. dr. Marjan Leber);

Slovensko gospodarsko okolje je v zadnjih desetletjih doživelo ogromno tranzicijskih, lastniških, tržnih, političnih in tudi finančnih sprememb. Podjetja, ki teh sprememb niso pravočasno upoštevala pri oblikovanju in izvajanju strategij, so se hitro znašla v težavah oziroma sploh niso preživela. Obvladovanje sprememb je ključnega pomena za konkurenčno delovanje podjetij, organizacij. Podjetja lahko za podporo uporabljajo različne pristope, tehnike, orodja, modele, ki pa niso prilagojeni zahtevam, ki izhajajo iz strategije in okolja ter tipu podjetja, še posebej, če so ta mala in srednje velika. V disertaciji je predstavljena zasnova in na študiju primera prikazano delovanje generičnega modela za obvladovanja sprememb, ki na osnovi simulacij menedžmentu v malih in srednje velikih podjetjih nudi podporo pri zaznavanju problemov, definiranju rešitev in implementaciji nujnih sprememb v poslovnih procesih. Uporaba generičnega modela za upravljanje sprememb statično podjetje spreminja v dinamično, ki je sposobno hitrih prestrukturiranj, ko je to potrebno;

- dne *14. julija 2016* **Tina ŽELJKO** z naslovom: »Uspešnost naprednega oksidacijskega postopka pri čiščenju tekstilne odpadne vode ter njena ponovna uporaba v procesu barvanja z reaktivnimi barvili« (mentor: prof. dr. Alenka Majcen Le Marechal);

Doktorska disertacija je razdeljena na dva večja sklopa. Prvi je namenjen kemometrijski karakterizaciji tekstilnih odpadnih vod, drugi pa UV/H_2O_2 postopku. V prvem sklopu smo s pomočjo podrobne kemijske analize posameznih tekstilnih procesnih odpadnih tokov iz tovarne Svilanit ter uporabljenih kemometrijskih metod (korelacijska analiza, CA, PCA in LDA) odpadne tokove klasificirali in ločili na tiste, ki bi se jih dalo obdelati z izbranimi tehnologijami čiščenja (UV/H_2O_2, UF, NF, MBR ter evapokoncentracija) v tekstilni tovarni sami. V drugem sklopu, ki je namenjen UV/H_2O_2 postopku, smo izvedli številne eksperimente na različnih napravah. Na laboratorijski UV/H_2O_2 napravi smo obdelali realne tekstilne odpadne vode iz tovarne Svilanit in Tekstina ter vodne raztopine hidroliziranega reaktivnega barvila RB 4. Na pilotni UV/H_2O_2 napravi smo obdelali različne realne tekstilne odpadne vode iz postopka barvanja z reaktivnimi barvili, nekaj primerov smo izvedli tudi na tekstilni odpadni vodi, ki je bila predhodno obdelana z UF v tovarni Svilanit. V tovarni Tekstina smo s pilotno UV/H_2O_2 napravo obdelali realne tekstilne odpadne vode, ki so bile predhodno čiščene z drugimi tehnologijami (NF, MBR ter evapokoncentracija). Najboljše rezultate smo dobili v primeru čiščenja nizko koncentriranih tekstilnih odpadnih vod (absorbanca < 1). Z in situ elektrokemijsko proizvedenim H_2O_2 na plinsko-difuzijski elektrodi smo pri modificiranem UV/

H_2O_2 postopku prav tako dosegli dobre rezultate razbarvanja in razgradnje realne tekstilne odpadne vode ter raztopin hidroliziranih reaktivnih barvil. Preostali H_2O_2 smo po laboratorijski UV/H_2O_2 obdelavi uspešno odstranili z encimatsko razgradnjo (katalaza). Določene tekstilne odpadne vode iz obeh tovarn smo po UV/H_2O_2 obdelavi ponovno uporabili v procesu barvanja ter s pomočjo barvne metrike določili kvaliteto obarvanega tekstilnega materiala. Iz rezultatov je razvidno, da so le nekatere tekstilne odpadne vode (absorbanca < 1) po UV/H_2O_2 postopku primerne za ponovno uporabo, primernost ostalih pa lahko izboljšamo še s predhodnim čiščenjem z drugimi tehnologijami;

● dne *16. julija 2016* **Martin KODRIČ** z naslovom: »Razvoj hibridnega stroja za delo na strmem terenu« (mentor: prof. dr. Jože FLAŠKER);

Obravnavamo problem vzdolžne obdelave nasadov na strmih kmetijskih površinah, ki se danes obdelujejo z vitelnimi obdelovalnimi stroji. Za ugotavljanje energijske učinkovitosti obdelave kmetijskih površin smo uvedli pojem izkoristek procesa obdelave kmetijskih površin, s katerim je opredeljeno razmerje med energijo delovnih priključkov in skupno vloženo energijo. Razvili smo koncept stroja, ki izkorišča razpoložljivo potencialno energijo in v času vožnje po strmi površini navzdol uporablja dva delovna priključka hkrati. Izdelali smo samovozni stroj z vitelnim in kolesnim pogonskim sklopom ter s hidrostatičnim prenosom moči. Prednosti novega stroja smo dokazali z metodo nevronskih mrež. Napisali smo algoritem za ugotavljanje in napovedovanje izkoristka procesa obdelave strme kmetijske površine. Rezultati izboljšav so manjša poraba goriva, manjša količina proizvedenega CO_2 in manjši stroški obdelave.

ZNANSTVENO MAGISTRSKO DELO

Na Fakulteti za strojništvo Univerze v Ljubljani je z uspehom zagovarjal svoje magistrsko delo:

● *dne 31. avgusta 2016* **Andrej GLOJEK** z naslovom: »Celovit in računalniško podprt proces zasnove in izdelave orodij za brizganje majhnih izdelkov iz polimernih materialov« (mentor: prof. dr. Karl Kuzman)

*

Na Fakulteti za strojništvo Univerze v Mariboru so z uspehom zagovarjali svoje magistrsko delo:

● *dne 11. julija 2016* **Alenka BOTOLIN** z naslovom: »Ekološki in ekonomski vidiki odvajanja in čiščenja izcednih vod deponije« (mentor: prof. dr. Darinka Fakin);

● *dne 13. julija 2016* **Iva MLINŠEK LEŠNIK** z naslovom: »Dejavniki tveganja v procesu realizacije invencije« (mentor: doc. dr. Marjan Leber);

● *dne 13. julija 2016* **Jože PAVLINJEK** z naslovom: »Uporaba vrednostno-časovnega profila pri optimizaciji stroškov investicijskega projekta« (mentor: prof. dr. Borut Buchmeister);

● *dne 14. julija 2016* **Damir LUKEŽIĆ** z naslovom: »Uporaba analize toka vrednosti pri optimizaciji poslovno-proizvodnih procesov« (mentor: prof. dr. Borut Buchmeister);

● *dne 14. julija 2016* **Aleš ELBL** z naslovom: »Optimizacija procesov razvoja z uvedbo koncepta sočasnega inženirstva« (mentor: prof. dr. Borut Buchmeister);

● *dne 15. julija 2016* **Barbara KOLAR** z naslovom: »Izdelava metodologije za ocenjevanje in sporočanje o okoljski uspešnost izdelka – »izračun okoljskega odtisa« za barvne koncentrate CCMaster - masterbatch« (mentor: doc. dr. Marjan Leber);

● *dne 16. avgusta 2016* **Peter KERŠ** z naslovom: »Optimiranje verige dodane vrednosti pri načrtovanju in izdelavi preoblikovalnih orodij« (mentor: prof. dr. Borut Buchmeister);

● *dne 17. avgusta 2016* **Marko SMRTNIK** z naslovom: »Analiza stroškovno-časovnega vložka v proizvodnji Kopur, d.o.o.« (mentor: prof. dr. Borut Buchmeister);

● *dne 17. avgusta 2016* **Stanka VUČKO PAVLEKOVIĆ** z naslovom: »Optimizacija krmiljenja proizvodnje po naročilu« (mentor: prof. dr. Borut Buchmeister);

● *dne 18. avgusta 2016* **Martin SMODIŠ** z naslovom: »Raziskava vsebnosti elementov redkih zemelj v prenosnih telefonih« (mentor: prof. dr. Niko Samec);

● *dne 18. avgusta 2016* **Janez CIGUT** z naslovom: »Upravljanje projektov v podjetju za proizvodnjo medicinske opreme« (mentor: izr. prof. dr. Iztok Palčič);

● *dne 18. avgusta 2016* **Irena KRAMBERGER** z naslovom: »Problematika adsorbljivih organskih halogenov in tenzidov v odpadnih vodah zdravstvene dejavnosti« (mentor: prof. dr. Milenko Roš);

● *dne 18. avgusta 2016* **Sabina HRAŠAN** z naslovom: »Vpliv hrupa na proizvodni in izobraževalni proces« (mentor: doc. dr. Nataša Vujica Herzog);

● *dne 18. avgusta 2016* **Katja TEMENT** z naslovom: »Zaznavanje amoniaka na osnovi sol-gel senzorskih nanosov« (mentor: prof. dr. Aleksandra Lobnik);

● *dne 18. avgusta 2016* **Vesna MASTEN GUBELJAK** z naslovom: »Odstranjevanje svinčevih in kromovih ionov iz vodnih raztopin s pomočjo

adsorpcije na nanodelce« (mentor: prof. dr. Aleksandra Lobnik);

● *dne 22. avgusta 2016* **Boštjan ŽIGON** z naslovom: »Modeliranje trka osebnih vozil« (mentor: prof. dr. Zoran Ren);

● *dne 23. avgusta 2016* **Zoran BELIĆ** z naslovom: »Validacija računskega modela za vrednotenje hrupa v okolju z meritvami v realnih pogojih« (mentor: prof. dr. Bojan Ačko);

● *dne 23. avgusta 2016* **Dražen MARKOVIĆ** z naslovom: »Izboljšava procesa nadzora kakovosti dobavljenih izdelkov« (mentor: prof. dr. Bojan Ačko);

● *dne 24. avgusta 2016* **Boštjan MARZIDOVŠEK** z naslovom: »Uvedba metode SMED kot korak na poti k vitki proizvodnji« (mentor: prof. dr. Borut Buchmeister);

● *dne 25. avgusta 2016* **Bojan ČURIN** z naslovom: »Razvoj in optimiranje električne oscilatorsko tangentne glave« (mentor: doc. dr. Marjan Leber);

● *dne 29. avgusta 2016* **Bojan KROPF** z naslovom: »Zasnova inteligentnega modela računalniško integrirane proizvodnje v topli valjarni aluminija« (mentor: prof. dr. Jože Balič);

● *dne 29. avgusta 2016* **Tilen RAVLAN** z naslovom: »Optimizacija kapacitet za proizvodnjo industrijskih nožev s simulacijsko analizo« (mentor: prof. dr. Borut Buchmeister);

● *dne 30. avgusta 2016* **Silvo BORŠIČ** z naslovom: »Model optimalizacije sprožanja v sanitarnih sistemih« (mentor: doc. dr. Mirko Ficko);

● *dne 30. avgusta 2016* **Miran ROŽMAN** z naslovom: »Metoda za določitev degradacije vročevodnih cevi na osnovi meritev neravnin profila« (mentor: prof. dr. Nenad Gubeljak);

● *dne 30. avgusta 2016* **Beno JURJOVEC** z naslovom: »Analiza vpliva postopka izdelave jekla 30MnVS6 na pojav površinskih napak z uporabo genetskega programiranja« (mentor: prof. dr. Jože Balič);

● *dne 30. avgusta 2016* **Petra FURMAN** z naslovom: »Problematika odpadnih vod v proizvodnji sukancev in trakov« (mentor: prof. dr. Darinka Fakin);

● *dne 30. avgusta 2016* **Jože TURNŠEK** z naslovom: »Obravnava elastične povratne deformacije pri globokem vleku visokotrdnostnih jekel« (mentor: prof. dr. Zoran Ren);

● *dne 31. avgusta 2016* **Jano MULEJ** z naslovom: »Trdnostna analiza in razvoj livarskega blažilca kinetične energije taline« (mentor: prof. dr. Nenad Gubeljak).

Information for Authors

All manuscripts must be in English. Pages should be numbered sequentially. The manuscript should be composed in accordance with the Article Template given above. The maximum length of contributions is 10 pages. Longer contributions will only be accepted if authors provide juastification in a cover letter. For full instructions see the Information for Authors section on the journal's website: http://en.sv-jme.eu .

SUBMISSION:

Submission to SV-JME is made with the implicit understanding that neither the manuscript nor the essence of its content has been published previously either in whole or in part and that it is not being considered for publication elsewhere. All the listed authors should have agreed on the content and the corresponding (submitting) author is responsible for having ensured that this agreement has been reached. The acceptance of an article is based entirely on its scientific merit, as judged by peer review. Scientific articles comprising simulations only will not be accepted for publication; simulations must be accompanied by experimental results carried out to confirm or deny the accuracy of the simulation. Every manuscript submitted to the SV-JME undergoes a peer-review process.

The authors are kindly invited to submit the paper through our web site: http://ojs.sv-jme.eu. The Author is able to track the submission through the editorial process - as well as participate in the copyediting and proofreading of submissions accepted for publication - by logging in, and using the username and password provided.

SUBMISSION CONTENT:

The typical submission material consists of:

- A **manuscript** (A PDF file, with title, all authors with affiliations, abstract, keywords, highlights, inserted figures and tables and references),
- Supplementary files:
  - a **manuscript** in a WORD file format
  - a **cover letter** (please see instructions for composing the cover letter)
  - a ZIP file containing **figures** in high resolution in one of the graphical formats (please see instructions for preparing the figure files)
  - possible **appendicies** (optional), cover materials, video materials, etc.

Incomplete or improperly prepared submissions will be rejected with explanatory comments provided. In this case we will kindly ask the authors to carefully read the Information for Authors and to resubmit their manuscripts taking into consideration our comments.

COVER LETTER INSTRUCTIONS:

Please add a **cover letter** stating the following information about the submitted paper:

1. Paper **title**, list of **authors** and their **affiliations**.
2. **Type of paper**: original scientific paper (1.01), review scientific paper (1.02) or short scientific paper (1.03).
3. A **declaration** that neither the manuscript nor the essence of its content has been published in whole or in part previously and that it is not being considered for publication elsewhere.
4. State the **value of the paper** or its practical, theoretical and scientific implications. What is new in the paper with respect to the state-of-the-art in the published papers? Do not repeat the content of your abstract for this purpose.
5. We kindly ask you to suggest at least two **reviewers** for your paper and give us their names, their full affiliation and contact information, and their scientific research interest. The suggested reviewers should have at least two relevant references (with an impact factor) to the scientific field concerned; they should not be from the same country as the authors and should have no close connection with the authors.

FORMAT OF THE MANUSCRIPT:

The manuscript should be composed in accordance with the Article Template. The manuscript should be written in the following format:

- A **Title** that adequately describes the content of the manuscript.
- A list of **Authors** and their **affiliations**.
- An **Abstract** that should not exceed 250 words. The Abstract should state the principal objectives and the scope of the investigation, as well as the methodology employed. It should summarize the results and state the principal conclusions.
- 4 to 6 significant **key words** should follow the abstract to aid indexing.
- 4 to 6 **highlights;** a short collection of bullet points that convey the core findings and provide readers with a quick textual overview of the article. These four to six bullet points should describe the essence of the research (e.g. results or conclusions) and highlight what is distinctive about it.
- An **Introduction** that should provide a review of recent literature and sufficient background information to allow the results of the article to be understood and evaluated.
- A **Methods** section detailing the theoretical or experimental methods used.
- An **Experimental section** that should provide details of the experimental set-up and the methods used to obtain the results.
- A **Results** section that should clearly and concisely present the data, using figures and tables where appropriate.
- A **Discussion** section that should describe the relationships and generalizations shown by the results and discuss the significance of the results, making comparisons with previously published work. (It may be appropriate to combine the Results and Discussion sections into a single section to improve clarity.)
- A **Conclusions** section that should present one or more conclusions drawn from the results and subsequent discussion and should not duplicate the Abstract.
- **Acknowledgement** (optional) of collaboration or preparation assistance may be included. Please note the source of funding for the research.
- **Nomenclature** (optional). Papers with many symbols should have a nomenclature that defines all symbols with units, inserted above the references. If one is used, it must contain all the symbols used in the manuscript and the definitions should not be repeated in the text. In all cases, identify the symbols used if they are not widely recognized in the profession. Define acronyms in the text, not in the nomenclature.
- **References** must be cited consecutively in the text using square brackets [1] and collected together in a reference list at the end of the manuscript.
- **Appendix(-icies)** if any.

SPECIAL NOTES

Units: The SI system of units for nomenclature, symbols and abbreviations should be followed closely. Symbols for physical quantities in the text should be written in italics (e.g. *v*, *T*, *n*, etc.). Symbols for units that consist of letters should be in plain text (e.g. ms^{-1}, K, min, mm, etc.). Please also see: http://physics.nist.gov/cuu/pdf/sp811.pdf .

Abbreviations should be spelt out in full on first appearance followed by the abbreviation in parentheses, e.g. variable time geometry (VTG). The meaning of symbols and units belonging to symbols should be explained in each case or cited in a **nomenclature** section at the end of the manuscript before the References.

Figures (figures, graphs, illustrations digital images, photographs) must be cited in consecutive numerical order in the text and referred to in both the text and the captions as Fig. 1, Fig. 2, etc. Figures should be prepared without borders and on white grounding and should be sent separately in their original formats. If a figure is composed of several parts, please mark each part with a), b), c), etc. and provide an explanation for each part in Figure caption. The caption should be self-explanatory. Letters and numbers should be readable (Arial or Times New Roman, min 6 pt with equal sizes and fonts in all figures). Graphics (submitted as supplementary files) may be exported in resolution good enough for printing (min. 300 dpi) in any common format, e.g. TIFF, BMP or JPG, PDF and should be named Fig1.jpg, Fig2.tif, etc. However, graphs and line drawings should be prepared as vector images, e.g. CDR, AI. Multi-curve graphs should have individual curves marked with a symbol or otherwise provide distinguishing differences using, for example, different thicknesses or dashing.

Tables should carry separate titles and must be numbered in consecutive numerical order in the text and referred to in both the text and the captions as Table 1, Table 2, etc. In addition to the physical quantities, such as *t* (in italics), the units [s] (normal text) should be added in square brackets. Tables should not duplicate data found elsewhere in the manuscript. Tables should be prepared using a table editor and not inserted as a graphic.

REFERENCES:

A reference list must be included using the following information as a guide. Only cited text references are to be included. Each reference is to be referred to in the text by a number enclosed in a square bracket (i.e. [3] or [2] to [4] for more references; do not combine more than 3 references, explain each). No reference to the author is necessary.

References must be numbered and ordered according to where they are first mentioned in the paper, not alphabetically. All references must be complete and accurate. Please add DOI code when available. Examples follow.

Journal Papers:

Surname 1, Initials, Surname 2, Initials (year). Title. Journal, volume, number, pages, DOI code.

[1] Hackenschmidt, R., Alber-Laukant, B., Rieg, F. (2010). Simulating nonlinear materials under centrifugal forces by using intelligent cross-linked simulations. *Strojniški vestnik - Journal of Mechanical Engineering,* vol. 57, no. 7-8, p. 531-538, DOI:10.5545/sv-jme.2011.013.

Journal titles should not be abbreviated. Note that journal title is set in italics.

Books:

Surname 1, Initials, Surname 2, Initials (year). Title. Publisher, place of publication.

[2] Groover, M.P. (2007). *Fundamentals of Modern Manufacturing*. John Wiley & Sons, Hoboken.

Note that the title of the book is italicized.

Chapters in Books:

Surname 1, Initials, Surname 2, Initials (year). Chapter title. Editor(s) of book, book title. Publisher, place of publication, pages.

[3] Carbone, G., Ceccarelli, M. (2005). Legged robotic systems. Kordić, V., Lazinica, A., Merdan, M. (Eds.), Cutting Edge Robotics. Pro literatur Verlag, Mammendorf, p. 553-576.

Proceedings Papers:

Surname 1, Initials, Surname 2, Initials (year). Paper title. Proceedings title, pages.

[4] Štefanić, N., Martinčević-Mikić, S., Tošanović, N. (2009). Applied lean system in process industry. *MOTSP Conference Proceedings*, p. 422-427.

Standards:

Standard-Code (year). Title. Organisation. Place.

[5] ISO/DIS 16000-6.2:2002. *Indoor Air – Part 6: Determination of Volatile Organic Compounds in Indoor and Chamber Air by Active Sampling on TENAX TA Sorbent, Thermal Desorption and Gas Chromatography using MSD/FID.* International Organization for Standardization. Geneva.

WWW pages:

Surname, Initials or Company name. Title, from http://address, date of access.

[6] Rockwell Automation. Arena, from *http://www.arenasimulation.com,* accessed on 2009-09-07.

EXTENDED ABSTRACT:

When the paper is accepted for publishing, the authors will be requested to send an **extended abstract** (approx. one A4 page or 3500 to 4000 characters). The instruction for composing the extended abstract are published on-line: http://www.sv-jme.eu/information-for-authors/ .

COPYRIGHT:

Authors submitting a manuscript do so on the understanding that the work has not been published before, is not being considered for publication elsewhere and has been read and approved by all authors. The submission of the manuscript by the authors means that the authors automatically agree to transfer copyright to SV-JME when the manuscript is accepted for publication. All accepted manuscripts must be accompanied by a Copyright Transfer Agreement, which should be sent to the editor. The work should be original work by the authors and not be published elsewhere in any language without the written consent of the publisher. The proof will be sent to the author showing the final layout of the article. Proof correction must be minimal and executed quickly. Thus it is essential that manuscripts are accurate when submitted. Authors can track the status of their accepted articles on http://en.sv-jme.eu/.

PUBLICATION FEE:

Authors will be asked to pay a publication fee for each article prior to the article appearing in the journal. However, this fee only needs to be paid after the article has been accepted for publishing. The fee is 240.00 EUR (for articles with maximum of 6 pages), 300.00 EUR (for articles with maximum of 10 pages), plus 30.00 EUR for each additional page. The additional cost for a color page is 90.00 EUR. These fees do not include tax.

Strojniški vestnik -Journal of Mechanical Engineering
Aškerčeva 6, 1000 Ljubljana, Slovenia,
e-mail: info@sv-jme.eu

9 770039 248001
ISSN 0039-2480

http://www.sv-jme.eu

Contents

Papers